DESIGN, SYNTHESIS, AND CHARACTERIZATION OF HIERARCHICAL-STRUCTURED FUNCTIONAL NANOCOMPOSITES

A Dissertation

by

YUAN YUE

Submitted to the Office of Graduate and Professional Studies of
Texas A&M University
in partial fulfillment of the requirements for the degree of

DOCTOR OF PHILOSOPHY

Chair of Committee,	Hong Liang
Committee Members,	Homero Castaneda-Lopez
	Philip Hemmer
	Jun Zou
Head of Department,	Ibrahim Karaman

May 2018

Major Subject: Materials Science and Engineering

ABSTRACT

Hierarchical-structured functional nanocomposites are a significant family of advanced materials. Multilayered or porous structures in micro- and nano-scales with zero-dimensional, one-dimensional, two-dimensional, and three-dimensional morphologies are the most promising features of hierarchical nanocomposites. They possess numerous favorable advantages such as ultrahigh surface area, great volumetric porosity, reduced weight, and enhanced physical and chemical activities. Various applications such as energy storage, catalysis, sensing, surface modifications, among others can be promoted by using the novel design of hierarchical nanomaterials. The optimal design of the synthesis routes to manipulate the morphology and property of hierarchical nanocomposites is a critical research topic with challenges. To date, different experimental approaches with bottom-up and top-down methods have been utilized to synthesize the hierarchical nano- and micro-structures.

Here in this research, the design, fabrication, and assembly of novel hierarchical metal–metallic-oxide nanocomposites are systematically investigated. Experimental approaches of hydrothermal treatment, wet-chemical synthesis, electrochemical etching, and electrochemical deposition are applied to synthesize hierarchical nanomaterials. They include the aluminum porous structure, nickel micro-channeled substrate, V_2O_5 nanosheets, and TiO_2 nanospheres. Experimental characterizations on wetting ability, heat transfer efficiency, and electrochemical performance are conducted for those hierarchical nanomaterials. The fancy properties of superhydrophilicity, improved heat

dissipation, and electrochemical energy storage performance are characterized for aluminum porous structure, Ni/Porous-Ni/V_2O_5 nanocomposites, and Cu/Ni/TiO_2 nanomaterials, respectively. The related mechanisms are systematically investigated.

Furthermore, theoretical research referring to the correlation between maximum capacity performance and morphological characteristics of a specific type of hierarchical electrode materials is accomplished. A quantitative model to calculate the value of maximum capacity for a specific electrode under a specific charge-discharge condition is proposed and validated.

In conclusion, this doctoral research systematically and comprehensively investigated several novel types of hierarchical nanomaterial from synthesis to application. Various types of novel hierarchical nanocomposites are fabricated and evaluated for various practical applications in different fields in this study. Moreover, the quantitative correlation between the maximum capacity and the morphological features of a specific lithium-ion battery electrode is also theoretically studied and validated.

DEDICATION

To my dear parents, who are proud of my impressive achievements.

To my beloved family, with whom my life is vibrant and inspirational.

ACKNOWLEDGEMENTS

Conducting the systematic study and research to earn a Ph.D. degree has been a challenging and significant experience for me. In this part, I would like to thanks to the support and assistant from many individuals.

First and foremost, I want to thank my Ph.D. advisor, Dr. Hong Liang, with my extreme grate appreciation, for her support, guidance, and supervision in my doctoral research and most importantly, the advice in my daily life during the Ph.D. studying period. She made me to obtain a comprehensive thought to think independently and creatively.

I would also like to thank the support from my Ph.D. advisory committee members, Dr. Homero Castaneda-Lopez, Dr. Philip Hemmer, and Dr. Jun Zou for their beneficial and meaningful advice and comments of this research.

I also want to express my appreciation to the assistant and guide from Dr. Abraham Clearfield, Dr. Partha Mukherjee, and Dr. Subrata Kundu for their generous help and support on my studies on electrochemical characterizations and nanoparticles synthesis. Their help meant a lot for my productive experimental results.

I want to say thanks to Dr. Karen Wooley, Dr. Winson Kuo, Dr. Haejune Kim, and Dr. Karl Hartwig. They provided the valuable help for me on the training and usage of a series of experimental facilities and the proofing of my research articles.

I am also grateful to the support from the Microscopy Image Center (MIC), Materials Characterization Facility (MCF), and the X-ray Diffraction Laboratory from

Department of Chemistry. I would like to give a special thanks to Engineering Academic and Students Affairs, Department of Mechanical Engineering, and Aggi_E Challenge Program for the opportunities of teaching assistant and mentoring undergraduate researchers.

I want to thank all the members in Surface Science Group as well for their help, assistance, and suggestions in my research. Particularly, assistance provided by Dr. Hyunho Choi, Dr. Sunghan Kim, Dr. Wei Dai, Dr. Yunyun Chen, Mr. Kyungjun Lee, and Ms. Lian Ma in my graduate research are also deeply appreciated.

Furthermore, I also want to thank Ms. Jules Henry, the academic advisor in Department of Materials Science and Engineering. She gave me significant helps on my degree plan arrangement.

Thanks for all of my friends and the department faculty and staff as well for making my learning and living time at Texas A&M University a great experience.

Finally, I really want to thank my parents and family members for all of their love, supports, and endless patience since my childhood, my efforts and achievements are their highest rewards.

CONTRIBUTORS AND FUNDING SOURCES

I would like to gratefully thank the support and attributions from my advisor, Dr. Hong Liang, and my committee members: Dr. Homero Castaneda-Lopez, Dr. Philip Hemmer, and Dr. Jun Zou for their valuable advice and comments of this research. Research assistance from Dr. Partha Mukherjee, Dr. Subrata Kundu, Dr. Winson Kuo, Dr. Abraham Clearfield, and Dr. Karl Hartwig are appreciated.

I was partially sponsored by the Texas A&M Energy Institute fellowship. Research accomplished with Dr. Abraham Clearfield were partially supported by e Robert A. Welch Foundation (Grant No. A-0673). The Aggi_E Challenge Program in 2015–2016 organized by Dwight Look College of Engineering of Texas A&M University supported the project of fabrication of aluminum porous structure. Partial support by the Texas A&M strategic seed grant program and the Turbomachine Research Laboratory is also acknowledged.

NOMENCLATURE

0/1/2/3D	Zero/one/two/three-dimensional
CVD	Chemical vapor deposition
LB	Langmuir-Blodgett
EESD	Electrochemical energy storage device
LIB	Lithium-ion battery
EDLC	Electron double layer capacitor
PC	Pseudocapacitor
LTMO	Lithium transition metallic oxide
TMO	Transition metallic oxide
SEM	Scanning electron microscopy
XRD	X-ray diffraction
EDS	X-ray energy dispersive spectroscopy
BET	Brunauer–Emmet–Teller
PVDF	Polyvinylidene fluoride
NMP	N-methyl-2-pyrrolidone
EC	Ethylene carbonate
DEC	Diethyl carbonate
CV	Cyclic voltammetry
EIS	Electrochemical impedance spectroscopy
SEI	Solid electrolyte interface

TABLE OF CONTENTS

LIST OF FIGURES

LIST OF TABLES

CHAPTER I

INTRODUCTION*

This chapter is the fundamental and comprehensive description of the major strategies of the whole research. This doctoral research is concentrated on the development of the novel types of hierarchical-structured nanomaterials. The basic concept, representative features, and typical experimental approaches to fabricate the hierarchical nanomaterials are systematically described. Several emerging and meaningful applications of such hierarchical nanomaterials are also introduced.

1.1 Hierarchical-structured nanomaterials

The family of the hierarchical nanomaterials has been exhibiting excellent performance after the proposing of the concept of "hierarchical materials" several decades ago [1]. The core feature of the hierarchical nanomaterial is revealed from their morphologies [1-3]. In the micro- or nano- scale, the nanosized layer-stacked morphology and the lamellar spatial distribution of hierarchical materials can usually be observed through the electron microscopy. Such layer-by-layer morphology can be categorized as numerous different styles. Figure 1 illustrates the typical types of appearances or morphologies of hierarchical nanomaterials. Nanoparticles-based

*Part of this chapter reproduced with permission from "Micro- and Nano-Structured Vanadium Pentoxide (V_2O_5) for Electrodes of Lithium-Ion Batteries" by Yuan Yue, *et al.*, *Adv. Energy Mater.*, **2017**, *7*, 1602545 (Copyright © 2017 Wiley-VCH).

microstructures such as yolk–shell or multiple stacked layers (0-dimensional, 0D) [4], branched or porous nanorods (1-dimensional, 1D) [5], the porous or layered nanosheets (2-dimensional, 2D) [6], and the assembled morphologies such as micro-flowers [7], inverse opal [8], and shape-specific particles [9] (3-dimensional, 3D) are the major styles of the hierarchical nanomaterials. Figure 1 exhibits several representative hierarchical structures in nano- and micro-scale.

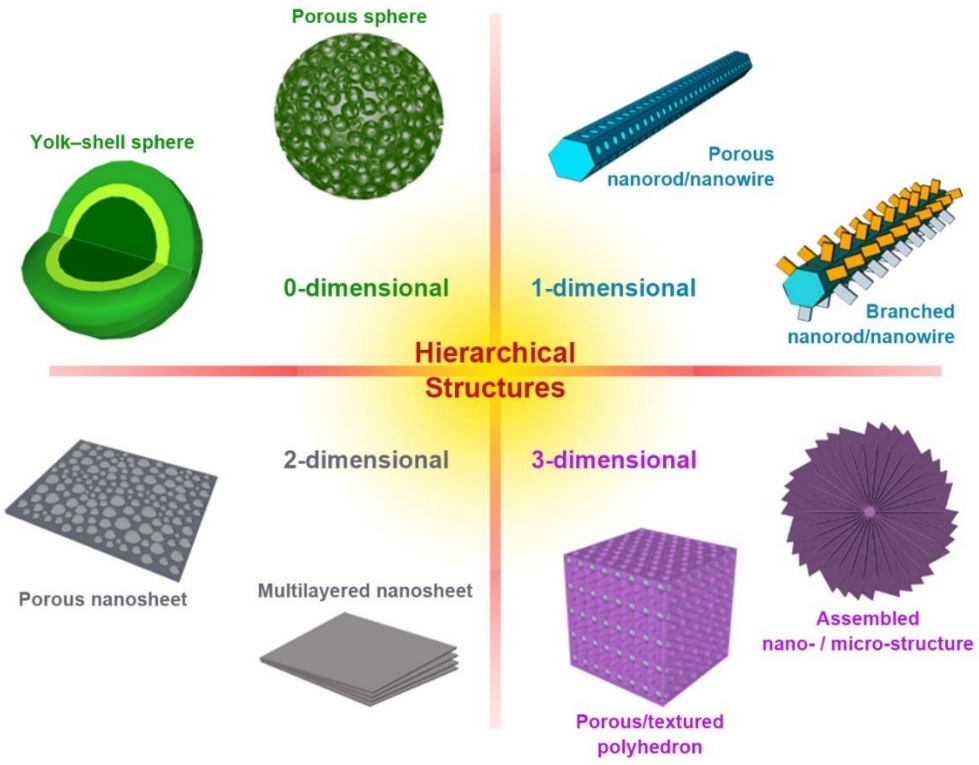

Figure 1. Schematic illustration of hierarchical nanomaterials with 0D, 1D, 2D, and 3D.

To date, the scalable and reliable fabrications and applications of novel hierarchical nanocomposites have become a series of crucial research topics. The main reason is their unique morphologies leading to interesting and tunable surface, physical,

and chemical properties. The unique characteristics such as high specific surface area, large volumetric porosity, light weight, and increased reaction activity led to versatile applications as shown in Figure 2, such as energy conversion or storage [3], catalysis [10], self-assembly [11], sensing [12], drug delivery [13], gas adsorption [14], among many others. In a word, the increasing demand of the micro- or nano-structured advanced materials promotes the development of the functional hierarchical nanocomposites. For this doctoral research, the novel fabrication and characterization of advanced hierarchical nanocomposites are proposed. As-fabricated samples of hierarchical nanocomposites are characterized for different applications, particularly for the electrochemical energy storage devices.

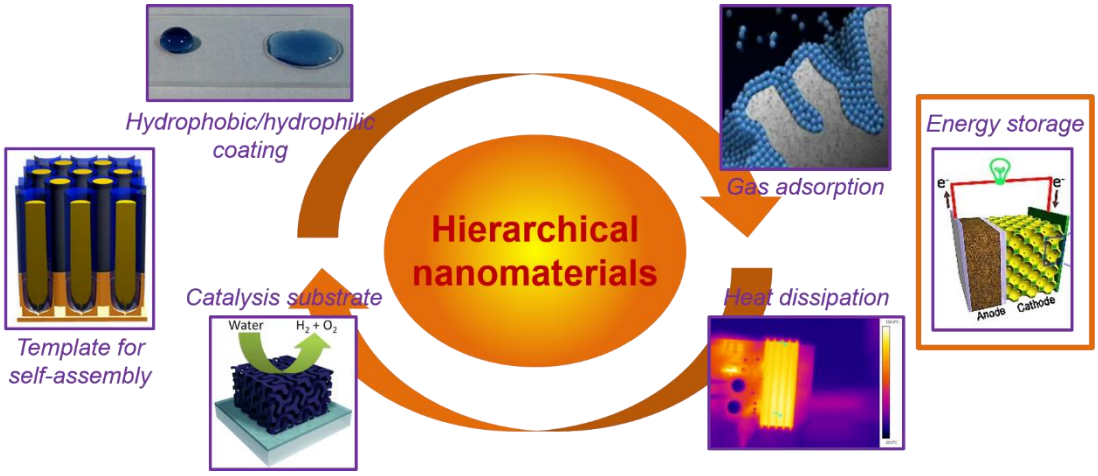

Figure 2. Representative applications of hierarchical nanomaterials.

1.2 Fabrications of hierarchical nanomaterials

There are numerously different experimental means, which have been created to fabricate the hierarchical nanomaterials. Methods of hydrothermal or solvothermal synthesis, chemical vapor deposition, wet-chemical synthesis, template-assisted coating

techniques, spin coating based assembly, electrochemical deposition, electrospinning or spray related methods, and self-assembly of nanoparticles are the most widespread eight approaches. A general summary of these eight methods is listed in Table 1. Meanwhile, a sketch to illustrate these typical methods is shown as Figure 3.

Table 1. The general summary of eight typical methods to manufacture the hierarchical nanomaterials.

Method	Fabricated materials	Major characteristics	Resulted structures	Reference
Hydrothermal or solvothermal	Ceramics, polymers, and their composites	Uniform size, well-defined crystallinity	Nanoparticle-based structures	[15, 16]
Chemical vapor deposition	Carbonaceous, ceramics materials	Well-defined crystallinity	Hierarchical thin-film structures	[17, 18]
Wet-chemical synthesis	Metals, ceramics, and polymers	Ease to fabricate, uniform size	Nanoparticle-based structures	[19, 20]
Self-assembly	Metals, ceramics, and polymers	Well-controlled morphology	Nanoparticle assembly	[21, 22]
Langmuir-Blodgett technique	Metals, ceramics, and polymers	Uniform coating	Layered films of nanoparticles	[23, 24]
Spin coating	Metals, ceramics, and polymers	Ease to fabricate, uniform distribution	Layer-by-layer thin films	[25, 26]
Electrochemical deposition	Metals, ceramics, and polymers	Uniform coating, well-defined crystallinity	Porous or hierarchical nanostructures	[27, 28]
Electrospinning	Polymers	Well-defined structure	Layered nanofiber structures	[29, 30]

There are two categories of the methods to fabricate the nanostructured hierarchical structures or materials. One is the bottom-up method, there other is top-down method. For the methods listed in Table 1, hydrothermal or solvothermal treatments, chemical vapor deposition (CVD), wet-chemical synthesis, electrochemical deposition, and electrospinning are typical bottom-up approaches. There are other types of methods such electrochemical etching, lithography or electron-beam lithography that

are considered as top-down approaches. Due to the restriction of the smallest fabricated dimensions of such top-down approaches, they are rarely used for the fabrication of the nanostructured hierarchical nanomaterials.

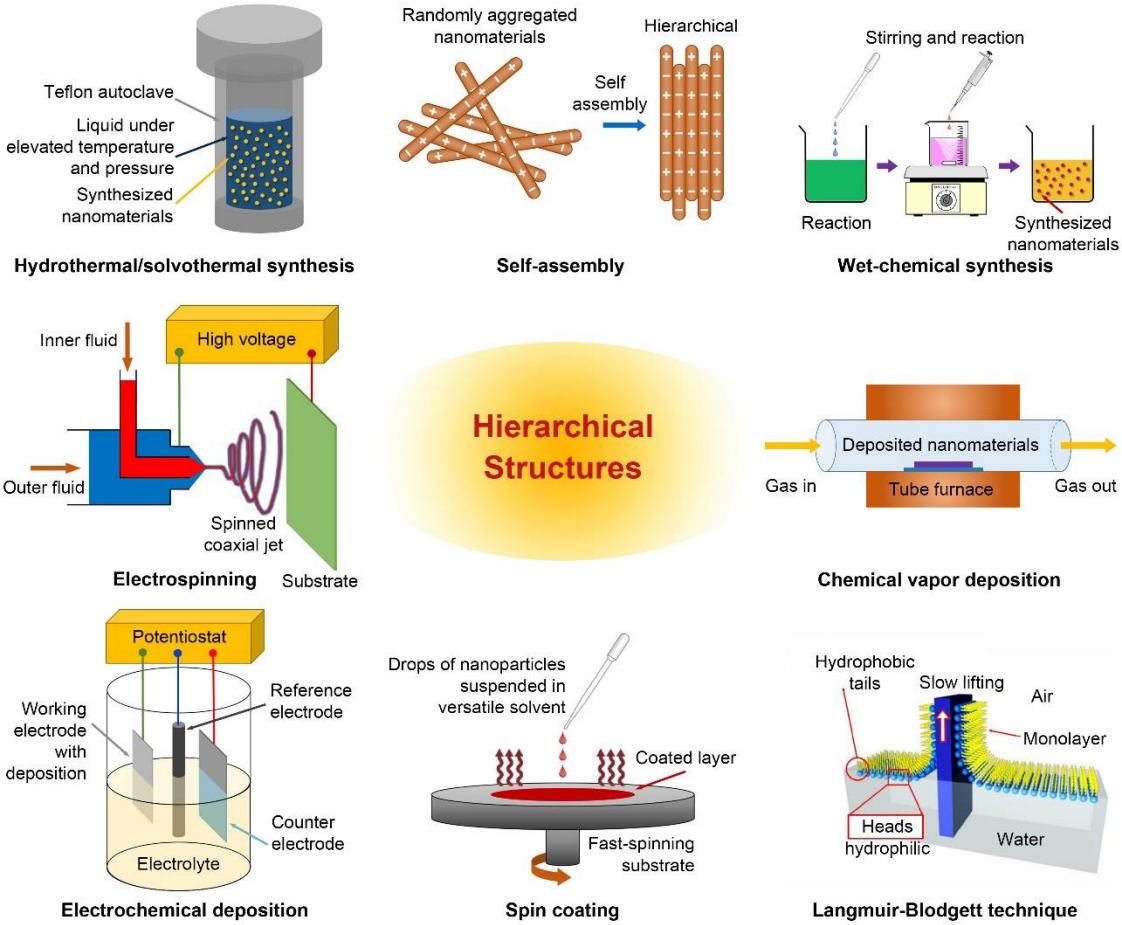

Figure 3. The sketch of typical fabrication methods of the hierarchical nanomaterials.

Hydrothermal or solvothermal routes are the most popular approaches to fabricate the hierarchical nanomaterials. During the hydrothermal or solvothermal process, the nanostructure can be grown with the well-controlled conditions inside the reaction vessel. Due to the high temperature and increased pressure introduced by the

supercritical solvent under the enclosed heating environment, the growth of the nanomaterials can have well-defined crystallinity as well as the uniform distribution [31]. Furthermore, the chemical kinetics of the synthetic reactions can facilitate the formation of the closely adjacent nanostructure [15]. This is the key point to form the hierarchical nanostructure. As another typical means to prepare the hierarchical nanomaterials, chemical vapor deposition can usually promote the formation of the well-crystalline and hierarchical thin film nanostructures due to the applying of the constant reactive gas flow under high temperature [32, 33]. As an experimental method which does not require rigid reaction conditions such as heating, pressuring, or specific gas flow, the wet-chemical synthesis possesses an obvious feature of the ease of the reaction condition. The instant or gradual formation and growth of the nanomaterials has the uniform morphology with the assistance of constant stirring of the reaction liquid [20]. During the stage of the formation of the nanostructure along with the stirring, the formed nanostructure will have the tendency to be bonded together because of the electrostatic force or van der Waals force. In this case, the hierarchical nanostructure may form by the wet-chemical synthesis. Furthermore, the self-assembly of the as-synthesized nanoparticles, nanowires, nanotubes, and nanosheets is another pathway to fabricate the hierarchical nanomaterials effectively. Fruitful experimental conditions are able to create the reliable environments for the purpose of the assembly of nanomaterials through the electrostatic or van der Waals force [34].

If the substrate or template can be introduced to the synthesis procedure, there will be more choices which are available to prepare the hierarchical nanomaterials. For

example, the hierarchical nanostructure can be fabricated after the continuous layer-by-layer deposition onto the substrate surface through the Langmuir-Blodgett (LB) technique [24]. Through the fine manipulation of the liquid viscosity, lift velocity after dipping, and the hydrophilic group addition, multiple layers of the nanomaterial thin film can be deposited. The process of the spin coating on a smooth or textured surface of the substrate is also a feasible means to fabricate the layer-by-layer hierarchical nanostructure. The optimal selection of the solvent and the rotation speed of the spinning are quite critical to the coating thickness and uniformity [25]. Moreover, through a series of spin coating of different suspensions, a kind of hierarchical architecture of different nanomaterials can be assembled layer-by-layer [19].

The application of the electric field or potential is also beneficial to prepare the hierarchical nanomaterials. Two distinct approaches are briefly introduced here. The first one is the electrochemical deposition. If a piece of the conductive substrate is placed vertically in electrolyte as the counter electrode, the seeds of nanomaterial can be nucleated at the surface of the substrate after applying a direct or alternating current between the substrate and the working electrode. With the continuous loading of the current, the growth of the nanostructure with specific hierarchical morphology will be possible [35]. Usually, the source of the deposited materials can come from the chemical component of either the solid working electrode or ions in the liquid electrolyte. The second approach is the electrospinning. The polymeric solution can undergo a process of the guided spinning onto the substrate after applying a high voltage between the

substrate and the spinning needle tip. The as-spun layers usually have the morphology of the hierarchical interconnected nanowires or nanofibers [30].

Substrates play important roles in building hierarchical structures. Approaches such as CVD, electrospinning, electrodeposition, spin coating, and LB technique are representative ones using substrate during the fabrication of hierarchical structures, as shown in Figure 3. One of the commonly used substrate-assisted methods is CVD. This method promotes the formation of the crystalline thin films by introducing reactive gas at elevated temperatures [32, 33]. A hierarchical structure can be generated by controllable epitaxial growth of nanocrystals on the surface of substrate. Another approach is using spin coating method by plating deposits on textured surfaces. The optimal selection of the solvent and the rotation speed are critical to the coating thickness and uniformity [25]. Through a series of spin coating of different suspensions, hierarchical structures of different nanomaterials can be assembled [19]. To fabricate quality hierarchical nanostructures, application of external fields such as electric was reported beneficial. Two approaches have been reported. One is the electrodeposition. In this approach, a conductive substrate is emerged into an electrolyte as the working electrode, the seeds of nanomaterial can be nucleated at the surface of the substrate after applying a current between the substrate and the counter electrode. With continued loading of the current, the growth of the nanostructure with specific hierarchical morphology was generated [35]. The source of the deposited materials comes from the chemical component of either the solid working electrode or ions in the liquid electrolyte. The other approach is electrospinning. Using this method, a polymeric

solution undergoes a process of the guided spinning onto the substrate after applying a high voltage between the substrate and the spinning needle tip. The resulting layers display the morphology of the hierarchical interconnected nanowires or nanofibers [30]. Finally, nanostructures can be fabricated through layer-by-layer deposition onto a substrate using the LB technique [24]. Through the optimization of the liquid viscosity and the hydrophilic group addition, multiple layers of the nanomaterial thin films can be deposited. As discussed above, the substrate-assisted methods can fabricate various types of hierarchical structures with controlled configuration in a larger length scale.

The remaining challenging issue is the lack of robust super-hierarchical nanostructures with more complexity that are manufactured at a large length scale with low-cost, high reliability, superior quality, and high yield. For methods with no substrate, the control of processing conditions is the first and critical issue with unsolved fundamental problems. The investigation of such problems related to the chemical thermodynamics or kinetics will promote the mass production of hierarchical materials. In addition, the as-fabricated individual hierarchical particles tend to agglomerate during drying process for actual usage. A process leading to direct usage of those particles without drying is necessary to prevent the negative effect from agglomeration. For substrate-assisted methods, the strength of the interface between the deposit and substrate is important. To solve this, the first step is to understand the principles between heterogeneous nucleation and epitaxial growth. Furthermore, the novel design of chemically-stable, hierarchical-structured, and light-weighted substrate can also open a new avenue to manufacture complex-structured hierarchical materials.

In a brief summary, the hierarchical nanomaterials can be fabricated through different choices of pathways according to different requirement of the ambient condition and the chemical used. This abundant available selections promote the development of the research related to the hierarchical nanomaterials.

1.3 Applications of hierarchical nanomaterials

1.3.1 Superhydrophilic or superhydrophobic coating layer

The terms of "hydrophilicity" and "hydrophobicity" are used to describe the wetting properties of a specific solid surface to the contact of liquid phase of water [36]. The most straightforward to common criterion to justify the wetting property of a surface is to measure the contact angle of a dropped water droplet on the surface. The contact angle θ is defined as the tangent angle at the solid–liquid–air triple point between the solid–liquid interface line and the tangent line of the droplet. Figure 4 indicates this method. According the measured value of contact angle, the wetting property of a specific surface can be identified as superhydrophilicity ($\theta < 5°$), hydrophilicity ($5° < \theta < 90°$), hydrophobicity ($90° < \theta < 150°$), and superhydrophobicity ($150° < \theta < 180°$) [36]. Currently, researcher have intensive interest to design and fabricate superhydrophilic or superhydrophobic surfaces for different types of applications.

The direct deposition of nanoparticles on a substrate through the evaporation suspension is a significant approach to assemble and coat the colloidal nanoparticles [37]. However, the negative issue of "coffee stain" effect due to the agglomeration of particles introduced by capillary force distribution blocks the practical usage of this

technique [38]. Figures 5a and b illustrate the formation of "coffee stain" composed of aggregated particles. The development of the novel substrate with textured surface morphology is necessary for the uniform coating of colloidal nanoparticles after drying suspension droplets. According to the related theory on the capillary force at the interface of droplet–substrate, a probable method to resolve the "coffee stain" effect is the addition of ordered vertically-aligned pores on the substrate [39]. The proposal vertically-aligned porous morphology and wettability of such substrate are sketched as Figures 5c and d. Therefore, facile, reliable, and cost-effective experimental means to fabricate numerous vertically-aligned porous structures on the metallic substrate is an important research topic. In this research, a simple and reliable method to fabricate the vertically-aligned pores using electrochemical etching on metallic sheets is proposed accordingly. Super-hydrophilic properties with extremely small contact angle is believed to achieve.

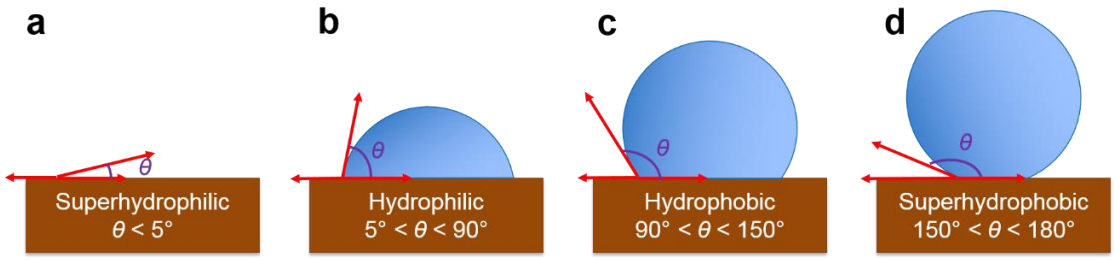

Figure 4. The illustration of various contact angles of a water droplet contacted with surfaces with different wetting properties.

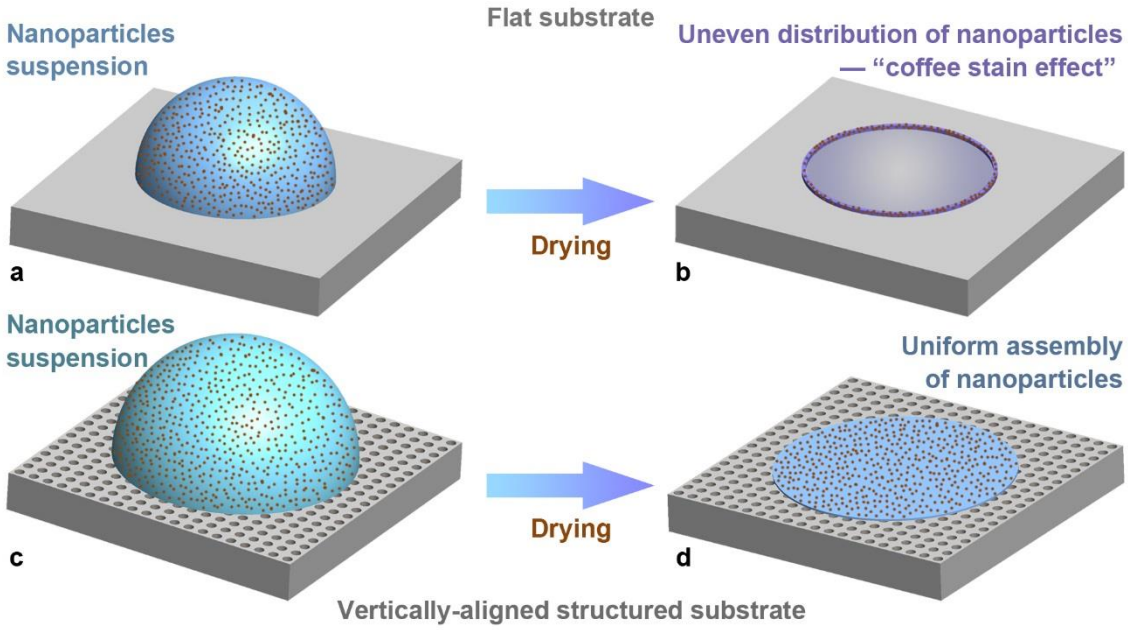

Figure 5. The comparison of the nanoparticle's deposition effect on between flat and vertically-aligned structured substrate.

1.3.2 Enhanced heat dissipation property

The ultrahigh surface area owned by hierarchical nanocomposites can be used in versatile applications. The enhanced heat dissipation property is the one with broad impacts. From the Fourier's law of thermal conduction, the total heat flow transported through a solid sample is proportional to its total surface area [40]. This is the main reason why a sample with greater surface area can dissipate more heat energy. In order to illustrate the enhanced heat dissipation of hierarchical materials, Figure 6 is sketched to compare the heat dissipation effect between flat and hierarchical coatings. Numerous hierarchical surface morphology in Figure 6b results in the increased surface area and causes the favorable heat transport efficiency. Unlike the conventional heat sink with macroscopic layered structures, hierarchical micro- or nano-composites can achieve the

same improvement of surface area while maintaining small occupied space. This is preferred for the practical usage of heat dissipation for microsized devices. In this research, the heat dissipation property of several types of hierarchical nanocomposites will be characterized to validate the advantage of them.

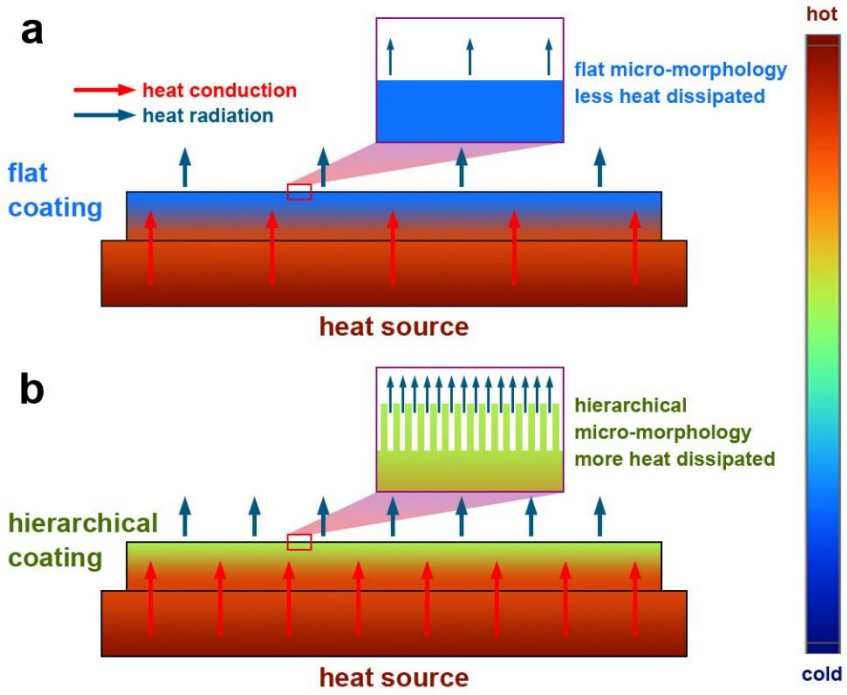

Figure 6. The comparison of the heat dissipation effect on between flat and vertically-aligned structured substrate.

1.3.3 Electrodes for advanced electrochemical energy storage devices

Since the early 21st century, using energy more efficiently and saving the limited energy sources have become critical worldwide. In recent years, researchers have been striving to discover new means to create energy sources. For example, energies from solar heating, photovoltaics, nuclear fission and fusion, wind blowing, hydropower, tidal fluctuation, biomass, and geothermal collection, are favorable alternatives to replace the

conventional combustion of fossil fuel. Scientific breakthroughs and technological innovations have been reported with increasing rate. The development of the advanced energy storage methods is very crucial to resolve the issue of energy deficiency. The exclusive research and industrial focus on the development of new energy sources cannot meet the current energy demands. The main reason is lack of efficient storage of the collected energy. Because the consumption rate of generated energy usually cannot be synchronized with the rate of generation. Fortunately, this problem has received attention from researchers and engineers around the world. Electrochemical energy storage devices (EESDs) [41, 42] are competitive candidates for energy storage. Lithium-ion batteries (LIBs) [43-51], electron double layer capacitors (EDLCs) as well as pseudocapacitors (PCs) [52-57], lithium–sulfur (Li–S) batteries [58-62], lithium–air (Li–air) or lithium–oxygen (Li–O_2) batteries [63-69], sodium-ion batteries [70-73], magnesium-ion batteries [74], lithium solid state batteries [75], among others are currently popular EESDs. Figure 7 briefly illustrates principles of the most popular types of EESDs [65]. Among those devices, LIBs are among the most interested. Since being initially commercialized by Sony, Inc. in 1990 [76], for more than a quarter of a century, the LIB has become a popular, portable, and rechargeable second battery used in various applications such as personal electronic devices [77], electric vehicles [78], hybrid electric vehicles [79], and smart grids [80]. To date, it is still needed to further improve the electrochemical performance of LIBs. The fabrication of novel and reliable electrode materials is critical for further development of better LIBs.

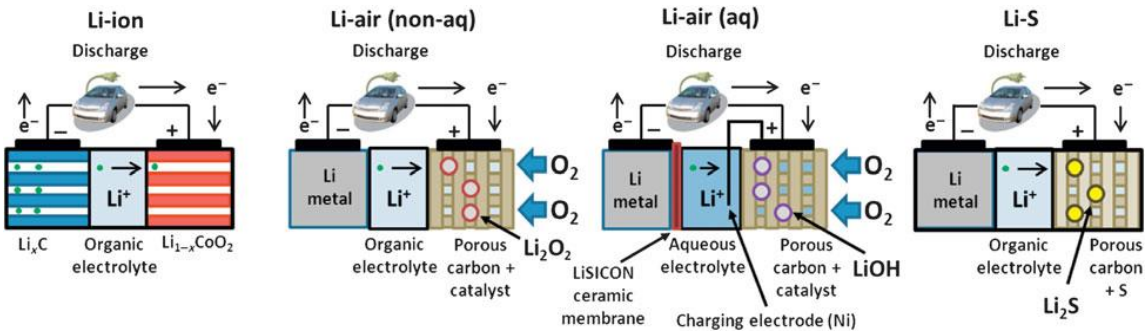

Figure 7. Schematic illustration of the general principles of four types of EESDs: lithium-ion batteries, lithium–air (non-aqueous) batteries, lithium–air (aqueous) batteries, and lithium–sulfur batteries [65]. Reprinted with permission from [65].

A LIB cell usually includes components of a solid-state positive electrode (cathode), a solid-state negative electrode (anode), some lithium-ion included liquid-state electrolyte (can be either non-aqueous or aqueous [81]), a polymeric separator, and a pair of the current collectors with encapsulated cases [43]. If an external voltage applied to both electrodes, lithium ions are deintercalated from cathode to anode through the electrolyte, so called the charging process; when there is an external loading applied to both electrodes, lithium ions are intercalated into unlithiated cathode from lithiated anode through the electrolyte again, i.e., the discharging process [43, 79, 82]. The discharging procedure of a LIB cell is shown in Figure 8 [79]. The role of the porous separator is to prevent the short circuit inside a cell. As the most significant components of one LIB cell, the properties of both cathode and anode materials determine the electrochemical energy storage ability of the cell. Therefore the selection of the electrode materials is a profound topic needs to be investigated.

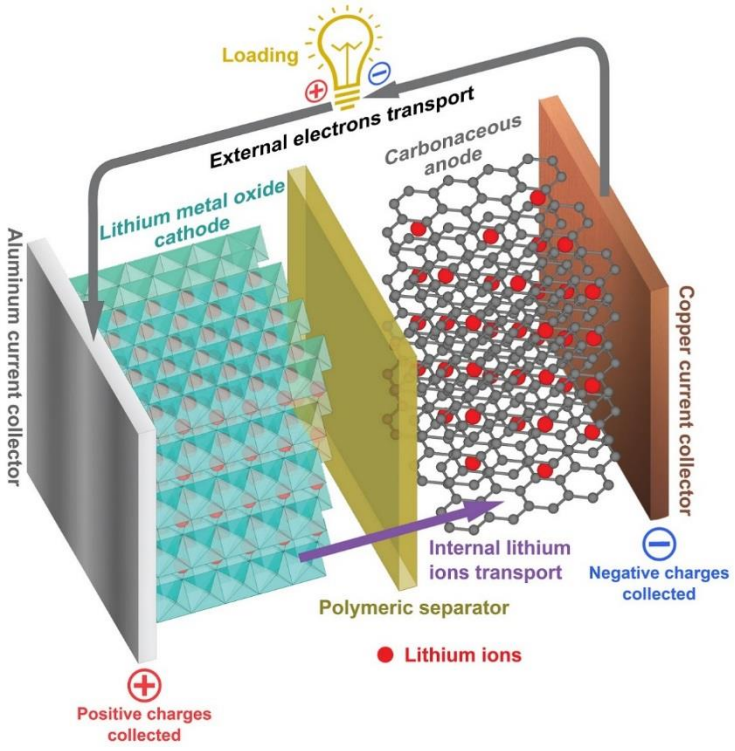

Figure 8. The schematic sketch of the structure of one LIB cell when it is discharged.

According to the illustration of Figure 8, it is apparent that both electrodes needs to be layered structure such that the lithium ions have sufficient spaces to be intercalated [79, 83, 84]. For anodes, the carbonaceous materials such as bulk/powder graphite, carbon black, and graphene are widely applied to LIB cells due to their layered structure and high reversibility of lithium insertions [83, 85]; For cathode, lithium transition metal oxides (LTMOs) [46] are favorable to be selected, because their layered structure, high theoretical specific capacity, high electrochemical potential versus Li/Li^{+}, acceptable reaction reversibility, among others [43, 86]. There are several LTMOs such as $LiCoO_2$ [87, 88], $LiNiO_2$ [89], $Li(Ni_{1/3}Mn_{1/3}Co_{1/3})O_2$ [90], $LiMn_2O_4$ [91], $LiFePO_4$ [92], which have become common cathode materials of LIBs cells for nearly two decades.

Nevertheless, the restricted capacity and cyclic performance of such bulk-sized conventional LTMOs cathode materials prompt to discover novel micro- and nano-structures in order to improve the performance of LIB cells [93]. Various transition metal oxide (TMO) nanomaterials that do not include lithium atoms, have attracted increasing attention. The main reasons are their high specific surface area, novel size effect, shorter ion diffusion pathway, obviously enhanced reaction kinetics, among others [45, 94]. Co_3O_4 [95], Cr_2O_3 [96], CuO [97], Fe_2O_3 [98], MnO_2 [99], NiO [100], SnO_2 [101], TiO_2 (both anatase [102] and rutile [103]), V_2O_5 [104-107], and ZnO [108]. Those TMOs have unique performance as cathodes since their properties of the molar masses, theoretical specific capacities, melting points, densities, and the insertion numbers of lithium ions are different.

Besides the synthesis and development of novel types of chemistry of active materials, hierarchical micro-architecture of the electrodes is also a type of reliable solution to improve the electrochemical performance of the LIB. The main advantages of the hierarchical electrode are 1) increased surface area to get reacted with lithium ions; 2) shorter pathway to transport the chargers; 3) more buffering space to accommodate the volume change during cycling; and 4) suppressed effect of the agglomeration of particles [79]. Therefore, the publications referring to the hierarchical electrode have an increasing amount in recent years. Despite the large amount of reports, most fabricated hierarchical nanoarchitecture were for active materials [109-111]. The as-fabricated 3D active nanomaterials need to be mixed with polymeric binder and conductive additives and then casted on a flat current collector. Such conventional slurry-casting-cell-

assembly approach as shown in Figure 9b results the severe agglomerations of active nanomaterials and interrupted ion transport pathways. That results in the difficulty to fully exploit active materials' advantages from their 3D nanostructures [112]. Moreover, the addition of polymeric binders can also reduce the specific capacity and increase the risk of the damage of electrodes at elevated temperature [113].

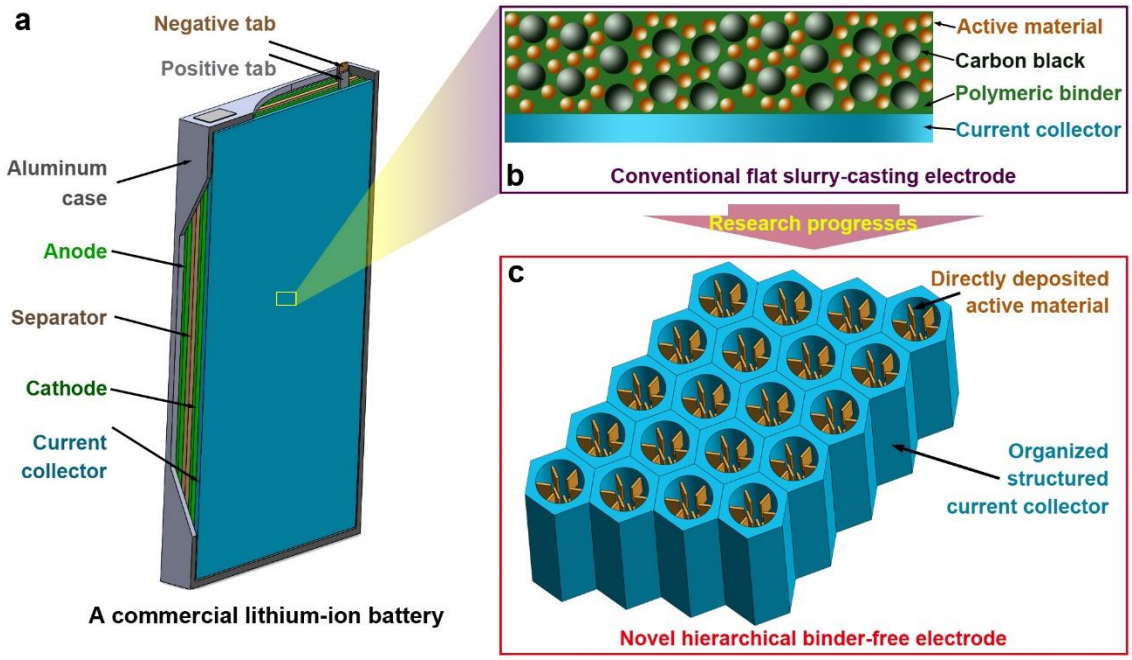

Figure 9. (a) The macroscopic structure of a commercial LIBs cell. The microscopic structure of (b) a conventional binder-used slurry-casting electrode and (c) a novel binder-free hierarchical electrode.

In this case, an alternative strategy to design hierarchical electrodes is introducing 3D hierarchical architecture for the whole electrode. The core idea is the direct deposition of nanostructured active materials on the surface of textured conductive current collector. Figure 9c demonstrates this design idea. This approach can prevent the negative effects from polymeric binder and slurry-casting process. Meanwhile, the

agglomeration and pulverization issues of active materials during cycling can be eliminated effectively. The usage of the binder-free cell assembly to joint active material and current collector is the main proposed strategy to fabricate hierarchical electrodes for LIBs.

1.4 Summary

In this chapter, a general overview of the concept and characteristics of hierarchical nanomaterials is presented. Typical experimental means to synthesize the hierarchical nanomaterials and nanocomposites are compared and contrasted. Different morphological features of hierarchical nanomaterials from 0D to 3D can promote the properties of various applications. Representative applications of superhydrophilicity or superhydrophobicity, enhanced heat dissipation, and excellent electrochemical energy storage performance are introduced. Particularly, the application to the advanced electrode materials for rechargeable batteries of hierarchical nanomaterials is emphasized.

CHAPTER II

MOTIVATIONS AND OBJECTIVES

For this doctoral research, the overall research motivations have two parts. This first one is the current urgent needs of the novel, reliable, scalable, and stable design of hierarchical nanomaterials and nanocomposites. The reason is the lacking of the applicable experimental approach to realize the proposed optimal design in the real product for the scalable functional applications. The second one is the deficiency of the theoretical understanding of the quantitative kinetics model to describe the electrochemical behavior of the hierarchical nanomaterials. This theoretical knowledge is quite significant to design the advanced electrode materials and structures for next-generation electrochemical energy storage.

2.1 Objectives

There are three major research objectives of this doctoral study that are addressed in the subsections below. The general research flowchart is demonstrated as Figure 10.

2.1.1 Fabrications of hierarchical nanocomposites consisting of metal and metallic oxide

The novel approaches to synthesize the novel types of hierarchical metal–oxide nanocomposites is the first and foremost part of this research. The creation of stable novel nanocomposites with hierarchical structures and fancy properties is the fundamental study referring to the chemical reaction, crystalline growth kinetics, and

condition control. The as-fabricated hierarchical nanomaterials with high yield and quality is the precondition of the realization of versatile applications.

2.1.2 Applications of as-fabricated hierarchical nanocomposites

Understanding unique properties and excellent performance of as-fabricated hierarchical nanomaterials for different applications is the second objective. Considering the different features and advantages of different types of nanomaterials, the reliability of fruitful applications such as wetting properties, heat dissipation, and electrochemical energy strange are evaluated.

2.1.3 Identification of theoretical factors for morphological and electrochemical properties

Besides the experimental studies described in the above two objective, the profound and convincing theoretical contribution is also a significant part of this doctoral research. The theoretical model to correlate the maximum electrochemical performance of a specific hierarchical electrode and its morphological parameter needs to be investigated, constructed, and evaluated.

2.2 Dissertation structures

In this dissertation, Chapter I presents an overall introduction of hierarchical nanomaterials and their fabrication approaches as well as applications. The part of motivations and objectives is given in Chapter II. Chapter III describes the details of the materials and methods used in this research. The fabrication and superhydrophilicity of a novel type of aluminum porous structure is presented in Chapter IV. The enhanced heat

dissipation of a hydrothermally deposited V_2O_5 hierarchical nanostructures is demonstrated in Chapter V. The excellent electrochemical performance of a type of hierarchical Cu/Ni/TiO_2 anode is illustrated in Chapter VI. A quantitative physical model to electrochemically evaluate the maximum capacity of a specific electrode under a specific charge-discharge condition is confirmed in Chapter VII. Finally, the general conclusions and future outlooks is summarized in Chapter VIII.

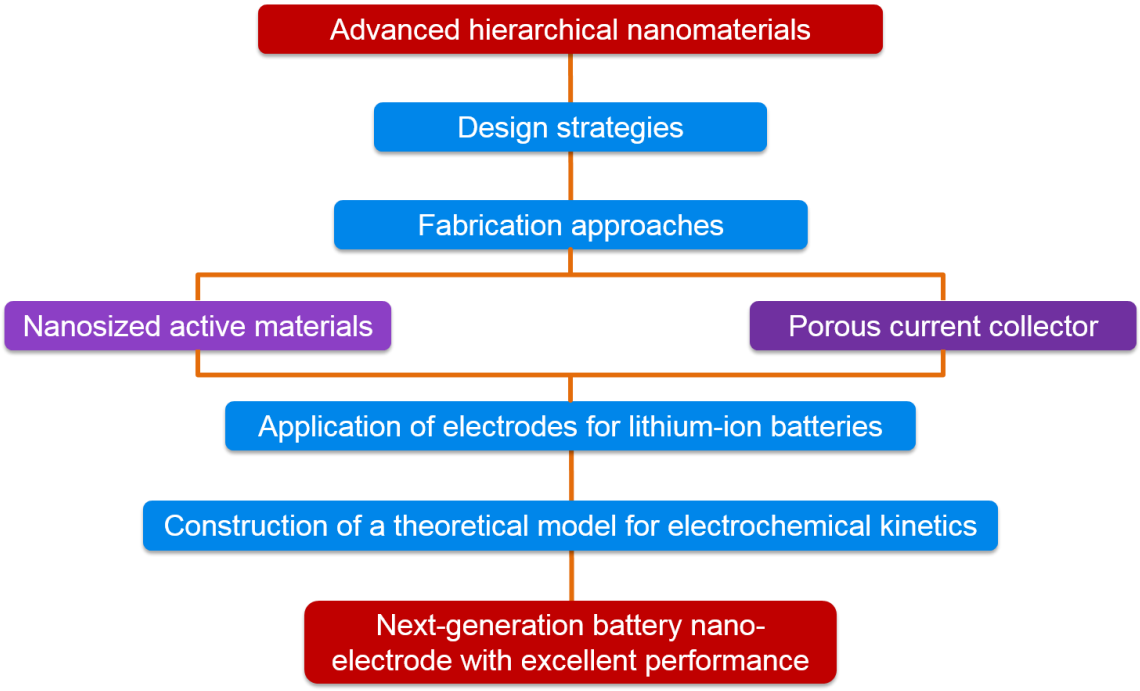

Figure 10. The overall flowchart of this doctoral research.

CHAPTER III

MATERIALS AND METHODS*

This chapter gives a general overview of the chemicals, reactants, experimental procedures, and characterization facilities applied in this research, presented in upcoming chapters in this dissertation. The materials and chemicals used are the fabrication steps to synthesis four types of hierarchical nanomaterials or nanocomposites are introduced at first. Then the specific methodologies to characterize various properties and performance of these as-fabricated nanomaterials are subsequently given.

3.1 Materials

All chemicals in this study were purchased and used without further purification. For the fabrication of aluminum porous structure, aluminum foil (household, 1100-type, aluminum purity ~99.00% with ~0.12% copper, minimal (unavailable) [114, 115], thickness is nearly 30 μm), perchloric acid (69-70 wt. %, Alfa Aesar), nitric acid (69-70 wt.%, Alfa Aesar), and ethanol (99.5%, 200 proof, VWR) were used.

---

*Part of this chapter reproduced with permission from "Electrochemical synthesis and hydrophilicity of micro-pored aluminum foil" by Yuan Yue, *et al.*, *Surf. Coat. Technol.*, **2017**, 309, 523-530 (Copyright © 2017 Elsevier); and "Super-hierarchical Ni/Porous-Ni/V_2O_5 Nanocomposites" by Yuan Yue, *et al.*, *RCS Adv.*, **2017**, 7, 40383-40391 (Copyright © 2017 Royal Society of Chemistry); and "Hierarchical Structured Cu/Ni/TiO_2 Nanocomposites as Electrodes for Lithium-ion Batteries" by Yuan Yue, *et al.*, *ACS Appl. Mater. Interfaces*, **2017**, 9, 28695-28703 (Copyright © 2017 American Chemical Society).

For the fabrication of Ni micro-channeled porous structure, as-purchased 110 copper sheet (99.90 wt.% Cu, McMaster-Carr, Inc.) with a thickness of 0.005 ± 0.0008 inch (0.127 ± 0.020 nm) and 200 Ni sheet (McMaster-Carr, Inc., 99.0% Ni, 0.13 mm thickness) were used as substrates for the electrodeposition of the nickel layer after thorough ultrasonication cleaning. A homemade double-electrode set-up including Ni sheet as cathode, graphite rod (6 mm in diameter, 99.995% carbon, Sigma-Aldrich) as anode, and an aqueous electrolyte of 0.2 M $NiCl_2$ (98%, Sigma-Aldrich) and various concentrations of NH_4Cl (≥99.5%, Sigma-Aldrich) was used for the electrodeposition of Ni micro-channels. The nanostructure of V_2O_5 nanosheets was conducted with the reactants of commercial V_2O_5 bulk powder (99.99% trace metals basis, Sigma-Aldrich) and H_2O_2 solution (30 % w/w in H_2O, contains stabilizer Sigma-Aldrich).

For the synthesis of the anatase TiO_2 nanoparticles (NPs), a facile wet-chemical synthesis was conducted based on the chemicals of cetyl trimethylammonium bromide (CTAB, purity >99.0%, Fluka), anhydrate ethanol (200 proof, 100%, VWR), and Ti(V) isopropoxide ($Ti[OCH(CH_3)_2]_4$, 97%, Sigma-Aldrich).

3.2 Fabrications of hierarchical-structured nanomaterials

3.2.1 Preparation of aluminum porous structure (APS)

To fabricate APS using electrochemical etching process, a solution was use that contained perchloric acid ($HClO_4$) and ethanol ($HClO_4$: ethanol = 1:4, volume ratio, hereinafter labeled as Cl-1-4 solution). The mixture of nitric acid (HNO_3) and ethanol with a volumetric ratio of 1:4 was prepared. This solution, marked as N-1-4, was used as

the reference. Figure 11 illustrates the general process of the fabrication of APS. Before etching process, the aluminum foil was cut into small pieces with dimensions of 1.5 inches x 1 inch (approximately 3.8 cm x 2.5 cm) followed by rolling. The flattened samples were pre-cleaned through rinsing by absolute acetone and ethanol successively. Most of the dust or contaminations on the surface of the aluminum foil could be removed due to absolute acetone and ethanol were strongly polar solvents.

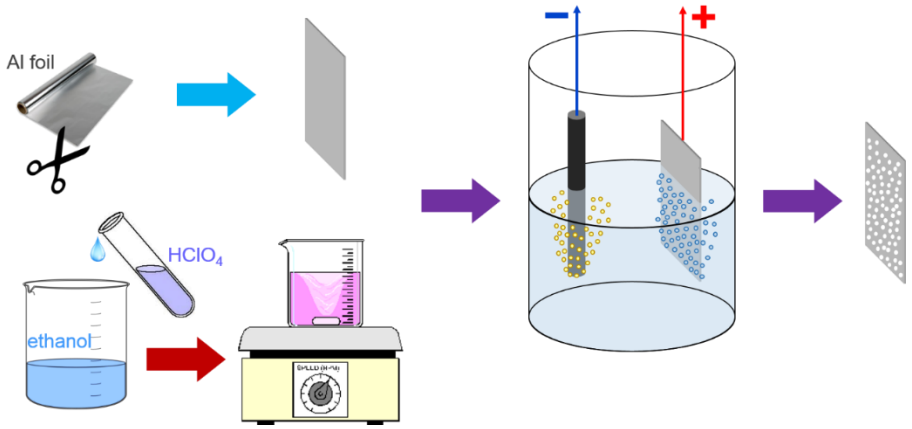

Figure 11. Illustration of the fabrication procedure of the aluminum porous structure (APS).

The electrochemical etching setup was constructed by a double-electrode system. The pre-cleaned aluminum foil was the working electrode and the high-purity graphite rod (>99.995%, Sigma Aldrich) acted as the counter electrode. During mounting, a positive alligator clip was clamped to the center of the edge of 1 inch length of the aluminum foil. The electrochemical etching was a galvanostatic process. The current density was set at 0.02 A/cm^2. The etching time were for 1, 2, 3, 4, and 5 minutes. The electrical potential fluctuated within the range of 3.0~3.3 V during the etching. The reference etching by the N-1-4 solution was also a galvanostatic process at 0.02 A/cm^2

for 1 and 3 minutes. All electrochemical etching processes in this research had no stirring of the electrolyte in order to get uniform treated samples. After etching, the sample was rinsed with absolute ethanol and acetone. Then the sample was dried in a vacuum oven for 2 hours.

3.2.2 Preparation of nickel micro-channeled substrate

The Ni micro-channeled microstructured layer was electrochemically deposited as the galvanostatic mode. Figure 12 illustrates the experimental approach of the electrodeposition. For Ni micro-channels coated on Cu substrate, i.e. Cu/Ni composites, the applied current density and duration of electrodeposition were constant as 0.4 A/cm^2 and 10 minutes, respectively. To investigate the effect of the concentration of ammonium ions, a series of samples were prepared using electrolytes with different concentrations of ammonium from 0.1 M to 4.0 M. Table 2 lists the detailed parameters of these samples with names of Cu/Ni-A to F. For Ni micro-channels coated on Ni substrate, i.e. Ni/Porous-Ni structure, an aqueous electrolyte of 0.2 M $NiCl_2$ and 4.0 M NH_4Cl was used. The applied current density and duration of electrodeposition were 0.5 A/cm^2 and 7 minutes, respectively.

After electrodeposition of Ni micro-channels, the sample was rinsed by acetone, deionized (DI) water, and ethanol thoroughly. Finally, the vacuum drying of the sample was accomplished at 60 °C overnight.

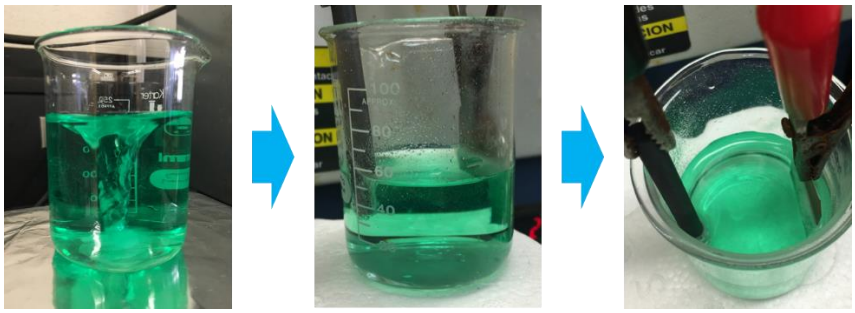

Figure 12. Experimental procedure of the electrodeposition of Ni micro-channeled microstructure.

Table 2. Experimental parameters of six sets of Cu/Ni micro-channeled samples.

Sample Name	Concen. of Ni^{2+} (M)	Concen. of NH_4^+ (M)	pH Value of Solution	Current Density (A cm^{-2})	Time Duration (min)
Cu/Ni-A	0.2	0.1	7.25	0.4	10.0
Cu/Ni-B	0.2	0.5	5.70	0.4	10.0
Cu/Ni-C	0.2	1.0	5.41	0.4	10.0
Cu/Ni-D	0.2	2.0	5.14	0.4	10.0
Cu/Ni-E	0.2	3.0	4.99	0.4	10.0
Cu/Ni-F	0.2	4.0	4.70	0.4	10.0

3.2.3 Synthesis of spherical anatase TiO_2 NPs

The experimental approach used in this research to synthesize anatase TiO_2 NPs was the modified method of a reported wet-chemical route [20]. In the first step, 4 mL 0.1 M CTAB aqueous solution was added into 60 mL anhydrate ethanol. After stirring this mixture with heat until it reached 65 °C, 2 mL Ti(V) isopropoxide was quickly dropped into the stirring mixture. A type of white blurred substance occurred immediately. Then the constant stirring at 65 °C continued for another 20 minutes. After stirring, the white suspension was cooled down naturally by aging it overnight. The white precipitation at the bottom was obtained. Figure 13 illustrates the brief experimental procedure and the white suspension after synthesis. The precipitation was

collected and rinsed by centrifugation in ethanol at 7000 rpm for 300 minutes. The white product was dried at 70 °C overnight followed annealing at 600 °C for 90 minutes. The temperature ramp was controlled as 10 °C/min. Finally, ~0.5 g white powder of anatase TiO_2 was synthesized.

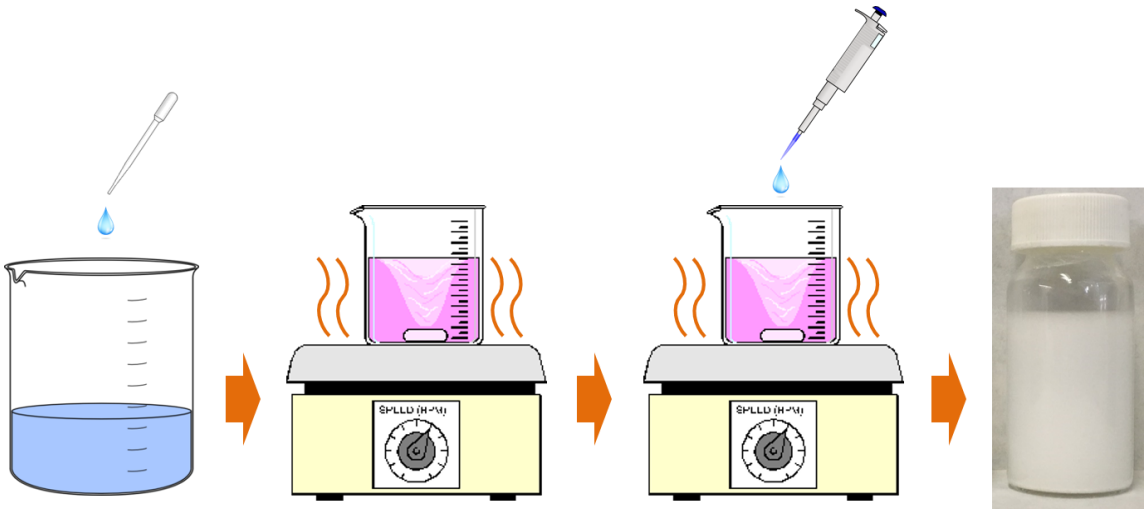

Figure 13. Schematic illustration of the wet-chemical synthesis of anatase TiO_2 nanoparticles.

3.2.4 Synthesis of V_2O_5 nanosheets and Ni/Porous-Ni/V_2O_5 nanocomposites

The multilayered and hierarchical 2D V_2O_5 nanosheets and micro-peonies were grown on the Ni/Porous-Ni substrate through a hydrothermal treatment. Figure 14 illustrates the general experimental synthesis pathway. 0.5 mmol (90.9 mg) of V_2O_5 bulk powder was firstly suspended in 23.5 mL DI water by magnetic stirring. After the formation of a uniformly distributed orange blur suspension, 1.5 mL H_2O_2 solution was added into the suspension dropwise. The transparency of the suspension mixture started increasing after continuous stirring for 10 minutes. The suspension completely became a clear and transparent solution with a little bubbling after 30 more minutes stirring at

room temperature. This light-orange-colored solution was then transferred to a sealed Teflon hydrothermal autoclave. The as-fabricated micro-channeled Ni/Porous-Ni substrate was directly placed into the solution inside the autoclave before sealing it. After the hydrothermal process at 180 °C for 7 hours, the sealed autoclave was cooled down naturally in the air. The product of dark green precipitation and the black Ni/Porous-Ni/V_2O_5 samples in the colorless transparent liquid was obtained. After rinsing by ethanol and DI water, both precipitation and Ni/Porous-Ni/V_2O_5 samples were dried at 70 °C in a vacuum overnight. Then, the annealing procedure was conducted in the Ar gas flow at 350 °C for 30 minutes. The temperature ramp was set as 5 °C/min. Finally, the product of dark-brown-colored dried powder of V_2O_5 and Ni/Porous-Ni/V_2O_5 sample were fabricated.

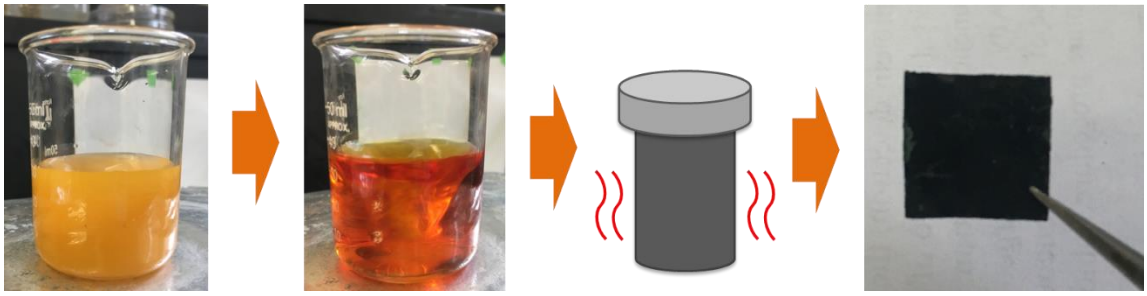

Figure 14. Illustration of the hydrothermal synthesis of V_2O_5 nanosheets.

3.3 Methods of characterization

3.3.1 Crystallographic and morphological characterizations

The morphological characterization of APS samples was carried out using digital optical microscope (VHX-600, Keyence Corporation), scanning electron microscope

(SEM) (VEGA II LSU, TESCAN ORSAY HOLDING, a.s.), and interferometer (NewView 600, Zygo Corporation).

The crystalline structures of Ni/Porous-Ni and V_2O_5 powders were characterized by the X-ray diffraction (XRD) instrument (Bruker D8 Focus Bragg-Brentano short-arm powder diffractometer) with a Cu Kα X-ray source (λ = 1.540598 Å). The morphological characterization of all samples was conducted at the SEM (FERA-3 Model GMH Focused Ion Beam Microscope, Tescan, Inc.) with an acceleration voltage of 10 kV. The X-ray energy dispersive spectroscopy (EDS) experiments were accomplished by the field emission SEM (JSM-7500F, JEOL, Inc.) with an acceleration voltage of 10 kV. The porous volume and estimated Brunauer–Emmet–Teller (BET) surface area were determined by conducting the nitrogen (N_2) adsorption–desorption experiment using ASAP 2010 (Micromeritics Instrument Corporation) at 77 K. Prior to experiments, the samples were degassed in high vacuum at 100 °C overnight to remove adsorbed gases and other impurities.

The crystalline structures of both Cu/Ni and anatase TiO_2 samples were characterized by the XRD instrument (Bruker D8 Focus Bragg-Brentano short-arm powder diffractometer) with a Cu Kα X-ray source (λ = 1.540598 Å). The morphological characterization of Cu/Ni samples was conducted by the SEM (Tescan VEGA II LSU) with the acceleration voltage of 10 kV. The morphological characterization of anatase TiO_2 samples was accomplished through the SEM (Tescan FERA-3 Model GMH Focused Ion Beam Microscope) with the acceleration voltage of 10 kV. The EDS mapping was conducted using an EDS detector (Oxford Instruments, Inc.) mounted on

the field emission SEM of JSM-7500F (JEOL, Inc.) and LYRA-3 Model GMH Focused Ion Beam Microscope (Tescan, Inc.).

3.3.2 Wetting angle testing

For the wetting angle test of the APS, a home built goniometer with a digital camera (60 frame per second) was used for the contact angle measurement. The droplet of ultrapure deionized water (Millipore) was used as liquid. All wetting angle tests were conducted at the stable and horizontal orientation. All fabrication and characterization experiments were repeated for five times. The following results in Chapter IV revealed the consistency of such repeated experiments. The analysis of optical microscopic photographs was accomplished using the image processing software of ImageJ.

3.3.3 Thermal imaging tests for heat dissipation measurement

The *in situ* heat dissipation measurement was conducted on a hot plate in atmosphere. An infrared thermal imager (Ti45, Fluke Corporation) was used to capture the infrared images of samples with calibrated temperature indicator.

3.3.4 Electrochemical characterization with coin-cell assembly

The electrochemical measurements of the Cu/Ni/TiO_2 anode were performed using a coin-type half cell (CR 2032). The working electrode of Cu/Ni/TiO_2 was assembled through a typical slurry-casting method. 80 wt% of as-synthesized anatase TiO_2 powders, 10 wt% conductive additive of carbon black (Super C65, Timcal), and 10 wt% PVDF as the polymeric binder (polyvinylidene fluoride, Kynar) were mixed uniformly by grinding and ball milling for 30 minutes with the addition of the N-methyl-2-pyrrolidone (NMP, Sigma-Aldrich) solvent. After obtaining the grey-colored

homogenous slurry, it was spread onto the surface of six sets of Cu/Ni current collectors listed in Table 3. The casted anode was dried overnight at 70 °C in the air. In order to achieve and maintain uniform dispersion of TiO_2 nanoparticles, these methods have been used: grinding, magnetic stirring, long-time ball milling, and immediate casting after mixing. The coin-cell assembly was conducted in an Ar-filled glove box. The moisture and oxygen concentrations in the glove box were both maintained below 0.1 ppm. The electrolyte used here was the typical solvent of 1 M $LiPF_6$ in a 1:1 (v/v) mixed solvent of ethylene carbonate (EC) and diethyl carbonate (DEC) purchased from BASF SE. The lithium metal (99.0%, Sigma-Aldrich) was used as the counter electrode. For comparison, the as-annealed TiO_2 NPs were also casted on the surface of an as-cleaned flat Cu current collector to make a half-cell. This sample was named as flat Cu.

Table 3. The statistical result of the loading mass of TiO_2 NPs for all seven samples.

Sample Name	Mean value of loading mass (mg/cm^2)	Standard deviation of loading mass (mg/cm^2)
Flat Cu	1.98	0.08
Cu/Ni-A	2.04	0.05
Cu/Ni-B	2.08	0.08
Cu/Ni-C	2.24	0.05
Cu/Ni-D	2.3	0.07
Cu/Ni-E	2.38	0.08
Cu/Ni-F	2.48	0.08

The tests of cyclic voltammetry (CV) and electrochemical impedance spectroscopy (EIS) were conducted at a scan rate of 0.1 mV/s within the potential interval of 0.01–3 V (vs. Li^+/Li). The alternating current (AC) perturbation signal was ± 10 mV and the frequency had a range from 10 mHz to 1 MHz. The charge-discharge

cyclic tests were performed within the potential interval of 0.01–3 V (vs. Li^+/Li) at various C-rates (1 C = 335 mA/g).

3.4 Summary

In this chapter, synthesis, fabrication, and characterization of five kinds of novel hierarchical-structured nanomaterials are introduced. They are categorized as two types, i.e. porous metallic substrates and novel oxide nanoparticles. The aluminum porous structure (APS), Cu/Ni micro-channeled composites, and Ni/Porous-Ni micro-channeled microstructures are assigned as the first type. Spherical anatase TiO_2 nanoparticles and ultrathin V_2O_5 nanosheets are second type.

The porous and high surface area properties of the first type of metallic substrate are characterized by the surface morphological measurement and corresponding statistical analysis. Meanwhile, the enhanced hydrophilicity of APS has been validated through the wetting angle tests based on the dropping of water droplets. The nanostructured hierarchical morphologies of anatase TiO_2 nanoparticles and ultrathin V_2O_5 nanosheets are evaluated through the SEM imaging and EDS elemental mapping. The excellent heat dissipation performance of ultrathin V_2O_5 nanosheets as a novel coating on metallic substrate is confirmed. Furthermore, the electrochemical kinetics of anatase TiO_2 nanoparticles is investigated through the LIB anode cyclic testing.

CHAPTER IV

ALUMINUM POROUS FOIL WITH ENHANCED HYDROPHILICITY*

This chapter demonstrate a facile and cost-effective method to fabricate an unprecedented macropore-arrayed structure on an aluminum foil through electrochemical etching. Morphological characterization and mechanism of the pores formation are exhibited. Further examination showed that the surface hydrophilicity was improved due to the existence of pores.

4.1 Morphological features of aluminum porous foil

The morphology of the as-fabricated APS was characterized using digital optical microscopy. Figure 15 shows the optical microscopic photographs as compared with a reference aluminum foil. The initial surface has the morphology of a flat surface with parallel grooves, as detailed in Figure 15a. The grooves were induced through rolling during manufacturing [116]. After etching the aluminum foil in the Cl-1-4 solution under the galvanostatic mode (current density 0.02A/cm^2) for 1, 3, and 5 minutes, a porous array was observed as indicated in Figure 15b-d. Three panels in Figure 15 showed the increase in the pores density in etching time. According to the inset of Figure 15d, the through pores can be verified by light transmission. For the comparison, the aluminum

* Part of this chapter reproduced with permission from "Electrochemical synthesis and hydrophilicity of micro-pored aluminum foil" by Yuan Yue, *et al.*, *Surf. Coat. Technol.*, **2017**, 309, 523-530 (Copyright © 2017 Elsevier).

foil sample was immersed into the Cl-1-4 solution without the applying of the current. After 5 minutes, there was virtually no corrosion or etching that could be observed. This suggested that the usage of the galvanostatic current loading was the key point to form the porous structure.

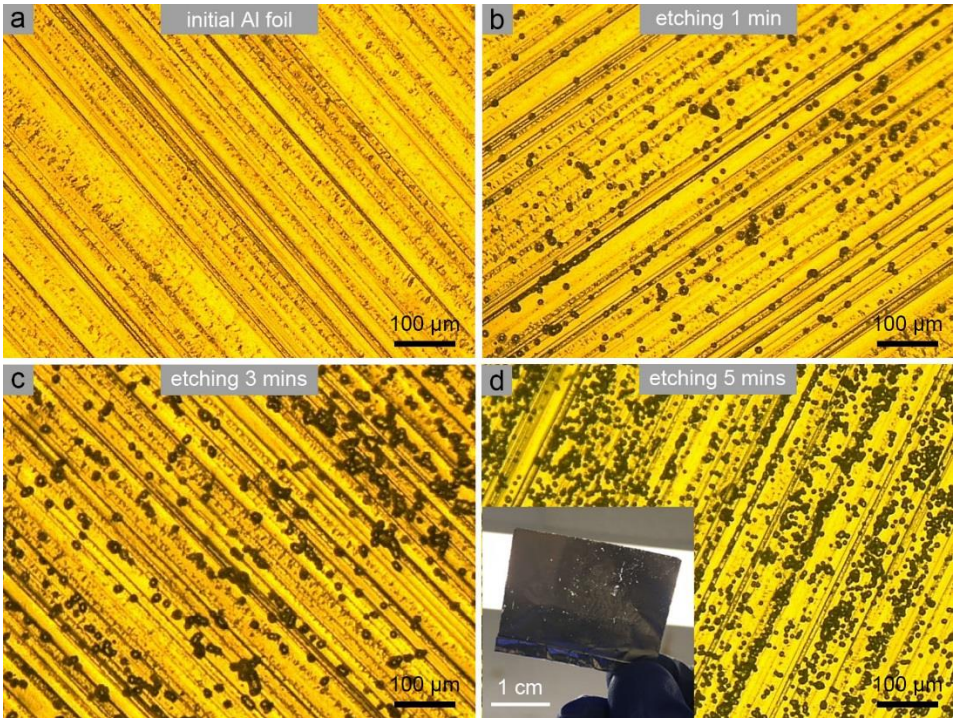

Figure 15. The digital optical microscopy photographs of the aluminum foil samples. (a) The surface image of the as-cleaned aluminum foil before etching. The morphology of the aluminum porous structures (APS) of aluminum foil after the etching treatment by the Cl-1-4 solution at 0.02 A/cm^2 for (b) 1 min, (c) 3 mins, and (d) 5 mins. The inset of the panel d is the digital camera photograph for the as-etched-for-5 mins APS.

To quantify the distributions of the number density and the average diameter of pores, statistical analysis was conducted based on the optical microscopic images. Two histograms were constructed (Figure 16) based on the statistical analysis of the APS samples of etching for 1 to 5 mins. In Figure 16a, it is apparent that the growing number of etched pores per unit area (5-40 pores per 0.1 mm * 0.1 mm) with the longer etching

time; On the other hand, mean diameters of pores only have narrow fluctuation, i.e. 11-17 μm, as can be seen from Figure 16b. This tendency suggested that longer etching time only caused denser distribution of pores but the diameter of pores kept stable with increased duration of treatment.

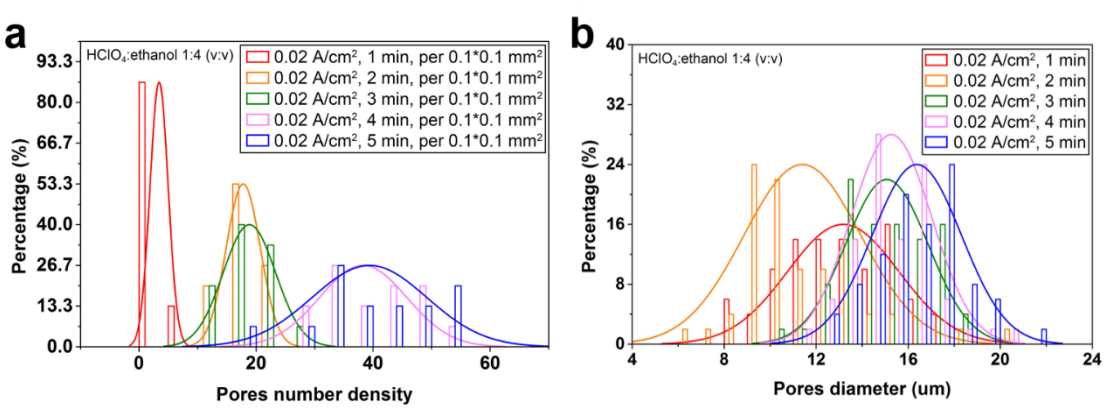

Figure 16. The histogram distribution diagrams for the APS samples with the etching time durations of 1, 2, 3, 4, and 5 mins. (a) The distributions of pores number densities per 0.1 x 0.1 mm^2. (b) The distribution of pores diameters. All data here was selected from the digital optical microscopy images of the corresponding APS samples.

The experiment of surface profile measurement by the interferometer imaging provided more evidence of the formation of porous array structure after etching in Cl-1-4 solution. In Figure 17a and c, the arithmetic and root-mean-squared surface roughness of the reference sample (pristine Al foil after cleaning) were R_a=0.27 μm and R_q=0.35 μm, respectively. This implied that the pristine aluminum foil had the smooth surface. After applying etching in Cl-1-4 solution at 0.02A/cm^2 for 20 seconds, 1 minutes, and 3 minutes, there were some pores emerged at the surface of the aluminum foil. This was illustrated by the porous morphology at the surface in the interferometer color mapping Figure 17b, e and f. The dark blue color at most of the pores region and the depth

profiles in Figure 17d, g and h revealed that the depth of pore channels was around 30 μm for all samples with etched pores, which was approximately the thickness of the aluminum foil.

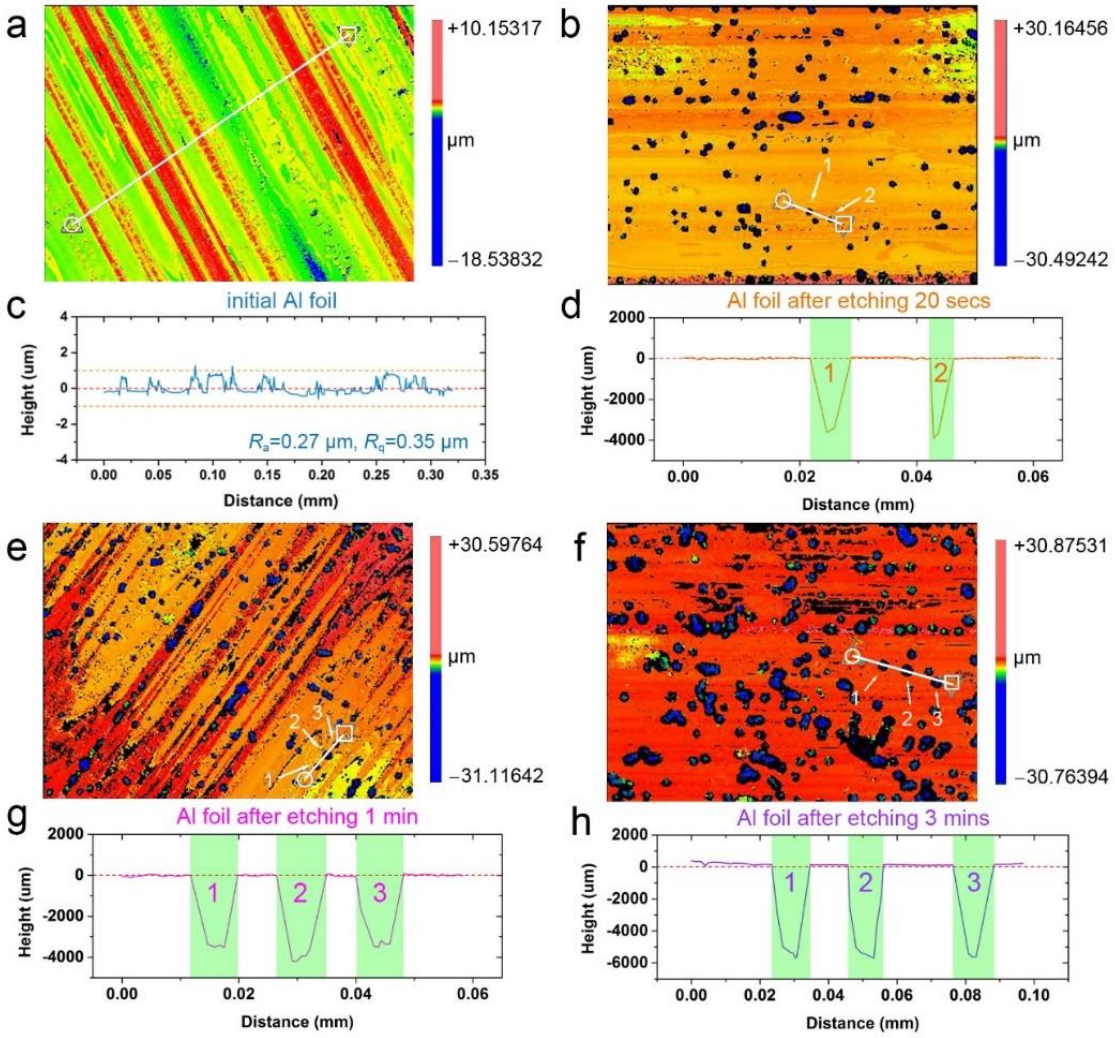

Figure 17. The surface interferometer images and profiles of the APS at etching for different durations. (a) The surface map of one region of the as-cleaned aluminum foil. The surface map of the APS sample which is treated by the Cl-1-4 etching for (b) 20 seconds, (e) 1 minute and (f) 3 minutes. (c)-(d) and (g)-(f) The surface profile plotting of the white line in (a)-(b) and (e)-(f).

The morphology of the fully-penetrated pores of the APS sample was also illustrated by the scanning electron microscopic imaging. Figure 18 shows the top view

of the porous morphology of an APS sample after the treatment by Cl-1-4 electrolyte for 3 minutes. The black holes in Figure 18 are the locations of the porous channels whose diameters were estimated as 5-10 μm. The cross section view of the etched APS sample was also observed through the SEM imaging. As shown in Figure 19, the morphology of numerous vertical channels are clear seen. A few blue arrows mark the positions of some surface pores. Their corresponding penetrated channels are indicated through yellow arrows. These channels were visible due to they were intersected with the cut facet. Furthermore, there were few etched rings or caves on the channel walls because of the continuous etching process inside channels after their formation. Red dashed ellipses in Figure 19 marked locations of the etched rings or caves.

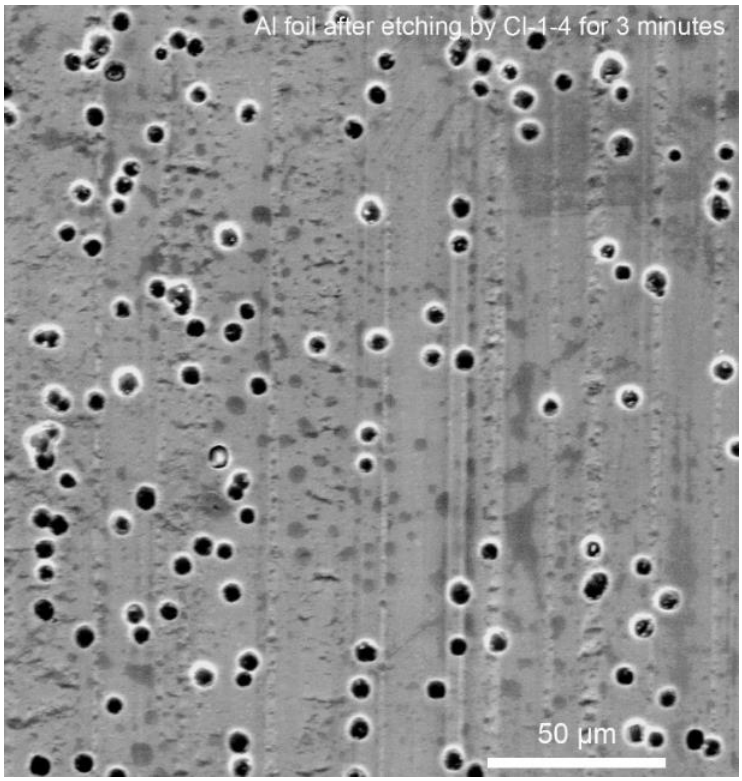

Figure 18. The top-view SEM image of the APS sample which is treated by the Cl-1-4 etching for 3 minutes.

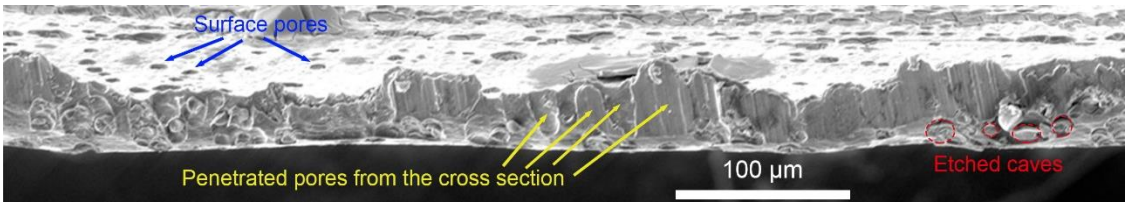

Figure 19. The side-view SEM image of the cross-section of the APS sample which is treated by the Cl-1-4 etching for 3 minutes. Several surface pores are pointed by blue arrows and the corresponding penetrated channels are highlighted by yellow arrows. The etched caves at the wall of channels are marked by red dashed circles.

4.2 Formation mechanism of porous structure

The formation of pores on a surface was distinct with electrochemical corrosion effect led by other acidic conditions. In order to confirm this, a set of reference experiments were conducted with the identical aluminum foil samples. After electrochemical treatment with 0.02A/cm^2 for 1 and 3 minutes by using the N-1-4 solution, a uniformly corroded surface on aluminum foil was observed in Figure 20. The porous morphology emerged by the treatment of Cl-1-4 was significantly different with the uniformly corroded surface. This is only uniformly corroded surface that can be observed in Figure 20c-d for samples etched by N-1-4 solution. This suggests the significant contribution from the ion group of perchlorate.

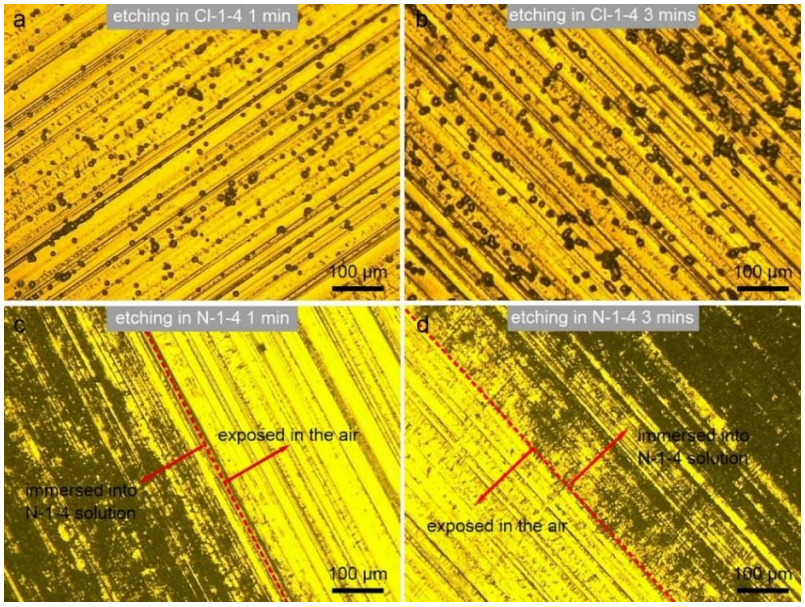

Figure 20. The comparison of the reaction effects of the etching aluminum foil samples inside the Cl-1-4 and N-1-4 solutions. The morphology of the aluminum porous structures (APS) of an aluminum foil sample after the etching treatment by the Cl-1-4 solution at 0.02 A/cm^2 for (a) 1 minute and (b) 3 minutes. The uniformly corroded dark surface of the aluminum foil samples after the treatment by the N-1-4 solution at 0.02 A/cm^2 for (c) 1 minute and (d) 3 minutes.

Morphological characterization using SEM accompanied with the chemical reaction analysis were carried out. The purpose of these efforts were to investigate the mechanisms of the formation of pores in Cl-1-4 solution. Figure 21 exhibits the SEM images during the formation procedure of the porous structure in the time scale. As shown in Figure 21a, the preliminary morphology of the etched rings array could be noticed after etching for 20 seconds. After etching for 1 minute, it is notable from Figure 21b that the un-etched inner regions surrounded by nearly a half of etched rings started cracking into two or more pieces. If the etching reaction continued, for instance etching for 2 minutes (as illustrated in Figure 21c), almost every single etched ring had accompanying cracks, which were the main components of a pore structure. The

magnified SEM image of the inset of Figure 21c reveals a typical morphology of cracks inside an etched pore. If the time duration of the etching continuously increases, the eventual morphology of porous arrays was formed, as shown in Figure 18. Detailed discussion will be provided later.

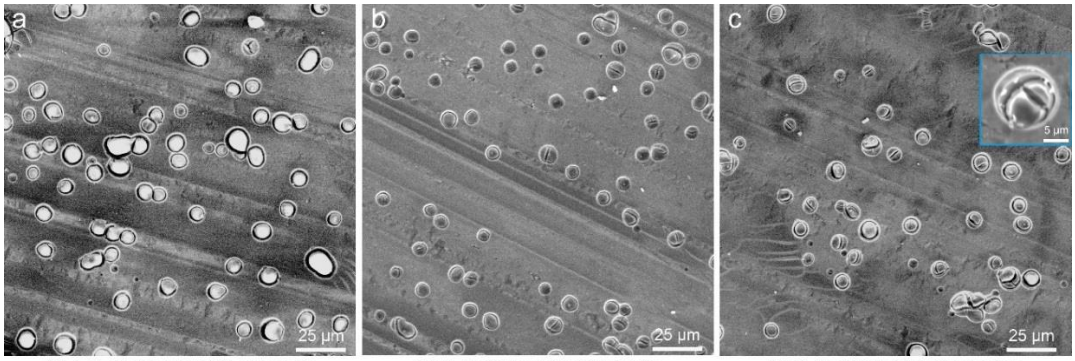

Figure 21. The time-dependent formation process of the etched pores at the surface of the Cl-1-4 treated aluminum foil revealed by the SEM images. (a) The morphology of the surface of APS after 20 seconds etching, the preliminary structure of etched rings are dominated. (b) The morphology of half rings and half rings with cracks of the surface of APS after 1 minute etching. (c) After etching for 2 minutes, the main morphology of pores is rings with cracks. The inset of panel d is a magnified image of one pore after etching for 2 minutes

The physical process and chemical reactions involved in the formation of the APS need to be understood. Due to the metal of aluminum ($Al^{3+} + 3e^{-} \leftrightarrow$ Al (s) E^0 = −1.676 V) is easier to get reacted with the acidic solution than copper ($Cu^{2+} + 2e^{-} \leftrightarrow$ Cu (s) E^0 = +0.340 V) [52] and the copper has very tiny composition percentage (~0.12%) in 1100 aluminum foil, there is no visible effects of copper impurity on the porous etching phenomenon of the 1100 aluminum foil. According to experimental results, the N-1-4 solution results in uniform corrosion while, the Cl-1-4 in porous structure. Owing to HNO_3 and $HClO_4$ have common proton cations and different oxoanions (i.e. NO_3^- vs. ClO_4^-), the role played by the perchlorate ion (ClO_4^-) during the formation of the unique

porous structure cannot be neglected. The typical etching process of the aluminum foil sample in the Cl-1-4 solution is the reaction that has vigorous bubbles formation on both electrodes, i.e. the working electrode (anode) of the aluminum foil and the counter electrode (cathode) of the graphite rod. Figure 22a reveals this phenomenon. The chlorine gas (Cl_2) can be released from the surface of the graphite cathode. The corresponding reduction reaction involving the perchlorate and the proton is listed as Equation (1).

Cathode: $ClO_4^- + 8\ H^+ + 7\ e^- \rightarrow ½\ Cl_2 + 4\ H_2O$ (1)

Anode: $2H_2O \rightarrow O_2 \uparrow + 4\ H^+ + 4\ e^-$ (2)

Overall: $4ClO_4^- + 4\ H^+ \rightarrow 7\ O_2 \uparrow + 2\ Cl_2 \uparrow + 2\ H_2O$ (3)

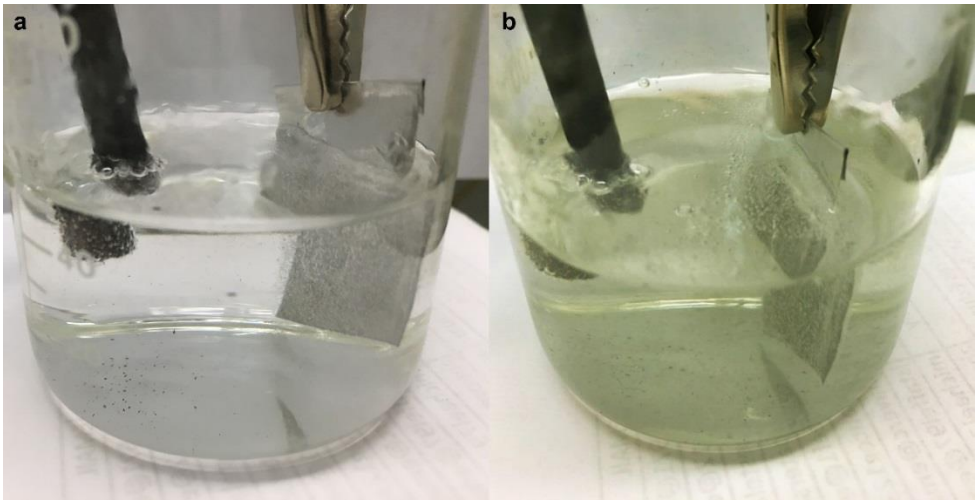

Figure 22. The digital camera photograph of the Cl-1-4 solution before (a) and after (b) long time usage. The vigorous gas bubbles can be observed during the reaction. The reaction-produced and dissolved chlorine gas makes the colorless solution turn into yellowish.

Moreover, the transparent solution of the Cl-1-4 will turn into yellowish after being used for reaction for repeated times, as shown in Figure 22b. The yellowish color suggests the accumulation of the released chlorine gas dissolved into the solution. This is

a convincing evidence to prove the formation of chlorine gas. On the other side, the water inside the as-purchased perchloric acid solution can undergo the oxidation reaction of releasing oxygen as described in Equation (2), which can combine an overall redox reaction of Equation (3) with Equation (1). The reaction of Equation (2) takes place at the surface of the aluminum anode. In one word, the overall reaction involving perchlorate ions results in the formation of Cl_2 gas released on cathode and O_2 gas on anode.

In addition to the formation of oxygen bubble, the contribution of the ethanol molecules in the Cl-1-4 solution mixture is considered. It is important to note that the spatial orientation of the ethanol molecule can be guided since ethanol molecule is polar with the dipole moment of 1.7 Debye [117]. According to this, the positively charged surface of the aluminum foil anode is able to offer electrostatic potential to attract the negative terminals (δ^-) of polar ethanol molecules. The sketch in Figure 23a suggests that such ethanol molecules should be adsorbed onto the positively charged surface of the aluminum foil. The reason that the aluminum surface has a net positive charge is the electron deficiency as a result of the electron transport towards the external circuit. The surface region where the ethanol molecules adsorb onto cannot provide the available sites to react with the perchloric acid. This is due to the fact that the sites are blocked by the adsorbed ethanol layer [118]. Only the randomly distributed surface region that is exposed to the perchlorate and hydrogen ions can participate in the reactions of Equation (1), Equation (2), and Equation (3). With the contribution of the minimal amount of the

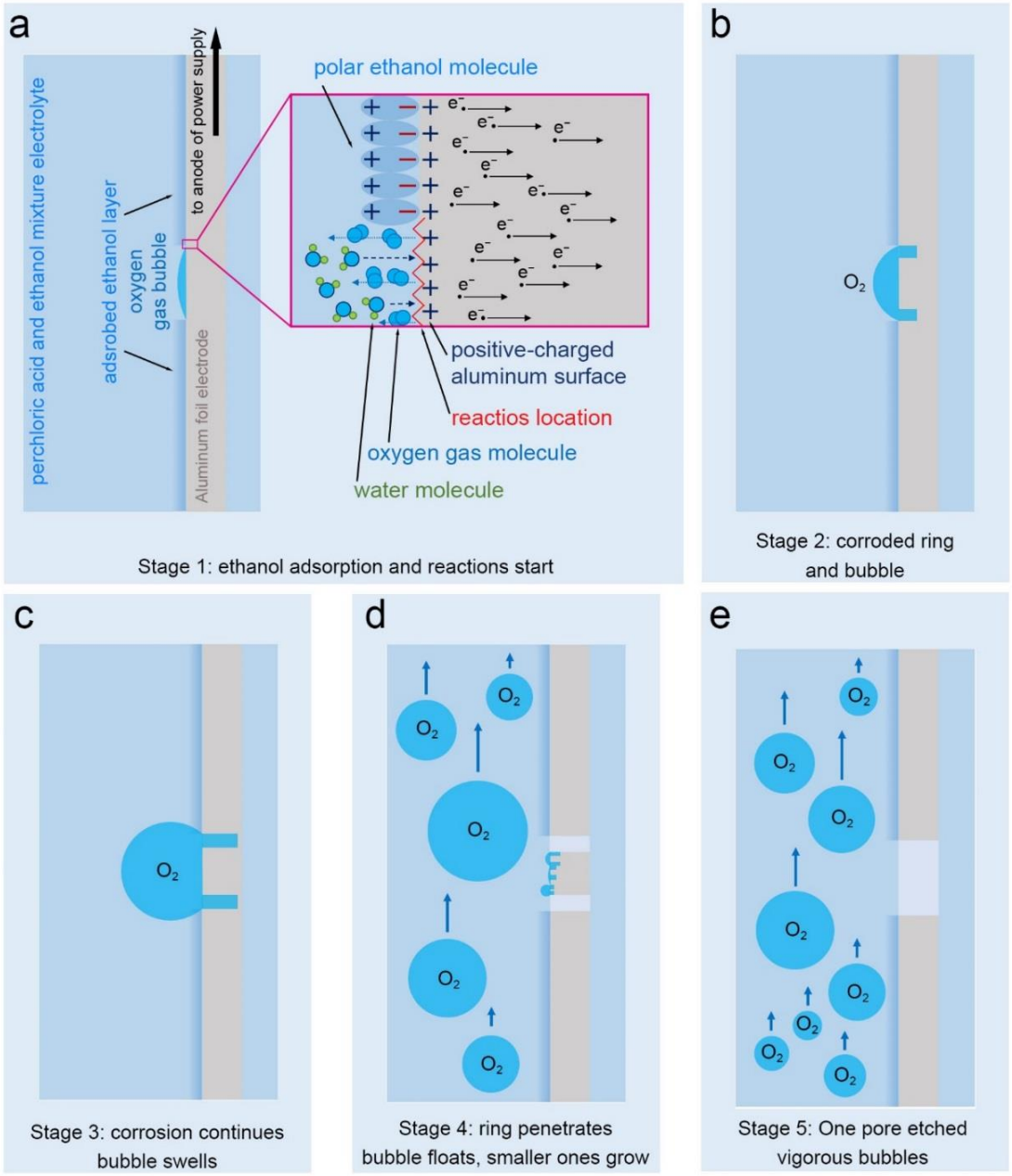

Figure 23. The sketch to describe the process of the formation of the APS. (a) The first stage of the adsorption of polar ethanol molecules and the initial formation of a flat oxygen bubble. The inset provides a detailed drawing in the zoomed scale. (b) The second stage of the swelling of the bubble and the etching of the ring region. (c) The third stage of the continuously growing bubble and etched part. (d) The fourth stage of the floating of bubbles and the starting of the subsequent etching at the inner part. (e) The fifth stage that the porous channel forms and numbers of oxygen bubbles are floating up.

copper impurity, the etching reactions are able to take place initially at such randomly selected pitting sites [119].

After the reactions start, the immediate releasing of oxygen can form an initial flat oxygen bubble, which occupies all available sites without the ethanol adsorption, as depicted in Figure 23a. Because the formation of oxygen bubbles can be regarded as another obstacle, the inner part of the reacted surface inside the bubble cannot continue participating in the reaction. At this time, the etching process exclusively begins nearby the interface of the oxygen gas, electrolyte solution, and the aluminum surface, which is the outer ring region of the bubble as represented in Figure 23b.

The etching process is attributed to the acidic corrosion reaction of the aluminum and perchloric acid. The swelling of the bubble and deepening in etched rings occur simultaneously (as illustrated in Figure 23c). Figure 23d demonstrates the floating towards the electrolyte-air interface of the swelled bubble. The floating is triggered after the volume of the bubble exceeds the threshold that the buoyancy of the bubble overcomes the surface tension at the triple interface. Subsequently, the inner part of the reacted aluminum surface can get exposed to the electrolyte solution. With it being partially hindered by polar ethanol molecules, some similar formations of the smaller bubbles start. This is a symbol of the cracks in the ring regions represented in Figure 21b and c. Eventually, a pore channel can be etched with several bubbles floating, as described in Figure 23e. Generally speaking, the etching of the porous channel structure onto the aluminum foil by Cl-1-4 solution can be identified as a synergetic interaction of the adsorption of ethanol molecules and the reaction participated by protons, perchlorate

ions, and electrons. This interaction consists of three phases of adsorption and the hindering effect of ethanol molecules, oxygen bubble formation on the aluminum surface and chlorine gas formation on the graphite surface, and the etching led by acidic corrosion successively.

4.3 Enhanced hydrophilicity and mechanism

As discussed earlier, the APS has a unique morphology with pored structures. The core characteristics of increased specific surface area and altered hydrophilicity can be utilized in many ways. For example, they offer more available sites to adsorb or deposit active micro- and nano-materials for the usages of heterogeneous catalysis [120, 121], hierarchical electrodes for the energy storage device [79, 122], hybrid functional composites [123-125], and many others. The hydrophilicity of the aluminum foil surface was increased by the porous channels. Figure 24a plots the decreased contact angles of DI water, as well as the increased hydrophilicity of samples etched for from 1 to 5 minutes. The inset with the orange margin of Fig. 6a is an example. It illustrates the APS etched for a relatively long time (i.e. 5 minutes) possesses the near-superhydrophilic surface [126, 127]. The corresponding contact angle here is as low as $\theta = 15.52°$. The reason behind this phenomenon is due to the extra vertical capillary force. If there were no porous channels on samples, the contact angle of such a smooth surface is ~62° (Fig. 6a). In this case, the water droplet can be stable with high contact angle. As shown in Figure 24b, this is the result under the combined effects of the horizontal capillary force from the center of the wetted region towards the air-water-aluminum triple interface, the

viscous force, and the surface tension of water [128, 129]. Nevertheless, after introducing the porous channel array on the surface of the aluminum foil, a new capillary force, i.e. capillary force II in Figure 24c, gets involved into the process to stabilize the water droplet. The capillary force II along the vertical direction of the porous channels provides additional water flows. Such flows allow the water inside the droplet to penetrate the channels.

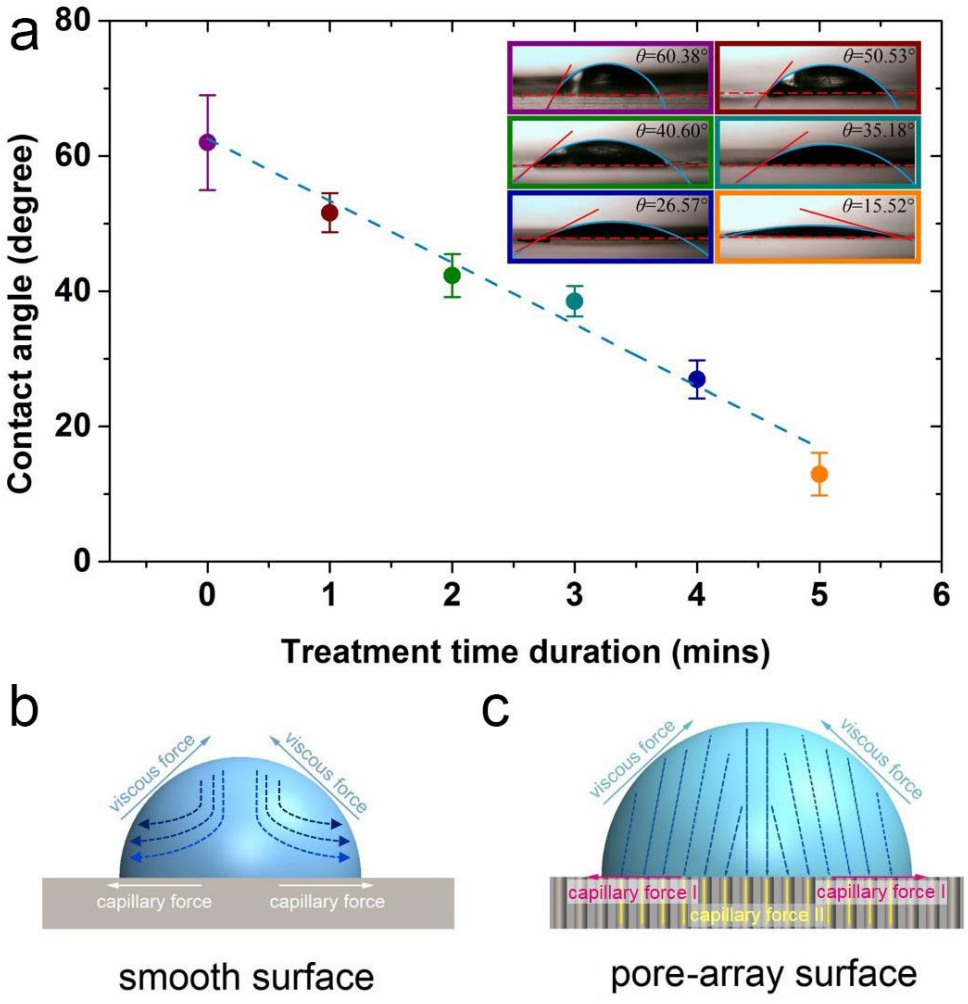

Figure 24. The feature of the near-hydrophilic surface of the APS. (a) The plot to demonstrate the decreased contact angles with the elongated etching time duration. The insets of this panel exhibit the digital photographs of the contact angle. (b) The sketch of the water droplet on the smooth surface. (c) The sketch of the water droplet on the pores-array surface.

As a result, the contact angle is significantly smaller than that on the smooth surface. Furthermore, the increased pore number density improves the efficiency of the extra capillary force II, which suggests the decreased contact angles. This offers wide applications. One example is to fabricate the uniformly distributed colloidal particles assembled layer [130-133]. The assembled layer will prevent the formation of the uneven "coffee-stain" effect caused by aggregated particles [38, 134-136].

4.4 Summary

In this chapter, a facile, quick, and efficient experimental approach was developed to fabricate APS on as-received foils. The unique surface morphology of the randomly distributed porous channel array with the mean diameter of 11~17 μm was confirmed using characterization techniques such as digital optical microscopy, scanning electron microscopy, and optical interferometer imaging. Through analyzing the pores after a series etching time, a general rule was discovered that the number densities of pores increased while their diameter distributions remained constant. Through experimental and theoretical analysis, the electrolyte solution of the mixture of the perchloric acid and ethanol played important roles for the formation of the porous channel array. The progressing corrosion that took place at the solid-liquid-gas interface promoted the formation of porous channels. The hindering effect of the polar ethanol molecule provided limited sites for reactions. The innovation of this work lie in the cost-effective method to fabricate pores on household aluminum foil (thickness < 50 μm) at a low electrochemical current loading (0.02 A/cm^2). This fabrication approach was facile,

energy-saving, safe, and the material used was cost-effective. The as-fabricated APS samples had improved hydrophilicity than as-received aluminum foils. Reduced contact angle with longer etching time meant that there was an effect led by the extra capillary force along porous channels.

For future outlook, the size and spatial distributions of current as-fabricated pores on the surface of aluminum foil need some improvement. Due to this fabrication was a localized etching without templates, the exact size and shape of each formed bubble were extremely hard to be well tuned. More precise control of the pore dimension and the optimization of the pore distribution will be undertaken in order to prepare well-defined and circular-shaped pores with uniform size and spatial distributions. The behavior of high-purity aluminum will be examined in comparison with the present study in order to understand effects of impurities on nucleation of pores. The APS will become a competitive candidate of the substrate for the hierarchical hybrid composite synthesis and the scalable manufacture of the well-distributed assembled layer of colloidal particles, at a low-cost.

CHAPTER V

IMPROVED HEAT DISSIPATION OF VANADIA-BASED NANOCOMPOSITE*

This chapter describes the fabrication and characterization of a novel super-hierarchical Ni/Porous-Ni/V_2O_5 nanocomposite was designed and synthesized through a simple two-step approach. Vertically-aligned micro-channels were formed as the unique and characteristic as-electrodeposited Ni/Porous-Ni substrate. The formation mechanism of ultrathin 2D V_2O_5 nanosheet arrays on Ni/Porous-Ni was explained according to an atomic structure model. The super-hierarchical Ni/Porous-Ni/V_2O_5 nanocomposite possessed an excellent heat dissipation.

5.1 Crystallography and morphology of Ni/Porous-Ni/V_2O_5

The as-fabricated Ni/Porous-Ni/V_2O_5 nanocomposites have uniform morphology along with well-crystalline structures. Figure 25 illustrates the overall physical properties of Ni/Porous-Ni/V_2O_5 nanocomposites characterized using the low-magnified SEM and XRD. The densely distributed vertically-aligned micro-channels of Ni/ Porous-Ni substrate is exhibited as Figure 25a. The diameters of those micro-channels span from 10 to 20 μm. According to the previous report [137], this was the result of selective deposition of Ni owing to the numerous H_2 bubble streams during electrodeposition

---

*Part of this chapter reproduced with permission from "Super-hierarchical Ni/Porous-Ni/V_2O_5 Nanocomposites" by Yuan Yue, *et al.*, *RCS Adv.*, **2017**, 7, 40383-40391 (Copyright © 2017 Royal Society of Chemistry).

process. In this case, the streams of bubbles actually played a role of "dynamic templates" to promote the formation of Ni micro-channels. From Figure 25b, the morphology of V_2O_5 nanostructures can be treated as hierarchical 2D nanosheets. There are two types of the growth of V_2O_5 nanosheets. One is the 2D nanosheets array directly formed on the surface of Ni/Porous-Ni substrate (Figure 26). This growth is highly compact and uniform with the full coverage of the surface of Ni/Porous-Ni substrate. The other is the multilayered peony-like micro-configuration grown from a large amount of 2D nanosheets. In macroscopic view of Figure 26, the annealed Ni/Porous-Ni/V_2O_5 nanocomposite has a physically firm and stable coating layer of V_2O_5 nanostructures.

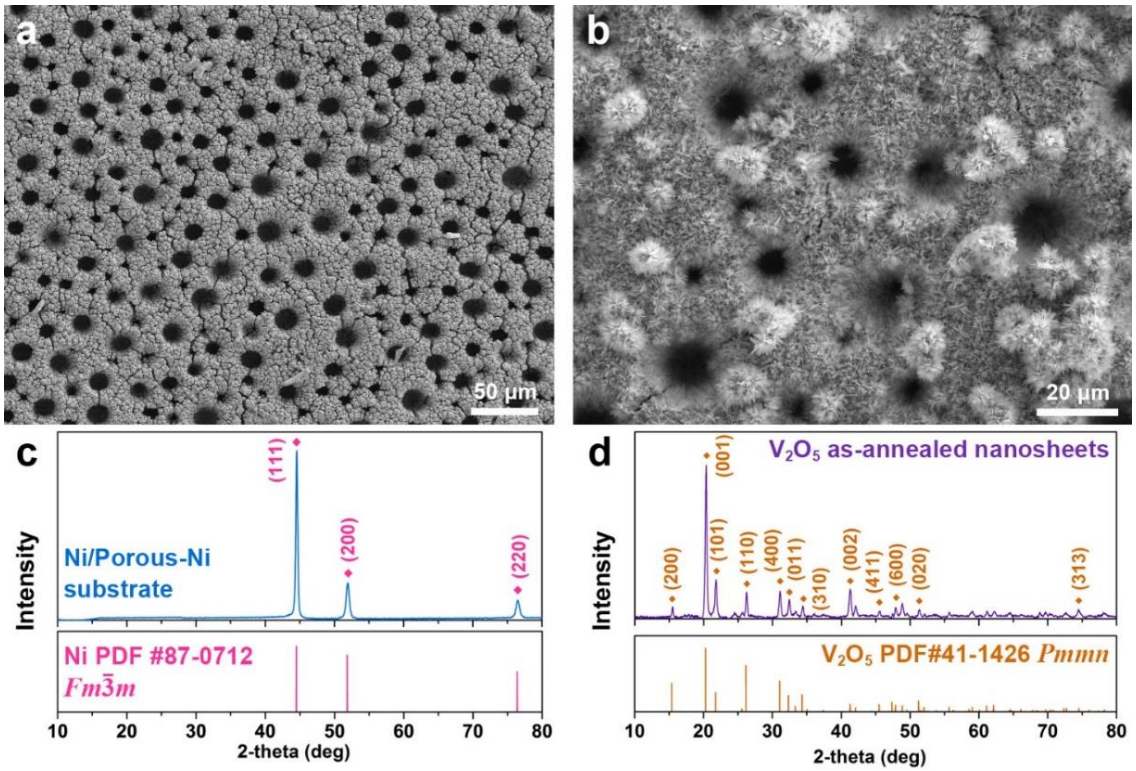

Figure 25. The low-magnified SEM photographs of (a) Ni/Porous-Ni porous substrates (500x) and (b) Ni/Porous-Ni/V_2O_5 nanocomposites (1500x). Corresponding XRD patterns of the (c) Ni/Porous-Ni substrate and (d) as-annealed V_2O_5 powders.

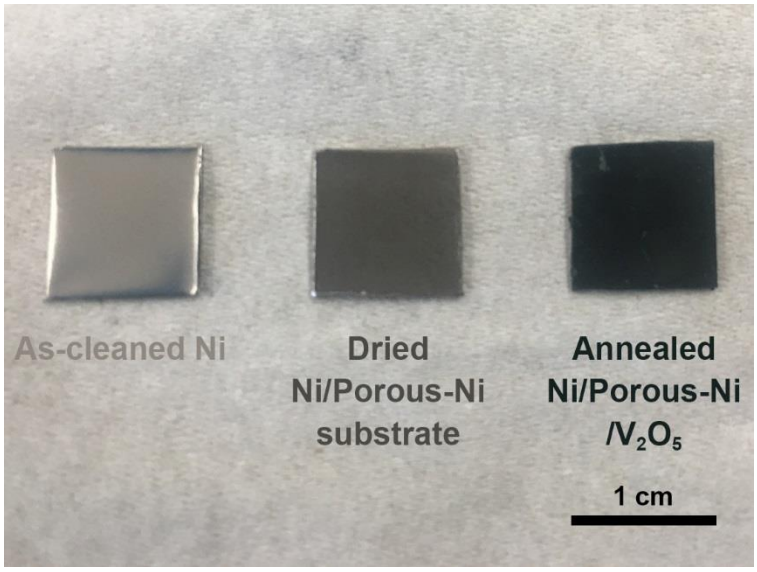

Figure 26. The digital camera photograph of the as-cleaned Ni, dried Ni/Porous-Ni substrate, and Ni/Porous-Ni/V_2O_5 nanocomposites.

Referring to the crystallographic properties of Ni/Porous-Ni/V_2O_5 nanocomposites, two XRD patterns of Ni/Porous-Ni substrate and V_2O_5 as-annealed nanosheets are shown in Figure 25c and d, respectively. The electrodeposited Ni layer with micro-channels has a well-defined face-centered cubic (FCC) structure (JCPDS PDF No. 87-0712, $Fm\bar{3}m$, a = 3.5238 Å). After hydrothermal growth at 200 °C and annealing at 350 °C, the V_2O_5 nanosheets reveal an excellent orthorhombic structure (JCPDS PDF No. 41-1426, *Pmmn*, a = 11.510 Å, b = 3.563 Å, c = 4.369 Å). It is worth noticing in Figure 25d that a dominating peak of the XRD pattern of V_2O_5 nanosheets is from facet (001). This suggests that the most exposed facet of formed V_2O_5 nanosheets is (001). For the comparison, the crystallinity of as-annealed V_2O_5 nanosheets is much better than that of as-hydrothermal V_2O_5 nanomaterial without annealing, whose XRD

pattern is shown in Figure 27. This indicates the significant role played by the annealing process for the synthesis of well-crystalline V_2O_5 nanosheets.

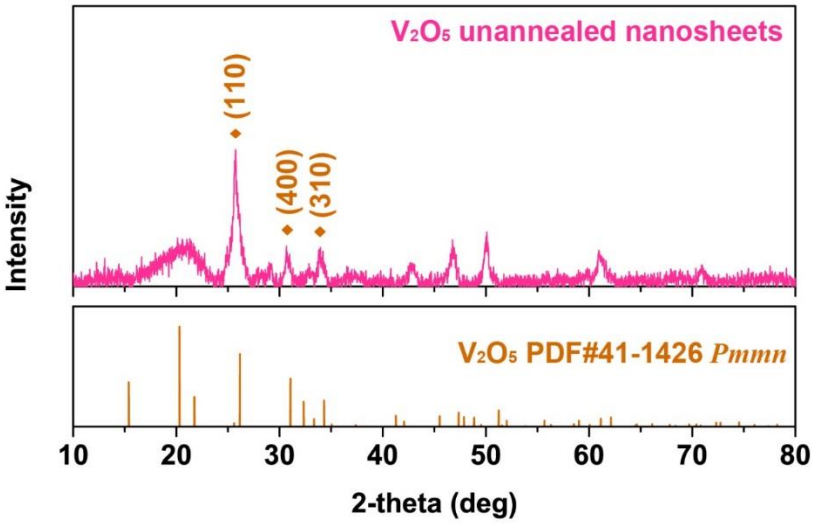

Figure 27. The XRD pattern of the unannealed V_2O_5 dried powders.

Above results showed that the Ni/Porous-Ni/V_2O_5 nanocomposites have exhibited super-hierarchical nanoarchitecture with evenly composited distribution. Figure 28 shows this feature. In Figure 28a, both 2D V_2O_5 nanosheets deposited on Ni surface and the V_2O_5 micro-peonies can be found in a selected region nearby a Ni micro-channel. The uniform and concentrated deposition of 2D V_2O_5 nanosheets array can not only take place on the outer surface of Ni deposit, but the inner wall of micro-channels as well. Meanwhile, multilayered micro-peonies with diameters of 5-10 μm are attached to the nanosheets array. This feature of hierarchical 2D nanostructures directly deposited on the hierarchical micro-sized substrate can be regarded as the "super-hierarchical nanoarchitecture".

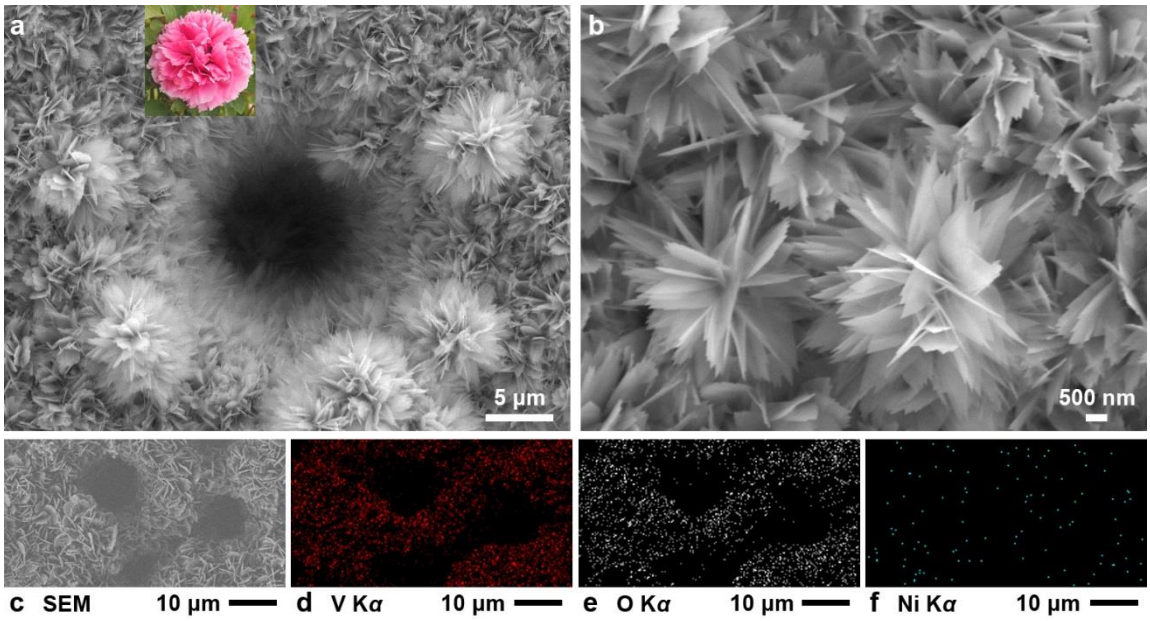

Figure 28. The medium- and high-magnified SEM photographs and EDS mapping spectrum of Ni/Porous-Ni/V_2O_5 nanocomposites. (a) The 5000x SEM image of Ni/Porous-Ni/V_2O_5 nanocomposites at the location of one Ni micro-channel. The inset is a photograph of a real blossoming peony. (b) The 15000x SEM image of several 2D V_2O_5 nanosheets and micro-peonies. (c) The SEM photograph for the region characterized by EDS mapping. The element map of (d) vanadium (Kα), (e) oxygen (Kα), and (f) nickel (Kα).

The morphological details of Ni/Porous-Ni/V_2O_5 at the high magnification are revealed in Figure 28b. The 2D V_2O_5 nanosheets are ultrathin with a thickness lower than 50 nm. The partial translucency of several "nano-petals" of micro-peonies validates this ultrathin feature. The lateral dimensions of single nanosheets are approximately 1-2 μm. Simultaneously, a type of obvious serrated edges can be observed from numerous 2D nanosheets. The slightly different brightness shown in those nanosheets implies a type of stacking of multiple pieces. Usually, this stacking has 3-5 pieces of V_2O_5 nanosheets. Furthermore, the morphological consistency before and after annealing is evaluated through the SEM imaging of an unannealed Ni/Porous-Ni/V_2O_5 sample shown

in Figure 29. Similar morphologies of ultrathin (~50 nm) 2D V_2O_5 nanosheets and micro-peonies can also be observed in the unannealed sample. Whereas, the lateral dimensions of unannealed nanosheets are usually larger (2-4 μm) than those of annealed counterparts. The shrinkage of lateral sizes was the consequence of the crystallization during the annealing procedure.

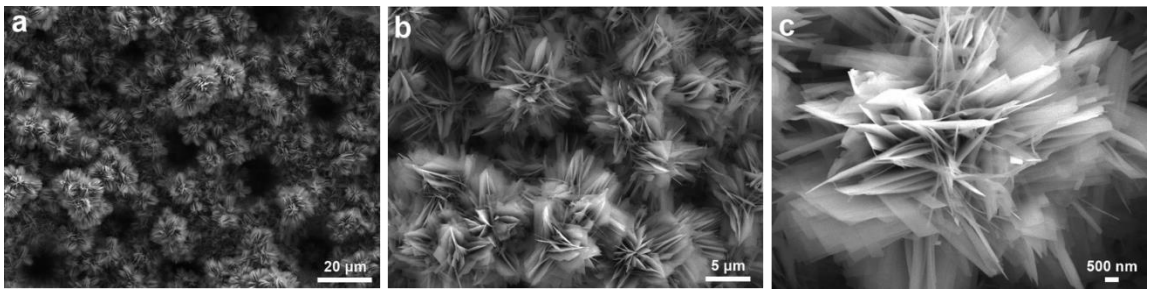

Figure 29. The SEM photographs of unannealed Ni/Porous-Ni/V_2O_5 nanocomposites at various magnifications. (a) 1500x; (b) 5000x; (c) 15000x.

According to the BET nitrogen gas adsorption–desorption experimental results, the BET surface areas of Ni/Porous-Ni/V_2O_5 nanocomposites before and after annealing were 10.2 $m^2\ g^{-1}$ and 15.3 $m^2\ g^{-1}$, respectively. Those values were 40-60 and 6000-7500 times greater than BET surface area of Ni/Porous-Ni substrate ($2.8\times10^{-1}\ m^2\ g^{-1}$) and surface area of as-cleaned Ni sheet ($1.80\times10^{-3}\ m^2\ g^{-1}$). Meanwhile, the volumetric porosity of Ni/Porous-Ni substrate and Ni/Porous-Ni/V_2O_5 nanocomposites before and after annealing were determined as 47.1%, 54.9%, and 55.1%, respectively. These results revealed the ultrahigh specific surface area and enhanced porosity of super-hierarchical Ni/Porous-Ni/V_2O_5 nanocomposites. The hierarchical and multilayered V_2O_5 nanosheets and micro-peonies were the main reason of the increased surface area.

Moreover, the uniformity of the spatial distribution of elements is evidenced through the EDS element mapping. After selecting a random area including a large amount of 2D V_2O_5 nanosheets and several Ni micro-channels (as shown in Figure 28c), the element mapping of vanadium (V, Figure 28d), oxygen (O, Figure 28e), and nickel (Ni, Figure 28f) were obtained. The uniform and abundant distribution of both elements of V (at. % ~27%) and O (at. % ~64%) from Figure 2d and e suggested that the numerous 2D nanosheets observed in Figure 3c were V_2O_5. The rare but even distribution of Ni (at. % ~9%) from Figure 2e confirmed the virtually complete hindering of Ni/Porous-Ni substrate by 2D V_2O_5 nanosheets.

5.2 Growth mechanism of V_2O_5 hierarchical nanostructure

The lamellar 2D morphology of V_2O_5 nanosheets on the Ni/Porous-Ni substrate was the result of directional growth of V_2O_5 nanocrystals. Figure 30 is a general schematic illustration of the formation mechanisms of V_2O_5 nanostructures. For this Ni/Porous-Ni/V_2O_5 nanocomposite, the formation mechanism of ultrathin 2D V_2O_5 nanosheets and micro-peonies is necessary to be investigated. This is quite significant in order to utilize this novel super-hierarchical nanoarchitecture. Through the crystallographic analysis, a set of models was proposed in this research. According to the fundamentals of the crystallography, V_2O_5 possesses a type of complicated orthorhombic phase [138]. As shown in Figure 30a, each vanadium atom (white balls) is embedded by a distorted pyramid composed of four oxygen atoms (red balls). Eight corners of a V_2O_5 unit cell are occupied by vanadium atoms [139]. The connection of adjacent VO_5

pyramids forms a 2D single layer in *a*-*b* plane. The weak bonding along *c* direction results in the layered crystalline structure of V_2O_5 [140]. When considering the direct growth of the 2D V_2O_5 nanosheets on the surface of Ni/Porous-Ni substrate, the most exposed crystalline facets of both V_2O_5 and Ni were analyzed at first. Since the highest XRD peaks of Ni/Porous-Ni substrate and V_2O_5 nanosheets were (111) and (001), two regulations could be summarized based on similar analysis in previous researches [141-143]. 1) The electrodeposited Ni layer had a most-common surface facet of (111); 2) The double sides of the 2D V_2O_5 nanosheets had the Miller index of (001). This suggested that the ultrathin 2D V_2O_5 nanosheets were composed of *c*-directional stacking of a series of planes combined by VO_5 pyramids.

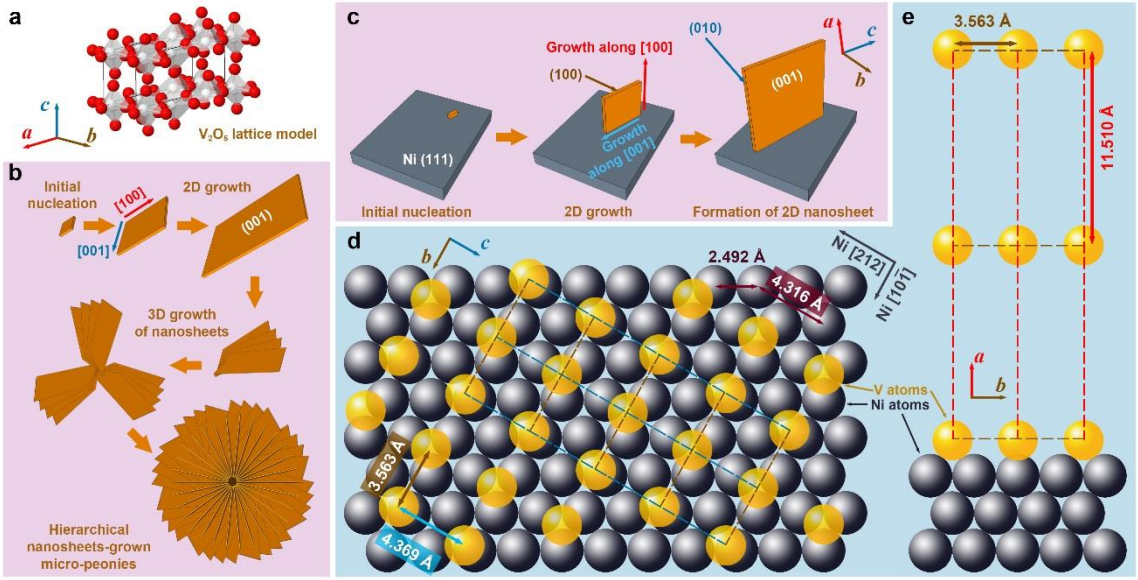

Figure 30. The schematic illustration of the formation mechanism of Ni/Porous-Ni/V_2O_5 nanocomposites. (a) The model of crystalline lattice structure of V_2O_5. The formation procedure of (b) V_2O_5 micro-peonies and (c) 2D V_2O_5 nanosheets on Ni/Porous-Ni substrate. The (d) top view and (e) side view of the atomic structure model of V_2O_5 crystal on the Ni (111) substrate. Note: for the simplification, only the vanadium atoms that are located at the corners of the V_2O_5 unit cell of are depicted in (d) and (e).

The formation of ultrathin V_2O_5 nanosheets was the result of the 2D hydrothermal growth from the $[VO_2]^+$ precursor. This precursor was obtained after mixing V_2O_5 powders and H_2O_2 solution before hydrothermal process. According to the related researches, the reactions between bulk V_2O_5 and H_2O_2 with the participation of H_2O at room temperature are listed below [144-146]:

$$V_2O_5 + 4H_2O_2 \rightarrow 2[VO(O_2)_2(OH_2)]^- + 2H^+ + H_2O \quad (4)$$

$$V_2O_5 + 2H^+ + 4H_2O_2 + 3H_2O \rightarrow 2[VO(O_2)(OH_2)_3]^+ + O_2 \quad (5)$$

$$2[VO(O_2)_2(OH_2)]^- + 4H^+ + 2H_2O \rightarrow 2[VO(O_2)(OH_2)_3]^+ + O_2 \quad (6)$$

$$2[VO(O_2)(OH_2)_3]^+ \rightarrow 2[VO_2]^+ + O_2 + 6H_2O \quad (7)$$

Figure 31. The digital camera photograph of the time-dependent hydrothermal treatment at 200 °C. Different vials from left to right enclose the as-reacted solution/suspension of before hydrothermal, after hydrothermal for 1, 2, 4, and 7 hours.

The ions of $[VO_2]^+$ along with O_2 gas and water molecules are final products of those reactions. That was the reason why the clear and light-orange-colored solution with some bubbles was obtained after stirring, which is shown in Figure 31. During the subsequent hydrothermal treatment, the $[VO_2]^+$ ions acted as the role of vanadium (V^{5+})

source provider. The ultrathin nanosheets of V_2O_5 were gradually formed in the supercritical condition offered by the hydrothermal process [146].

To validate the procedure of 2D hydrothermal growth, the time-dependent SEM imaging of hydrothermal treatment for 1 h, 2 h, 4 h, and 7 h are shown in Figure 32. The gradual formation of the 2D morphology from preliminary nucleation to lamellar micro-peonies during the first 4 hours can be observed through SEM panels of Figure 4a-c. From Figure 32d, 7-hour dense and compact growth of micro-peonies even virtually hinder the Ni micro-channels.

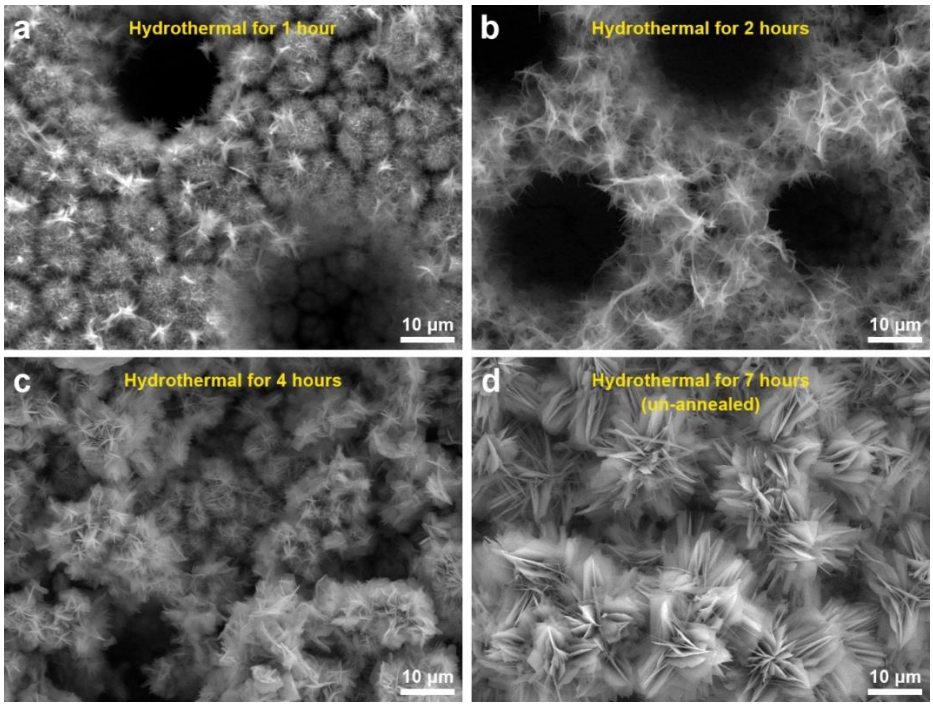

Figure 32. The time-dependent SEM images of hydrothermal treatment at 200 °C for (a) 1 h, (b) 2 h, (c) 4 h, and (d) 7 h (before annealing).

Considering the most exposed facet of (001) of 2D V_2O_5 nanosheets, the formation procedure of them could be described as the 2D growth of V_2O_5 crystals along

[100] and [001] directions after forming initial nucleation. Figure 30b and c depict this process. During the 2D growth of ultrathin V_2O_5 nanosheets, the preference of the smaller total surface energy promoted the approaching of neighboring nanosheets to assemble into multilayered micro-peonies (as illustrated in Figure 30b). The structure of micro-peonies were stable due to the minimization of the total surface energy [147-149]. Furthermore, the process of Ostwald ripening was also one reason of the micro-peony formation [150].

Further study was conducted on the mechanisms of atomic-scale formation of ultrathin 2D V_2O_5 nanosheets directly on the surface of Ni (111) surface. As sketched in Figure 30c, the V_2O_5 nanosheets are grown through a similar manner of 2D growth along [100] and [001] directions in the hydrothermal condition. It is necessary to point out that the facet of V_2O_5 nanosheets interfacing the Ni (111) plane can be determined as (100). This is based on the analysis of the crystalline structures of Ni (111) plane and V_2O_5 unit cells. An atomic structure model illustrated as Figure 30d and e was constructed to illustrate the evolution. One necessary condition to form a crystalline material on the surface of another similar to the epitaxial growth is the small lattice mismatch between two crystals [151-155]. According to the crystallographic data obtained through the XRD peak identification in an aforementioned part of this paper, the FCC Ni (111) facet has the interatomic distance of 2.492 Å. Therefore, the distance between two nearest Ni atoms (grey spheres in Figure 3d and e) along [212] direction is 4.316 Å (as marked in Figure 30d). On the other side, the orthorhombic V_2O_5 (100) facet has the lattice parameters as 3.563 Å (along *b* direction) and 4.369 Å (along *c* direction),

which are also marked in Figure 30d. Thanks to the small lattice mismatch of 1.2% between 4.369 Å and 4.316 Å, the vanadium atoms (yellow spheres in Figure 30d and e) on the facet (100) can be packed on the Ni (111) surface along [212] and $[10\bar{1}]$ directions. Axes of V_2O_5 *b* and *c* are corresponding to the directions of Ni $[10\bar{1}]$ and $[\bar{2}\bar{1}\bar{2}]$, respectively. The form of packing of vanadium atoms at the corner of the orthorhombic V_2O_5 lattice is demonstrated as Figure 30d and e. Through this packing the most exposed facet of the V_2O_5 nanosheets is (001). This is consistent with the experimental measurement using XRD. As noted that the oxide of V_2O_5 directly grew on the metallic Ni surface and the ions of O^{-2} acted as the natural binder. It is anticipated that there is no clear interface formed.

5.3 Improved heat dissipation

Heat dissipation of the super-hierarchical Ni/Porous-Ni/V_2O_5 nanocomposite was characterized using an *in situ* heating and cooling process. For comparison, seven samples were tests. They are as-cleaned Ni, Ni/Porous-Ni substrate, Ni/Porous-Ni/V_2O_5 after 1 hour, 2 hours, 4 hours, and 7 hours (annealed and unannealed) hydrothermal treatments at 200 °C. After placing seven samples at the center of a hot plate as illustrated in Figure 33, a slow and uniform heating was started at room temperature of 27 °C (300 K). The surface temperature of the hot plate reached 49.3 °C after 25 mins of heating. The power was then turned off and the plate was cooled in air. For another 25 mins, surface temperature of the hot plate reached 32 °C.

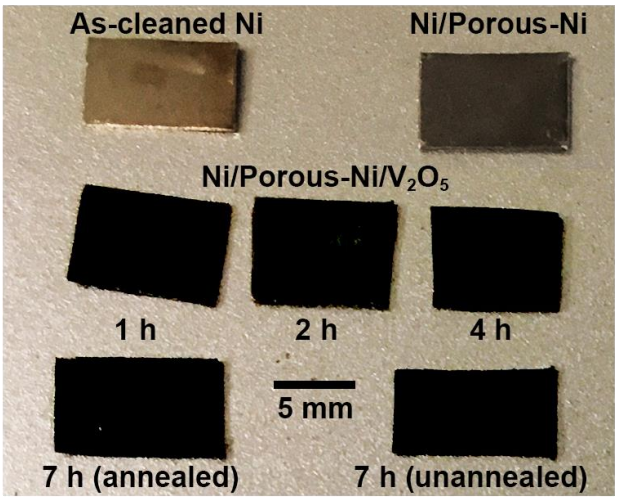

Figure 33. The digital camera photograph of the samples of as-cleaned Ni, Ni/Porous-Ni substrate, Ni/Porous-Ni/V_2O_5 nanocomposites after hydrothermal treatment for 1 h, 2 h, 4 h, 7 h (both before and after annealing). This layout is for the heat dissipation measurement.

All panels in Figure 34 illustrate the *in situ* time-dependent infrared thermal images of the samples. It was clear to observe that the surface temperature *T* of Ni/Porous-Ni/V_2O_5 after 7 hours hydrothermal treatment with annealing was the highest, meaning the highest thermal conductivity. Meanwhile, the surface temperature of as-cleaned Ni was the lowest, the least conductive. This was evidenced in both heating and cooling cycle. The detailed data points of the surface temperatures of 7 samples and hot plate are depicted in Figure 35. The trend of $T_{7h\text{-}an} > T_{7h\text{-}un} > T_{4h} > T_{2h} > T_{1h} > T_{Ni/Porous\text{-}Ni} > T_{Ni}$ was discovered that can be seen at any time point during the heating-cooling cycle. The higher the surface temperature, the greater the dissipated heat flow [156, 157], the values of *Q* followed the rule of $Q_{7h\text{-}an} > Q_{7h\text{-}un} > Q_{4h} > Q_{2h} > Q_{1h} > Q_{Ni/Porous\text{-}Ni} > Q_{Ni}$.

In this research, the regulation of Fourier's law for the heat conduction was applied to investigate the heat dissipation performance. Equation (8) describes the formula of Fourier's law [40].

$$Q = qA = -kA\frac{\mathrm{d}T}{\mathrm{d}x} \tag{8}$$

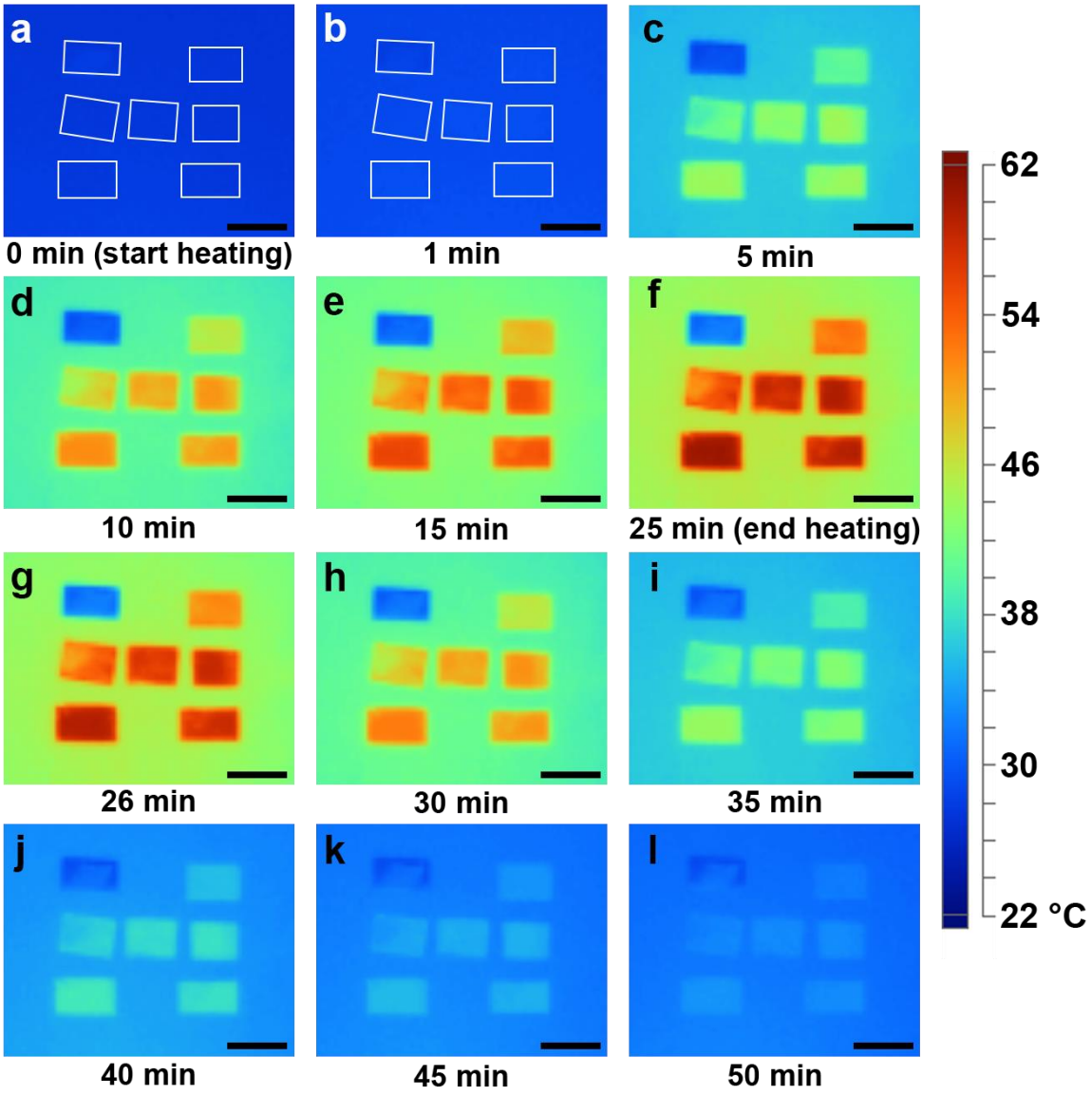

Figure 34. The time-dependent infrared thermal images of samples during an *in-situ* heating (a)-(f) and cooling procedure (g)-(l). The heating and cooling durations are 25 min. The scale bars are 1 cm. The white rectangles in (a) and (b) mark the locations of 7 samples.

Parameters of q, A, and k are heat flux density, surface area, and thermal conductivity of the sample. $\mathrm{d}T/\mathrm{d}x$ is the gradient of the temperature from one side of

sample to the other. In the present work, dT/dx can be rewritten as $(T_{plate} - T_{room})/d$ as the temperature gradient is linear, where d is the thickness of all samples, i.e. ~0.13 mm. Hence, at a specific time point during heating and cooling, values of $(T_{plate} - T_{room})/d$ as well as dT/dx of all seven samples were nearly identical. According to reported data, the thermal conductivity of V_2O_5 thin nanosheets ranged 0.45–1.7 W m^{-1} K^{-1} [158, 159]. Although the thermal conductivity of 200 Ni was 70 W m^{-1} K^{-1} [40], the value of product of $(kA)_{7h\text{-}an}$ was still approximately 150 times higher than $(kA)_{Ni}$. The main reason was the ultrahigh specific surface area of the super-hierarchical Ni/Porous-Ni/V_2O_5 nanocomposite. The ultrahigh surface area was far enough to compensate the intrinsic low thermal conductivity of V_2O_5 thin nanosheets. As a result, $Q_{7h\text{-}an}$ was the greatest among all 7 samples at any moment during the heating and cooling. As a result, the super-hierarchical Ni/Porous-Ni/V_2O_5 nanocomposite exhibited superior heat dissipation efficiency. This unprecedented characteristic indicates the potential to be used as novel surface coatings to improve cooling effect for macro- and micro-devices.

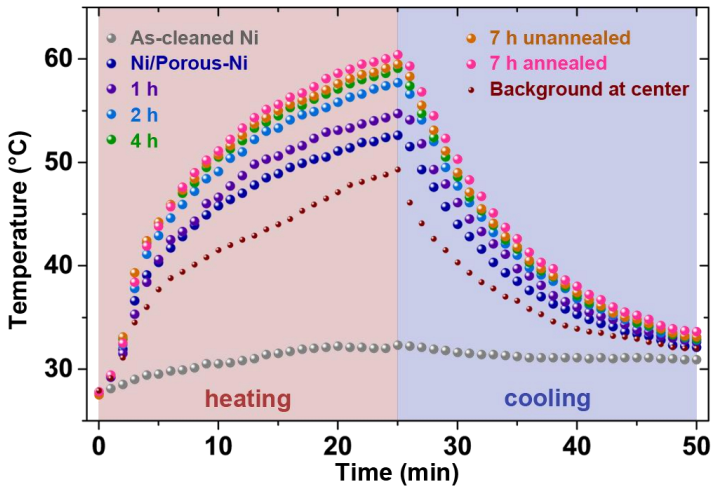

Figure 35. The plot of the temperature change of all samples and the central point of background during the heating and cooling procedure.

5.4 Summary

In this chapter, a super-hierarchical Ni/Porous-Ni/V_2O_5 nanocomposite was fabricated using a simple, low-cost, and environmentally-friendly two-step approach of electrodeposition followed by hydrothermal treatment. A nickel substrate was electrodeposited with vertically-aligned micro-channels of ~10 μm in diameter through hydrogen bubbles as "dynamic templates". Two distinguished nanostructures were generated, 2D V_2O_5 nanosheets (< 50 nm thick) and peony-like micro-configuration. These two structures were evolved directly on the Ni/Porous-Ni substrate surface using a hydrothermal and annealing process. Through the BET nitrogen adsorption-desorption experiment, the specific surface area and porosity of the annealed Ni/Porous-Ni/V_2O_5 nanocomposite was determined as 15.3 $m^2\ g^{-1}$ and 55.1%. The growth mechanism of such hierarchical morphology of V_2O_5 nanostructures was investigated. Firstly, XRD analysis indicated that 2D crystal grew along the directions of [100] and [001] from the $[VO_2]^+$ precursor. Furthermore, micro-peonies were the result of the growth and Ostwald ripening inside the supercritical fluid. An atomic crystalline model was generated to illustrate the interfacial relationship, the low lattice mismatch (1.2%) between directions of FCC Ni [212] and orthorhombic V_2O_5 [001] promoted the packing of vanadium atoms of facet (100) on the Ni (111) surface. Furthermore, the superior heat dissipation performance of super-hierarchical Ni/Porous-Ni/V_2O_5 sample was discovered through *in situ* thermal imaging. This unique characteristic was attributed to the ultrahigh surface area. The great thermal energy released through the Ni/Porous-Ni/V_2O_5 sample was

beneficial to applications in effective cooling when the material is made as coatings. Overall, the easy fabrication, unique super-hierarchical structures, and ultrahigh surface area open new avenues for future investigation. The advanced structure generated in this research will facilitate the usage of Ni/Porous-Ni/V_2O_5 composites for the application of surface coating to prevent the overheating of macro- and micro-devices.

CHAPTER VI

LITHIUM-ION ELECTRODE OF ANATASE-BASED NANOCOMPOSITE*

This chapter investigates the electrochemical performance of a hierarchical nanostructured Cu/Ni/TiO_2 composite as an anode for LIBs. This composite consisted anatase TiO_2 active material and metallic current collector of an anode. The Cu/Ni/TiO_2 composite exhibited excellent electrochemical performance and stable reliability of the rate performance and the lifespan under ultrahigh speed of charging-discharging.

6.1 Crystallographic and morphological characteristics of Cu/Ni/TiO_2

In this section, the physical features referring to crystallography and morphology of Cu/Ni/TiO_2 composites were characterized. The physical characterizations of as-synthesized TiO_2 and Cu/Ni samples using XRD and SEM are shown in Figure 36. From the comparison of high peaks between Figure 36a and b, the as-synthesized TiO_2 NPs after annealing had the crystalline structure of anatase phase (JCPDS No. 73-1764). A tetragonal unit cell (space group of $I4_1/amd$) with the lattice parameters of a = 3.776 Å and c = 9.486 Å represented this structure. Facets of (101) and (200) were its major dominated peaks. This shows that the as-annealed TiO_2 NPs are mainly consisted of anatase. The exhibition of Figure 36c-e revealed the FCC structure owned by both Ni

*Part of this chapter reproduced with permission from "Hierarchical Structured Cu/Ni/TiO_2 Nanocomposites as Electrodes for Lithium-ion Batteries" by Yuan Yue, *et al.*, *ACS Appl. Mater. Interfaces*, **2017**, 9, 28695-28703 (Copyright © 2017 American Chemical Society).

electrodeposited layer and Cu substrate. No oxidation states of Ni or Cu were found through the XRD patterns. The narrow and sharp peaks shown in Figure 36a and c suggested the well-crystalline structures of both TiO_2 and Cu/Ni samples.

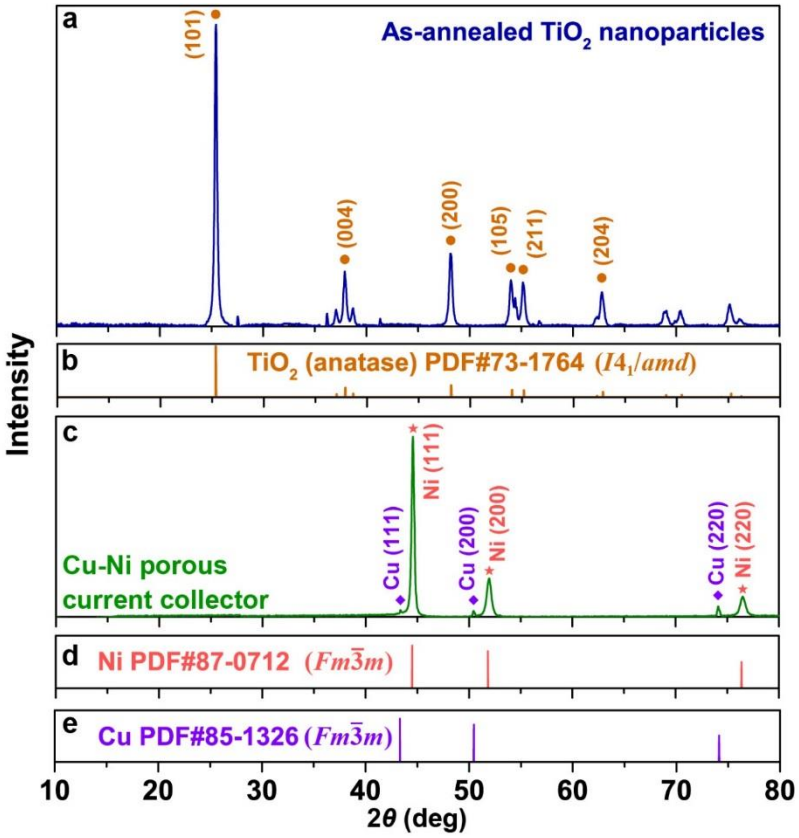

Figure 36. The crystalline characterization of as-annealed TiO_2 NPs and Cu/Ni current collectors. (a) The XRD pattern of the as-synthesized TiO_2 sample. (b) The standard XRD peaks of JCPDS No. 73-1764 of anatase phase of TiO_2. (c) The XRD pattern of the Cu/Ni sample. The JCPDS standard XRD peaks of (d) No. 87-0712 of Ni and (e) No. 85-1326 of Cu.

The morphological characterizations for both TiO_2 and Cu/Ni samples were conducted through the imaging of SEM. Figure 37a demonstrates the morphology of as-synthesized anatase TiO_2 NPs. The size of those anatase TiO_2 NPs was 97.1 ± 15.2 nm with a stable monodispersion (as shown in Figure 37b). Such a uniform morphology in the nanoscale ensured the reliability to be used as anode materials of LIBs. The wet-

chemical hydrolysis of Ti(IV) isopropoxide dissolved in ethanol solution at the elevated temperature could obtain the product of Ti(IV) hydroxide ($Ti(OH)_4$) colloidal suspension [160]. The sufficient stirring and the addition of CTAB as a surfactant facilitated the formation of uniformly distributed nanosized $Ti(OH)_4$ particles. During the annealing procedure, the hydroxide group broke into oxygen ion with the release of water molecules. The anatase NPs was obtained if the annealing temperature was fixed at 600 °C [20].

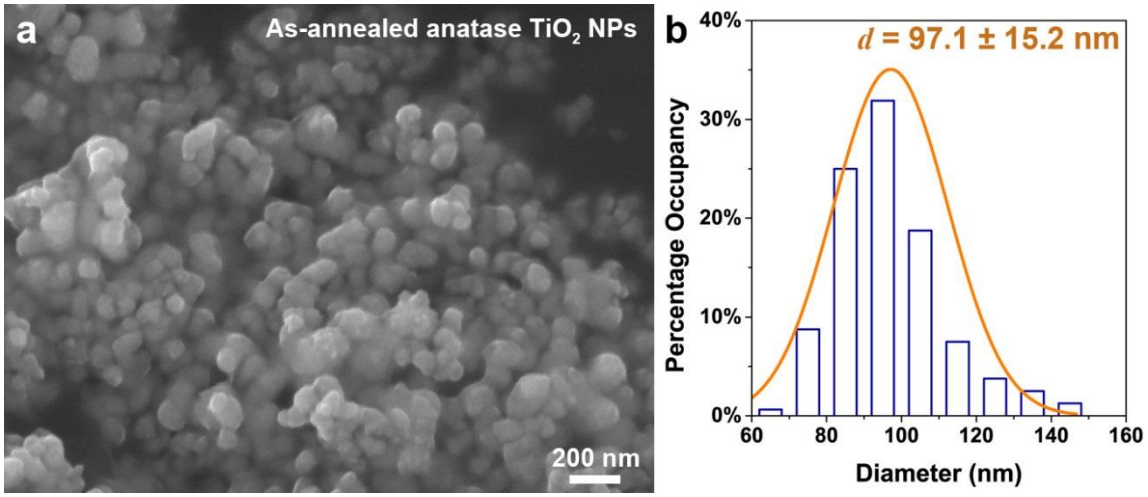

Figure 37. The morphological characterization of as-annealed TiO_2 NPs. (a) The SEM photograph of anatase TiO_2 NPs. (b) The statistical size distribution of anatase TiO_2 NPs.

The electrodeposited Ni layer on the surface of Cu substrate had the morphology of highly porous structure with vertically-aligned micro-channels. Figure 38a-f illustrate the top view SEM photographs of all six sets of Cu/Ni current collectors from A to F. From Figure 38a, set Cu/Ni-A with 0.1 M NH_4^+ completely had no distinguishable pores. With the increasing of the addition of NH_4^+, as shown in Figure 38b-f, an increasing amount of pores could form on the surface of Cu substrate. The morphology

of vertically-aligned micro-channels was revealed through the cross-sectional SEM imaging shown in Figure 39. The boundary of every single completely or partially visible vertical micro-channel in Figure 39 was marked by the yellow dashed line. It was also clear that additional NH_4^+ could result in the increasingly hierarchical architecture. Therefore, the highly porous and hierarchical vertically-aligned micro-channeled morphology of Cu/Ni samples was convincingly validated. Such morphology was the result of the selective growth of Ni with the assistance of the hydrogen bubbles stream during the electrodeposition [137].

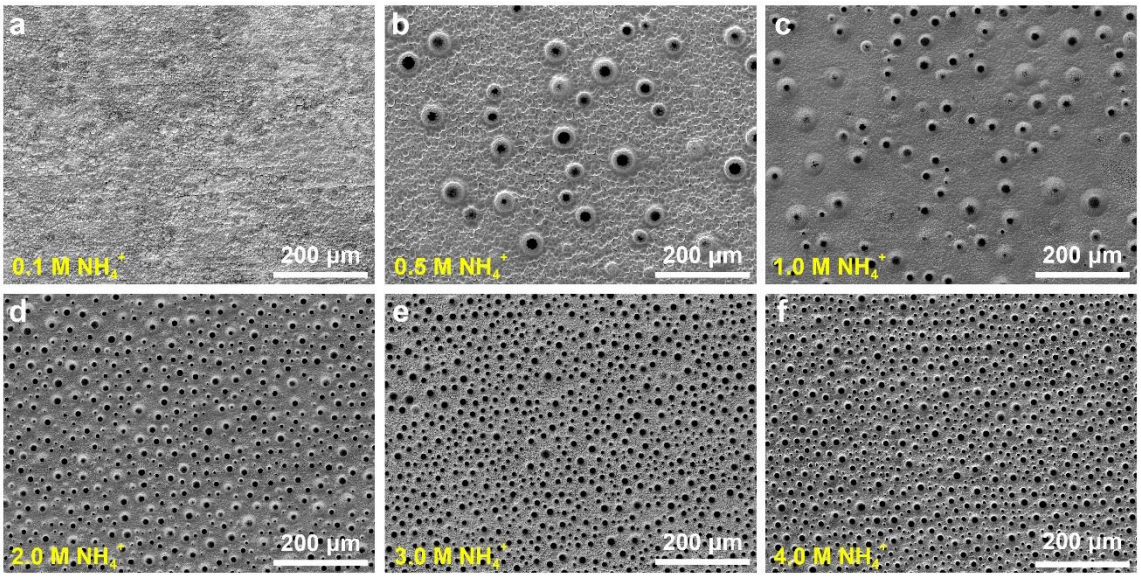

Figure 38. The morphological properties of six sets of Cu/Ni porous current collectors. The top view SEM photographs of Cu/Ni current collector of (a) set Cu/Ni-A, (b) set Cu/Ni-B, (c) set Cu/Ni-C, (d) set Cu/Ni-D, (e) set Cu/Ni-E, and (f) set Cu/Ni-F.

Some quantitative statistical analysis of those micro-channels are plotted in Figures 40 and 41. From Figure 41a, the regulation of that the higher concentration of NH_4^+ addition brought smaller diameters with narrower distribution could be found. Higher concentration of NH_4^+ increased the formation rate of small hydrogen bubbles.

This led to the formation of smaller micro-channels. Most of the micro-channels had diameters of approximately 10 μm for sets of D, E, and F. Those three sets also had enhanced number densities of micro-channels and their porosities, which are shown in Figure 41b. For the most favorable set of Cu/Ni-F, which had ~617 micro-channels per 0.5×0.5 mm^2 with the porosity of 32.5%, the specific surface area was suggested to be the greatest. This property was preferred to for the anode of LIBs.

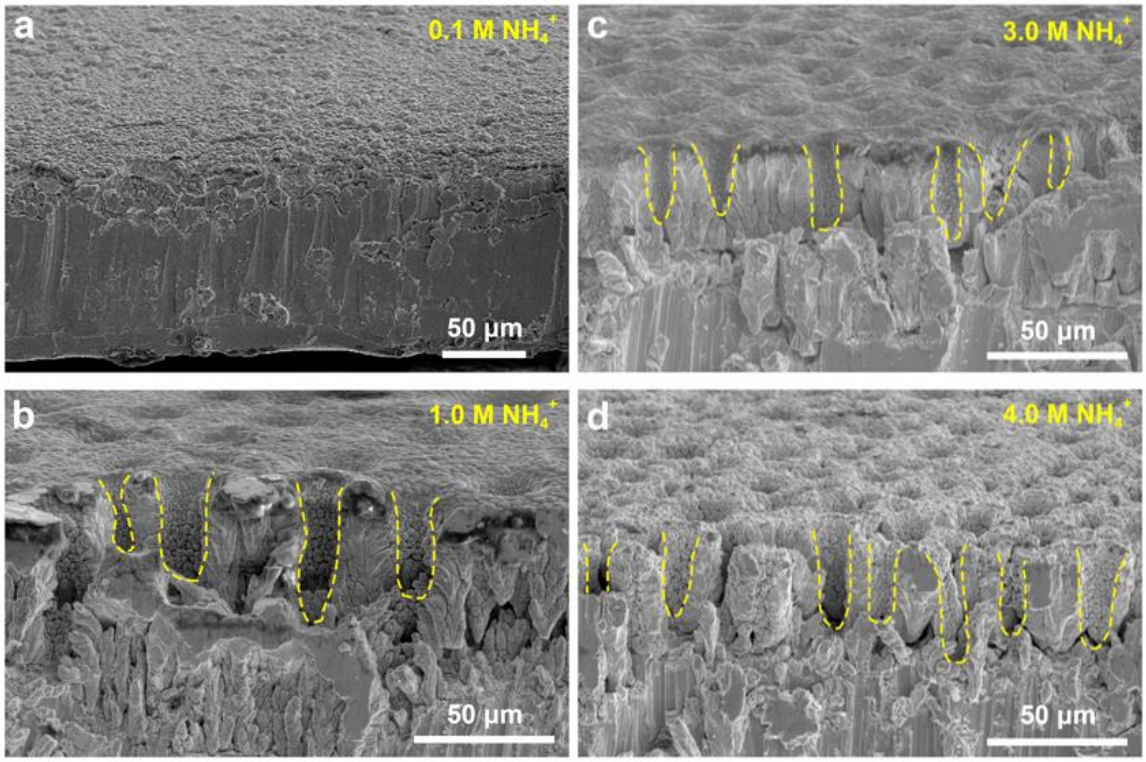

Figure 39. The schematic sketch of several 0.5×0.5 mm^2 Cu/Ni porous composites with different concentrations of NH4+. (a) 0.1 M. (b) 1.0 M. (c) 3.0 M. (d) 4.0 M.

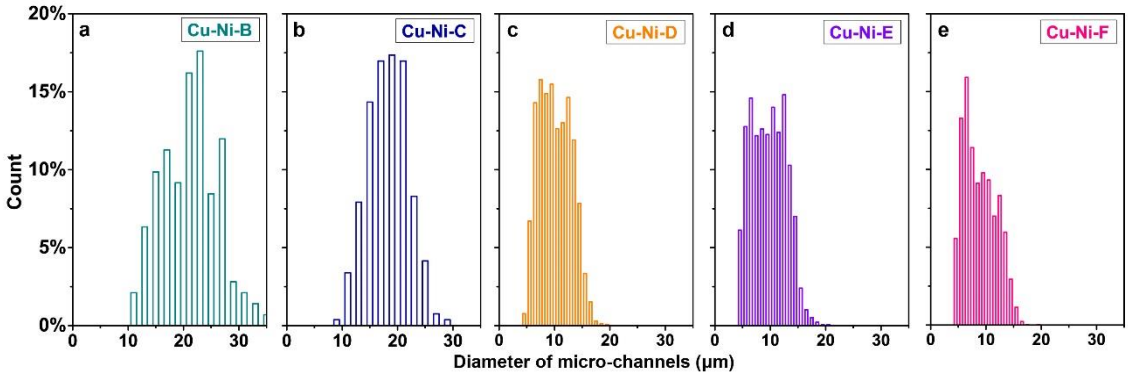

Figure 40. The statistical result of pore diameter distribution of Cu/Ni current collectors. (a)-(e) The statistical histograms of diameter of pores from Cu/Ni-B to Cu/Ni-F.

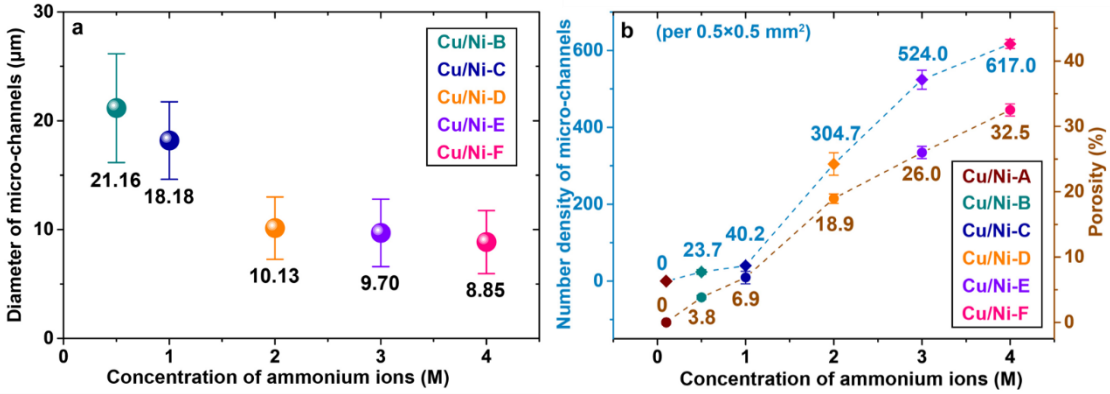

Figure 41. (a) The statistics of diameters of micro-channels among Cu/Ni-B, C, D, E, and F. (b) The plot of number density of micro-channels and porosity of Cu/Ni-B, C, D, E, and F.

6.2 Superior electrochemical performance of Cu/Ni/TiO_2 anode

The electrochemical performance of all six sets of Cu/Ni/TiO_2 and one flat Cu/TiO_2 anode was firstly characterized through the charge-discharge cyclic experiments at a low current density of 0.1 C. The casted TiO_2 active-nanoparticles on each of seven samples had a loading mass of 2.0–2.5 mg on a 1 × 1 cm^2 current collector. Figure 42a and b illustrate the discharge specific capacity plot and Coulombic efficiency plot, respectively. In general, both discharge specific capacities and

Coulombic efficiencies had the identical tendency that better performance was obtained if the number density of micro-channels increased. The initial discharge capacities from Cu/Ni-A to Cu/Ni-F were 100.5, 123.8, 153.4, 220.3, 256.9, and 279.9 mAh/g, respectively. It is obvious from Figure 42a that Cu/Ni-F has the flattest fading curve of capacity and its maximum discharge specific capacity (283.3 mAh/g) occurs at the fifth cycle rather than the first one. After 30 cycles at 0.1 C, the discharge capacity retention from A to F were 54.1%, 75.2%, 78.0%, 44.1%, 65.1%, and 95.0%, which was corresponding to the capacity fading per cycle as 1.53%, 0.83%, 0.73%, 1.86%, 1.17%, and 0.17%, respectively. All of above data for each set of samples is tabulated in Table 4.

Table 4. The symbols of the samples before and after calcining

Sample Name	Max. discharge specific capacity (mAh/g)	Capacity retention after 30 cycles (%)	Coulombic efficiency after 30 cycles (%)
Flat Cu	91.2	43.9	97.2
Cu/Ni-A	100.5	54.1	98.6
Cu/Ni-B	123.8	75.2	98.9
Cu/Ni-C	153.4	78.0	99.1
Cu/Ni-D	220.3	44.1	98.5
Cu/Ni-E	256.9	65.1	99.0
Cu/Ni-F	283.3	93.9	99.9

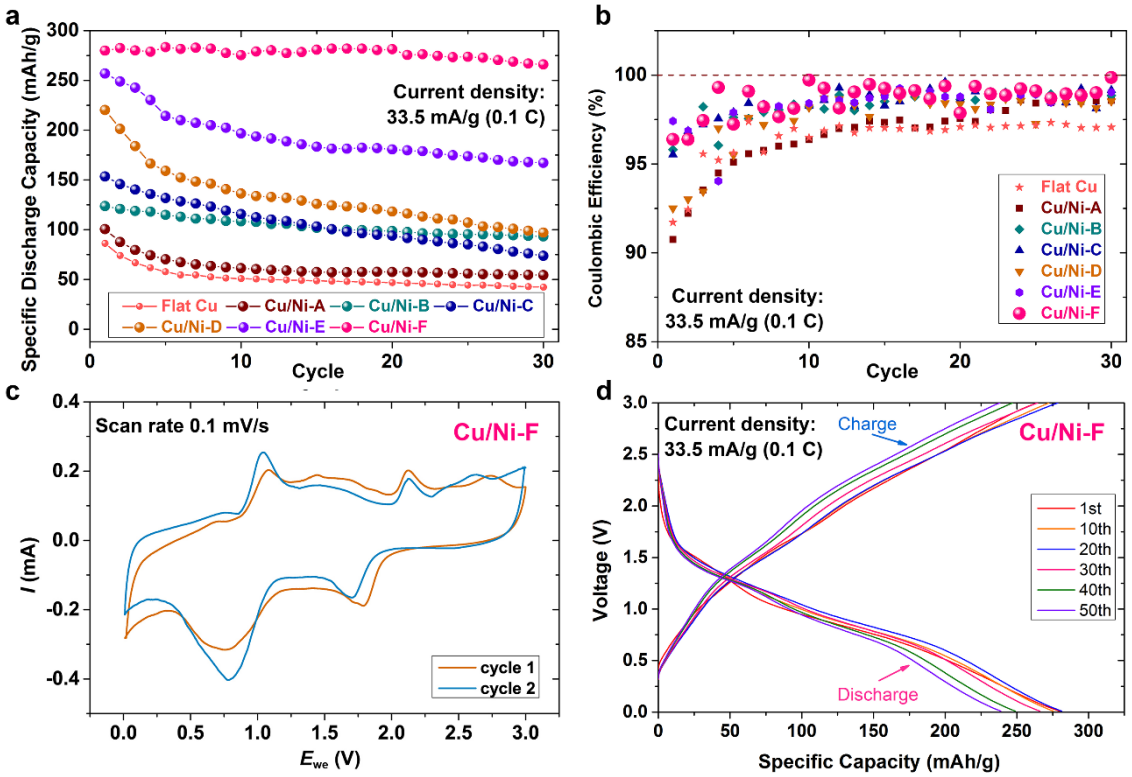

Figure 42. The electrochemical performance of flat Cu/ TiO_2 anode and six sets of Cu/Ni/TiO_2 anodes. (a) The capacity performance of all seven sets of samples with 30 cycles at 33.5 mA/g (0.1 C). (b) The plot of Coulombic efficiency of all seven sets of samples with 30 cycles at 33.5 mA/g (0.1 C). (c) The CV profile of the first and second cycles of Cu/Ni-F sample at a scan rate of 0.1 mV/s within the potential interval of 0.01–3 V (vs. Li+/Li). (d) The charge-discharge profile of Cu/Ni-F sample at the current density of 33.5 mA/g (0.1 C).

As for the values of Coulombic efficiencies, Figure 42b exhibits that the initial Coulombic efficiencies of six samples spans from ~91% to ~97%. After 30 cycles at 0.1 C, all of them could reach values within the range of 98–100%, which implied the stable charge-discharge performance. This could be attributed to the formation of stable solid electrolyte interphase (SEI) [161, 162]. For six samples of Cu/Ni/TiO_2 anodes, a tendency was found that more micro-channels resulted in higher surface area, more loading of TiO_2 NPs, and greater specific capacity. Furthermore, the slightly greater

electrochemical performance of Cu/Ni-A than that of flat Cu anode is observed in Figure 42a and b. This suggested the flat Ni current collector in Cu/Ni-A had similar effect with flat Cu as conventional current collectors.

The set of Cu/Ni-F possessed the most favorable electrochemical performance among all six sets of sample based on the results depicted in Figure 42a and b. More electrochemical tests referred to Cu/Ni-F were conducted to analyze the electrochemical reactions at the anode-electrolyte interface. The CV profile of Cu/Ni-F for the first two cycles is illustrated by Figure 42c. In this research, the potential window was set as 0.01–3 V vs. Li^+/Li, which was different with the conventional setting that started from at least 1.0 V for the anatase TiO_2 anodes [163-170]. From the curves shape in Figure 42c, a pair of oxidation/reduction peaks located at ~1.8 V and ~2.1 V could be obviously found from the discharging and charging curves, respectively. This was consistent with several reported results referring to the anatase TiO_2 anodes [165, 168-170]. This CV profile confirmed that the electrochemically active material in this Cu/Ni/TiO_2 anode was TiO_2 nanoparticles. Neither Ni deposited layer nor Cu substrate participated in the electrochemical reaction. This was actually corresponding to the electrochemical reaction between lithium ions and anatase TiO_2 NPs. The reaction formula could be written as Equation (9) [163].

$$x\mathrm{Li}^+ + \mathrm{TiO}_2 + xe^- \leftrightarrow \mathrm{Li}_x\mathrm{TiO}_2 \quad (9)$$

The value of insertion coefficient *x* usually had the theoretical value of ~0.5, which was equivalent with the theoretical specific capacity of anatase TiO_2 anodes (167.5 mAh/g) [163, 164, 166]. However, the maximum value of *x* was measured as

~0.85 (283.3/335.0) for the best Cu/Ni-F sample in the present research. This suggested that more lithium ions could participated into the electrochemical reaction with respect to anatase TiO_2 anodes, which brought the improvement of *x* value as well as one extra pair of reversible peaks at ~0.8 V (oxidation) and ~1.1 V (reduction). After expanding the potential window, this extra reversible electrochemical reaction kinetics was significant for the excellent electrochemical performance of Cu/Ni-F sample. The stability of such sufficient reaction could be revealed from the charge-discharge profile curves depicted as Figure 42d. The sample of Cu/Ni-F had a series of charge-discharge curves with similar layout at 1st, 10th, 20th, 30th, 40th, and 50th cycles with the C-rate of 0.1 C. This implied the stable peak location of the oxidation/reduction reactions. The corresponding discharge/charge specific capacities at 1st, 10th, 20th, 30th, 40th, and 50th cycles were 279.9/269.8, 275.4/274.6, 281.3/275.3, 266.0/265.7, 248.8/248.0, and 238.7/236.5 mAh/g. Coulombic efficiencies of 96.4%, 99.7%, 97.9%, 99.9%, 99.7%, 99.1% were also evidences of the stable reaction kinetics during the cycling process.

From the electrochemical performance reported in Figure 42, it could be concluded that the sample with the largest amount of micro-channels, i.e. Cu/Ni-F, had the best performance among all six samples. Therefore, more electrochemical tests were conducted for this sample to comprehensively characterize its performance. The related results are exhibited in Figure 43. Firstly, the comparison of the capacity performance between the best (Cu/Ni-F) and the worst (Cu/Ni-A) Cu/Ni/TiO_2 sample is depicted as Figure 43a. After cycling for 100 cycles at 0.1 C, despite both of A and F had virtually 100% Coulombic efficiency (shown in the inset of Figure 43a), their specific discharge

capacity had a wide gap between one another. The initial capacity of F (279.9 mAh/g) was nearly 3 times as that of A (100.5 mAh/g). This could be attributed to the enhanced specific surface area of sample F. According to our recent study (to be published elsewhere), the calculated specific surface area of F was ~3.14 time as that of A. This dramatically improved surface area could provide much more available sites for the electron transport from the anatase TiO_2 NPs to the Cu/Ni porous current collector [79, 171]. Meanwhile, the capacity retention of sample F (75.8%) was much greater than that of sample A (37.5%) after 100 cycles.

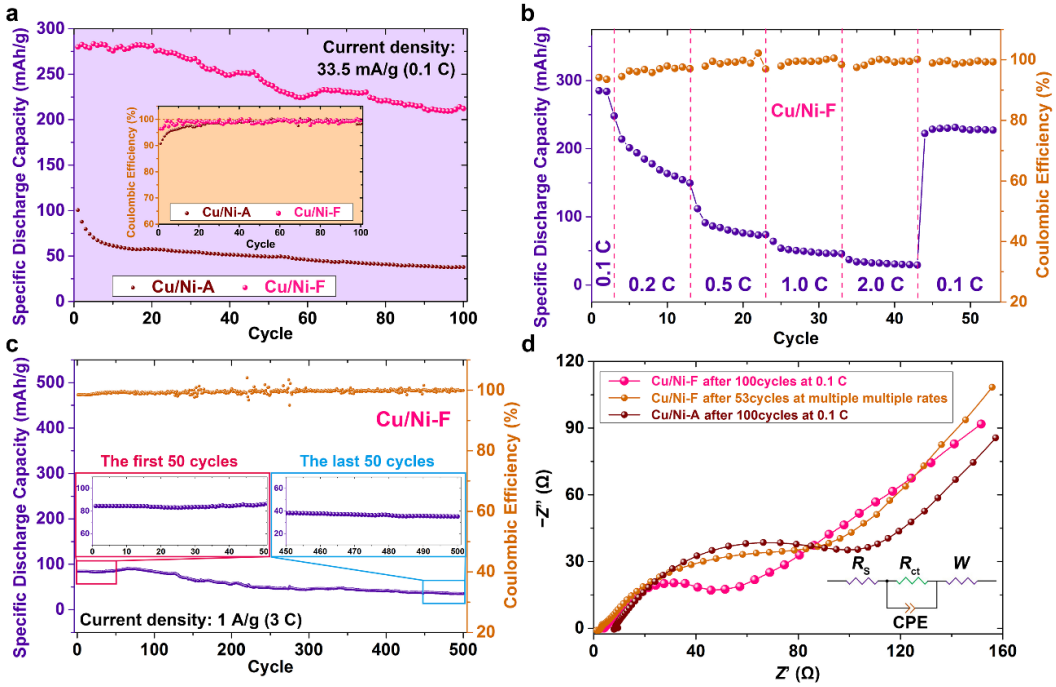

Figure 43. The electrochemical performances of the Cu/Ni-F anode. (a) The comparison of the capacity performance between Cu/Ni-A and Cu/Ni-F anodes for 100 cycles at 0.1 C. (b) The plot of rate capacities of the Cu/Ni-F anode. (c) The capacity performance of the Cu/Ni-F anode at ultrafast-speed (3.0 C) charge-discharge mode with 500 cycles. (d) The Nyquist plot of the EIS test referred to Cu/Ni-F anode.

As a matter of fact, the capacity performance of the Cu/Ni-A sample was equivalent with the conventional electrode using flat Cu current collector. The flat

surface of Cu/Ni-A from Figure 38a resulted in the identical layout of mixed slurry as the flat Cu anode after casting. Such profound electrochemical performance of the Cu/Ni-F sample was the consequence of its unique morphology with highly hierarchical and porous architecture, which was beneficial to form the stable SEI layer and maintain the capacity [172].

The rate performance of the Cu/Ni-F anode under cycling with various current densities is shown as Figure 43b. After accomplishing the first three cycles at a low C-rate of 0.1 C with an initial discharge specific capacity of 285.2 mAh/g, the Cu/Ni-F anode delivered discharge capacities of 149.6, 73.8, 45.8, and 29.3 mAh/g after 13th, 23rd, 33rd, and 43rd cycles, which were corresponding to current densities of 0.2 C, 0.5 C, 1.0 C, and 2.0 C. The discharge capacity recovered to 228.5 mAh/g after returning the current density to 0.1 C. This value was still 80.1% of the initial value in this rate test. This result illustrated the favorable rate performance owned by the Cu/Ni-F anode. The cyclic tests under extreme condition of ultrafast C-rate for numerous cycles is significant for the practical usage of a battery cell. In this case, an ultrafast 3.0 C cyclic tests for the Cu/Ni-F anode was accomplished after three warm-up cycles at 0.1 C. The plots of both discharge specific capacity and Coulombic efficiency are shown in Figure 43c. The capacity was retained as 35.2 mAh/g after 500 cycles at 3.0 C, which was 41.7% of the initial capacity of 84.5 mAh/g. This performance suggested that the mean value of capacity fading was only ~0.1% per cycle under such a fast speed of charging and discharging. Two magnified insets in Figure 43c show the localized capacity plot within first and last 50 cycles. The virtually flat layout of both insets suggested the stable

capacity performance as well. Meanwhile, the Coulombic efficiency among the whole stage of 500 cycles was maintained nearby the reference line of 100%. In brief, the excellent performance of Cu/Ni-F anode was firmly and comprehensively obtained based on results from charge-discharge tests under slow and fast C-rates as well as the multiple-rate test.

6.3 Analysis of the electrochemical kinetics and performance

The favorable electrochemical performance of Cu/Ni-F anode could be ascribed to two aspects at the anode-electrolyte interface. One was the stable formation of SEI layer and the other was the small thickness of formed SEI. The former one had been demonstrated in the aforementioned analysis in this paper, the latter one was evidenced by the Nyquist plot of EIS test. Figure 43d illustrates the comparison of Nyquist curves of Cu/Ni-A and F anodes after cycling with various conditions. It is obvious to find that Cu/Ni-F anode has smaller semicircle arc than that of Cu/Ni-A after 100 cycles at 0.1 C. For Cu/Ni-F anode, the size of semicircle arc after 100 cycles at 0.1 C is smaller than that after 53 cycles of the rate test. According to a typical model of the electrochemical equivalent circuit [173-175] sketched as an inset of Figure 43d, the positive gradient straight line at low frequency region was the symbol of the lithium ion diffusion through the surface layer of anodes [176]. The depressed semicircle in high frequency range was corresponding to the charge transfer resistance [177]. Therefore, values of electrolyte resistance R_s and charge transfer resistance R_{ct} could be calculated. The values of R_s for Cu/Ni-A after 100 cycles, Cu/Ni-F after 100 cycles, and Cu/Ni-F after 53 cycles were

4.2, 3.6, and 3.8 Ω. This suggested the stable condition provided by the liquid electrolyte. On the other hand, their values of R_{ct} had significant differences. After cycling 100 times at 0.1 C, the Cu/Ni-A anode had an R_{ct} value as 74.1 Ω while the Cu/Ni-F had a counterpart of 46.9 Ω. This concluded that the excellent electrochemical performance of Cu/Ni-F anode could be attributed to the enhancement of the charger transfer conductivity during the electrochemical reaction. Furthermore, it was worth noting that this enhancement depended on the cycling condition. The value of R_{ct} of Cu/Ni-F increased to 75.1 Ω if it was cycled with multiple C-rate for 53 cycles was the evidence.

The cross-sectional area of samples was imaged using SEM and EDS mapping. The spatial distribution of TiO_2 nanoparticles inside the micro-channels before and after cycling was obtained. Figure 44a-d are the results. Figures 44a and b are for the Cu/Ni-A sample with a flat Ni current collector. Figures 44c and d are for the Cu/Ni-F sample with high density vertically-aligned Ni micro-channels. The elemental distribution of Ti, O, and Ni for both samples before cycling is shown in the EDS mapping in Figures 44a and c. The overlapping of Ti and O pixels is highly visible. Furthermore, regions covered by Ni pixels were voids of the Ti and O pixels. Those results suggested that the distribution of TiO_2 nanoparticles was uniform on the Ni surface and/or inside the Ni micro-channels for both samples. Particularly for Cu/Ni-F, all of the inner walls of Ni micro-channels were fulfilled by the casted TiO_2 slurry with close contact. The EDS mapping result in Figure 44c shows the distribution of TiO_2 nanoparticles inside the micro-channels. After 500 cycles at 3.0 C, Figures 44b and d exhibit the SEM and EDS

results of Cu/Ni-A and Cu/Ni-F, respectively. In comparison, the spatial distribution of TiO_2 nanoparticles for both samples was consistent after many cycles. For the hierarchical Cu/Ni-F sample, the structural integrity of Ni micro-channels and distributional stability of TiO_2 nanoparticles can be observed through the EDS mapping in Figures 44d. The cross-sectional microscopic analysis confirmed the uniform, fulfilled, and stable distribution of nanosized TiO_2 nanoparticles in the inner walls of Ni micro-channels after numerous cycling. Furthermore, no obvious agglomerations or volume changes of TiO_2 nanoparticles can be observed from Figures 44b and d. This confirmed that the morphology and dimension of TiO_2 nanoparticles could be maintained after cycling.

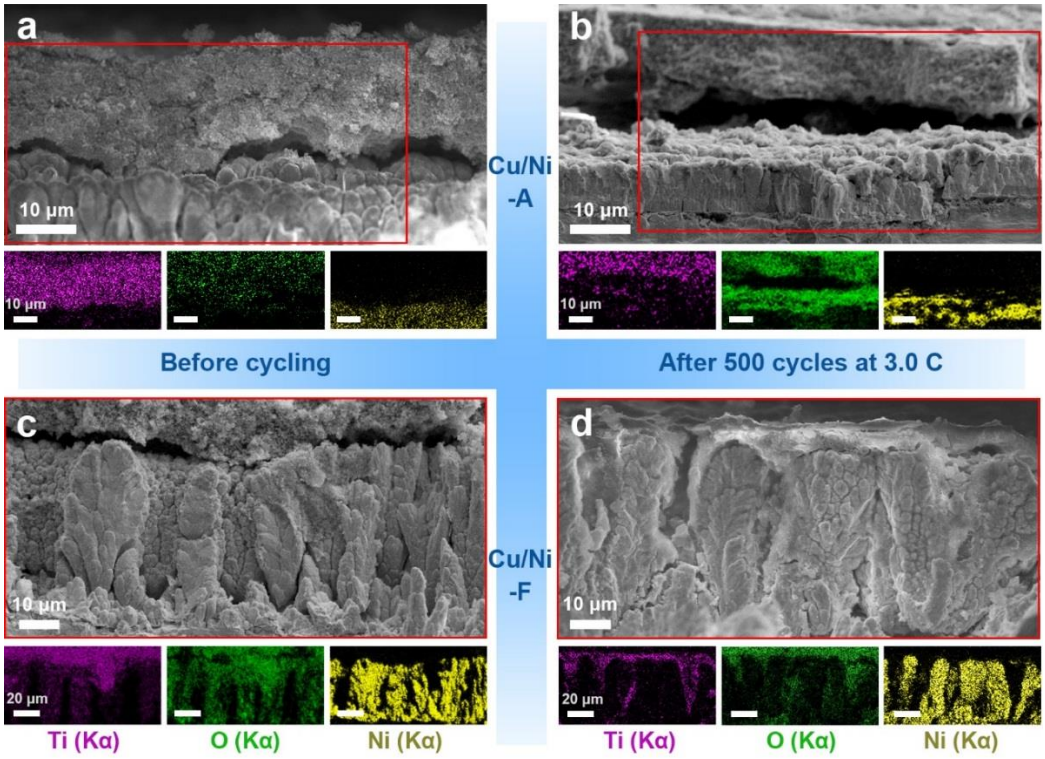

Figure 44. The microscopic analysis of the cross-sectional morphology of Cu/Ni/TiO_2 composite anode before and after cycling. The SEM photograph and EDS mapping results of Cu/Ni-A sample (a) before and (b) after 500 cycles at 3.0 C. The SEM photograph and EDS mapping result of Cu/Ni-F sample (c)

before and (d) after 500 cycles at 3.0 C. The red rectangular regions highlighted in (a)-(d) are the selected area for the EDS mapping.

Table 5. The list of capacity performance among recently published anatase-based LIB anodes.

Morphology of anatase	Max. specific capacity (mAh/g)	Cycle number	Capacity fading per cycle (%)	Measured current density (mA/g)	Ref.
Nanotubes	290	20	1.5	36	[163]
Nanosheets hierarchical spheres	202	100	0.14	170	[164]
Combined with graphene and carbon nanotubes	121.8	100	0.09	1680	[165]
Hollow peanuts	197	30	1.3	33.5	[166]
Hollow ellipsoids	184	30	1.1	33.5	[166]
Hollow capsules	165	30	0.9	33.5	[166]
Hollow pseudocubes	158	30	0.9	33.5	[166]
V^{5+} doped nanoparticles	239.0	30	0.36	0.1 mA/cm^2	[167]
Nanospheres	198	100	0.43	168	[168]
Hollow spheres	121	200	0.33	168	[178]
Fluorine-doped carbon-treated hollow spheres	255	100	0.18	84	[169]
Anatase and lithium phosphate at carbon nanotubes	276.4	200	0.13	160	[170]
Nanotubes wrapped with reduced graphene oxide	240	500	0.03	500	[179]
Nanoparticles on Cu/Ni porous current collector (this work)	**283.3**	**100**	**0.24**	**33.5**	[180]

The excellent electrochemical performance of the Cu/Ni-F sample as an anode of LIBs could be summarized as a synergistic effect between the nanosized TiO_2 active material and highly hierarchical and porous Cu/Ni current collector. As tabulated in Table 5, the electrochemical performance of the Cu/Ni/TiO_2 composite anode was competitive with a comparison with recently published anatase TiO_2-based anodes for LIBs. Figure 45 sketches the mechanism. First, the uniform-shaped and ~100 nm-sized anatase TiO_2 provided an increasing surface area as well as available sites for the

reaction with lithium ions. This could enhance the kinetics of reactions and shorten the lithium ion diffusion pathway. Meanwhile, the unique design of the micro-channels in the hierarchical Cu/Ni current collector offered the ultrahigh specific surface area. This feature offered more loaded TiO_2 NPs on the surface of current collector. From the electrochemical performance of Cu/Ni-A to F, the tendency of the more TiO_2 NPs loading resulted in the higher capacity value was clear. Furthermore, the densely distributed ~10 μm-sized vertically-aligned micro-channels accommodated the possible volume change of TiO_2 NPs during the cycling. Finally, the walls of adjacent channels could be considered as aligned pathways for electrons transport.

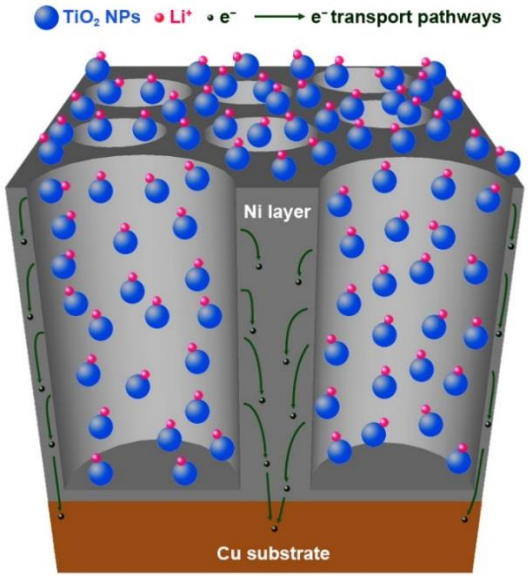

Figure 45. Three potential methods to modify the optical performance of RE-doped NPs and their mechanisms.

6.4 Summary

In this chapter, a novel anode made of Cu/Ni/TiO_2 composite had been generated using facile electrodeposition and wet-chemical methods. The hierarchical Cu/Ni current

collector fabricated by electrodeposition with NH_4^+ had the morphology of densely distributed vertically-aligned micro-channels. Anatase TiO_2 nanoparticles (NPs) had a well-defined crystalline structure and the dimension of ~100 nm. A one-step wet-chemical approach at room temperature followed by annealing was used to synthesize anatase TiO_2 NPs. After combining them into a Cu/Ni/TiO_2 hierarchical and porous anode through a slurry-casting procedure, evaluation was carried out and results showed that high density micro-channels on the Cu/Ni current collector could lead to greater capacity with high Coulombic efficiency. The optimized electrode was found in the sample Cu/Ni-F that had the maximum discharge specific capacity of 283.3 mAh/g at 0.1 C. After 100 cycles at 0.1 C, 75.8% of initial discharge capacity was retained. Moreover, the Cu/Ni-F anode could still deliver 84.5 mAh/g as the maximum discharge capacity at a high C-rate of 3.0 C with the retention of 41.7% after 500 cycles. The cross-sectional analysis using SEM and EDS validated the uniform, fulfilled, and consistent distribution of nanosized TiO_2 nanoparticles inside the Ni micro-channels after long-time cycling.

Nyquist plots through EIS tests showed superior performance of Cu/Ni-F anodes. It could be attributed to the synergistic effect of TiO_2 NPs and highly hierarchical Cu/Ni composites with vertically-aligned micro-channels. This unprecedented combination of active materials and current collectors could (i) offer excessive sites for electrochemical reactions; (ii) provide ultrahigh specific surface area to deposit more TiO_2 NPs; (iii) reduce the negative effect of structural pulverization of TiO_2 NPs due to cyclic volume changes; (iv) facilitate the electron transport through aligned pathways inside the current

collector. The Cu/Ni/TiO_2 hierarchical and highly porous composite exhibited high capacity of lithium ion storage, improved rate performance, long-term cycling stability. In the near future, other materials will be investigated as potential porous current collector and hierarchical structures. The unique design of the micro-channels-array current collector opens a new avenue to develop advanced electrodes.

CHAPTER VII

QUANTITATIVE THEORETICAL MODEL FOR MAXIMUM CAPACITY

As the most significant theoretical achievement in the whole research, this chapter constructed a quantitative model to determine the maximum specific capacity of one certain shaper-specific electrode material under a certain cyclic condition. This model is the first correlation between the actual capacity performance and the characteristics of the electrode material and C-rate. The specific values of sizes, aspect ratio, and surface area of one-dimensional (1D), two-dimensional (2D), and three-dimensional (3D) particles of active materials were involved in the calculation of the maximum capacity. The reliability of the model was validated by the comparison between calculated maximum capacities and measured maximum capacities of 25 published results.

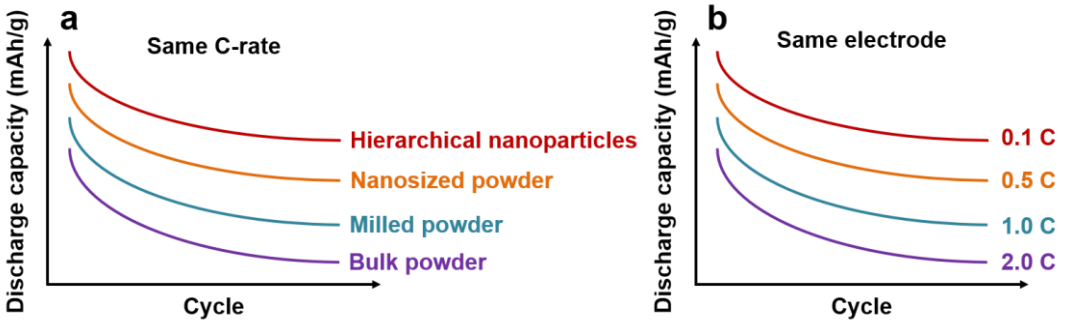

Figure 46. Two representative routine regulations of the capacity performance of a LIB cell. (a) The improvement of the capacity output of a cell with the same active material but different particle sizes. (b) The reduction of the capacity output of a cell with the identical active material and structure at faster C-rate.

7.1 Introduction to the theoretical capacity of lithium-ion electrodes

The electrochemical performance of the electrode materials (including cathode and anode) are the most critical part for a favorable design of LIBs. Properties such as higher electric conductivity, greater surface area, smaller particle size, improved reaction kinetics, and more stability under fast cyclic speed have become major components to enhance the electrochemical performance of electrodes [181]. The potential ability of the capacity output of a specific LIB cell under a specific cyclic condition is an important criterion to justify its electrochemical performance. Researchers usually use the term of "theoretical specific capacity" as a reference value to identify the performance [94]. In recent decade, an increasing number of novel electrode materials with nanostructures, shape-specific morphologies, and hierarchical architectures have been manufactured with versatile performance [51, 182, 183]. However, the conventional concept of the theoretical specific capacity for a type of electrode material can only provide a general and rough scale of the performance [94]. No detailed statuses such as structure, size, surface area, and cyclic C-rate are included. Therefore, for a specific LIB cell under a specific charge-discharge condition, a quantitative theoretical model to correlate the maximum specific capacity to the parameters of the electrode and condition is necessary to be proposed.

There are several routine regulations referring to the capacity performance of a LIB cell under different conditions. Figure 46 exhibits two of representative ones. Through the calculated results based on this model, one can answer questions about these regulations, such as: 1) what is the maximum capacity of the electrode with a

specific morphology used at a certain C-rate? 2) how to design the dimension, size, and aspect ratio for an electrode material to reach an expected goal of the capacity performance? and 3) what is the fastest acceptable C-rate to sufficiently release the potential of the capacity performance for a specific electrode?

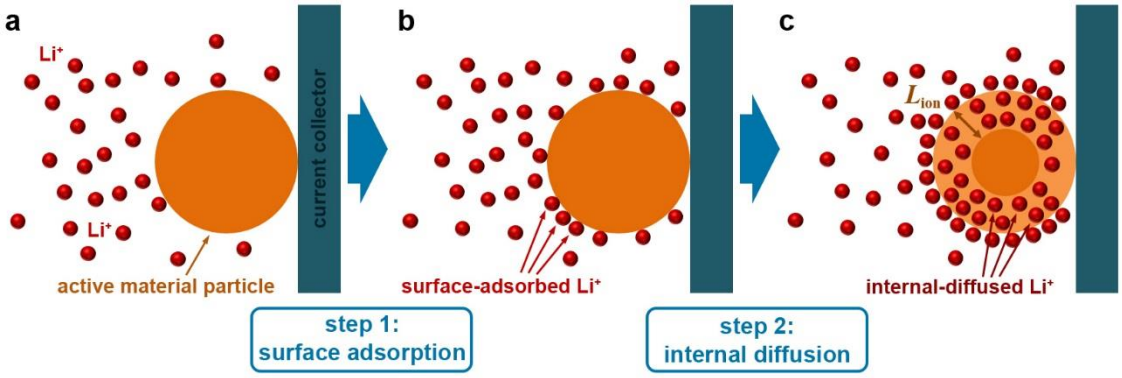

Figure 47. Illustration of the process of electrochemical reaction between lithium ions and an active material (AM) particle. (a) Before step 1 of surface adsorption. (b) During step 1 of surface adsorption. (c) During step 2 of internal diffusion.

7.2 Construction of the model

The theoretical model is based on a scenario of a type of electrode made of particles of the active material (marked as AM). This AM has a molar mass of M (in kg mol^{-1}) and bulk density of ρ (in kg m^{-3}). After applying an external potential with the current density at a C-rate of ζC, the AM electrode will react repeatedly with lithium ions inside a liquid (non-aqueous or aqueous) electrolyte of a LIB cell. If AM is a cathode, then the reaction is insertion of lithium ions (Equation (10)); if AM is an anode, then the reaction can be insertion (Equation (11)), alloying (Equation (12)), or conversion (Equation (13)) depending on the type of material. Please note that the parameter x, i.e. the transferred number of electron per reaction, is not necessarily to be

an integer. The theoretical maximum specific capacity of AM at C-rate of ζC is denoted as C_{ct} (in mAh g^{-1}). The theoretical analysis of the electrochemical reaction between AM and lithium ions is divided into two steps. The first step is the reaction during the surface adsorption of lithium ions; the second step is the reaction during the internal diffusion of lithium ions. Figure 47 illustrates the process with above two steps.

Cathode: $x\mathrm{Li}^+ + xe^- + \mathrm{M}_n\mathrm{X}_m \leftrightarrow \mathrm{Li}_x\mathrm{M}_n\mathrm{X}_m, \mathrm{M} = \mathrm{metals}, \mathrm{X} = \mathrm{O}, \mathrm{S}, \mathrm{etc.}$ (10)

Insertion anode: $x\mathrm{Li}^+ + xe^- + x\mathrm{C} \leftrightarrow \mathrm{Li}_x\mathrm{C}_x$ (11)

Alloying anode: $x\mathrm{Li}^+ + xe^- + \mathrm{M} \leftrightarrow \mathrm{Li}_x\mathrm{M}, \mathrm{M} = \mathrm{Si}, \mathrm{Ge}, \mathrm{or}\ \mathrm{Sn}.$ (12)

Conversion anode: $2m\mathrm{Li}^+ + 2me^- + \mathrm{M}_n\mathrm{X}_m \leftrightarrow n\mathrm{M} + m\mathrm{Li}_2\mathrm{X}, \mathrm{M} = \mathrm{metals}, \mathrm{X} = \mathrm{O}, \mathrm{S}.$ (13)

The contact between lithium ions in the electrolyte and solid AM surface is the precondition of the above reactions in Equations (10)-(13). This contact can be considered as type of liquid–solid Langmuir adsorption [184]. The electrochemical reaction is triggered immediately after the adsorption occurs (as shown in Figure 47b). The total specific surface area is denoted as A_s (in $m^2\ mol^{-1}$) for 1 mol of AM electrode (with N_A molecules or crystalline unit cells). For the Langmuir adsorption of lithium ions, there are n available surface sites per unit area of AM. For most of solid materials, the value of n is usually at the order of magnitude of 10^{18} sites per m^2 [185]. Then the total number of available surface sites in 1 mol of AM electrode is $A_s \cdot n$.

According to the theory of Langmuir adsorption, the fractional occupancy of the adsorbed lithium ions at the equilibrium θ_s is denoted as Equation (5):

$$\theta_s = \frac{K_{eq} c_{Li}}{1 + K_{eq} c_{Li}} \tag{14}$$

where c_{Li} is the concentration of lithium ions in the electrolyte, K_{eq} is the equilibrium constant of reactions of Equation (10)-(13). It is straightforward that K_{eq} can be simply written as Equation (15) for any type of reaction in Equation (10)-(13). In this case, the expression of θ_s can be rewritten as Equation (16). Therefore, the total number of surface sites that participate in the electrochemical reaction between lithium ions and AM N can be derived as Equation (17). Due to $x e^-$ is transferred for each reaction site, the total number of e^- transferred in the step of surface adsorption of lithium ions per mol AM electrode is expressed as N_e^s in Equation (18).

$$K_{eq} = \frac{1}{[Li^+]^x} = \frac{1}{c_{Li}^{\ x}} \tag{15}$$

$$\theta_s = \frac{K_{eq} c_{Li}}{1 + K_{eq} c_{Li}} = \frac{c_{Li}^{1-x}}{1 + c_{Li}^{1-x}} < 1 \tag{16}$$

$$N = A_s \cdot n \cdot \theta_s \tag{17}$$

$$N_e^S = N \cdot x = A_s n x \theta_s \tag{18}$$

The value of actual specific surface area A_s is correlated to the morphological feature of the particles of AM electrodes. Here in this study, the value of A_s is determined based on 1D, 2D, and 3D morphologies of AM micro- or nano-particles. Figure 48 demonstrates three typical shapes of 1D rods, 2D sheets, and 3D spheres owned by AM particles. For each type of shape in Figure 48, the smallest dimension of one single particle is defined as r (in m). The ratio between larger dimension(s) and the smallest dimension is denoted as the aspect ratio of μ. Obviously, μ should be equal or

greater than 1 in this case. Figure 48 marks the length, width, and thickness of the 1D rod, 2D sheet, and 3D sphere. For the ideal case of perfect monodispersion of AM particles, i.e. all AM particles have the identical values of r and μ, the value of can be calculated as Equation (19).

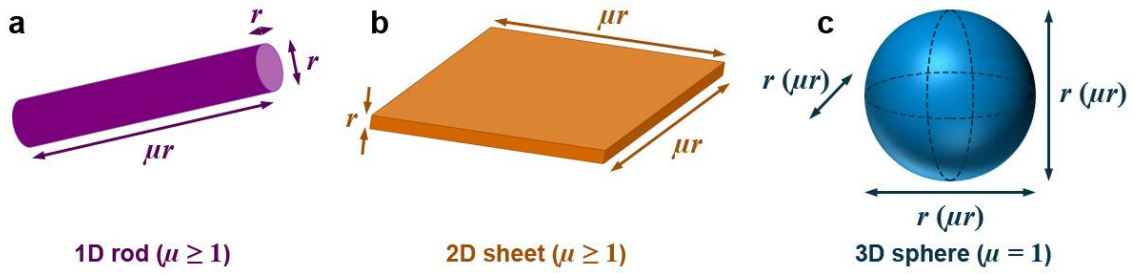

Figure 48. Representative shapes of the micro- or nano-particle of AM electrodes. (a) 1D rod. (b) 2D sheet. (c) 3D sphere. Their lengths, widths, and thicknesses are denoted by the smallest dimension r and aspect ratio μ.

$$A_s = \frac{2+\mu}{\mu} \cdot \frac{2M}{\rho r} \tag{19}$$

This derivation is based on the ideal assumption of the monodispersion and constant density of AM particles. The morphologies and dimension data of 1D, 2D, and 3D AM particles are shown in Figure 2 in the main text. To calculate the value of A_s, we consider the number of the rods/sheets/spheres for 1 mol AM particles and the surface area of each rod/sheet/sphere.

- 1D rods (d = 1 and μ > 1):

$$A_{s-1D} = \frac{M}{\rho \cdot \frac{\pi}{4} \mu r^3} \cdot \frac{2+\mu}{2} \cdot \pi r^2 = \frac{2+\mu}{\mu} \cdot \frac{2M}{\rho r} \tag{20}$$

- 2D sheets (d = 2 and μ > 1):

$$A_{s-2D} = \frac{M}{\rho \cdot \mu^2 r^3} \cdot 2\mu r^2 (2+\mu) = \frac{2+\mu}{\mu} \cdot \frac{2M}{\rho r} \tag{21}$$

- 3D spheres (d = 3 and μ = 1):

$$A_{s-3D} = \frac{6M}{\rho \cdot \pi r^3} \cdot \pi r^2 = \frac{6M}{\rho r} = \frac{2+\mu}{\mu} \cdot \frac{2M}{\rho r} \tag{22}$$

Actually, Equations (20)-(22) has the identical eventual format. Therefore, the value of A_s for perfectly monodispersed 1D, 2D, and 3D AM particles can be written as Equation (19).

Therefore, the expression of N_e^s can be rewritten as Equation (23) for the perfectly monodispersed AM particles.

$$N_e^s = \frac{2+\mu}{\mu} \frac{2M}{\rho r} nx\theta_s \tag{23}$$

The second step of internal diffusion of lithium ions is the main contributor of the transferred electrons after the process of surface adsorption. In the optimal case, all internal molecules of crystalline units of an AM particle can participate in the electrochemical reaction during the internal diffusion procedure. Then the total number of e^- transferred in the step of internal diffusion per mol AM electrode is obtained as N_e^i in Equation (24).

$$L_{ion} = \sqrt{D_{Li}\tau} \tag{24}$$

where D_{Li} (in $m^2\ s^{-1}$) is the diffusion coefficient of lithium ions inside the AM electrode. D_{Li} is an intrinsic parameter for a type of electrode material. τ (in s) is the characteristic diffusion time of lithium ions. It denotes the time for lithium ions to diffuse a length of L_{ion} inside the AM particle [186]. Therefore, the value of τ can be correlated to the value of C-rate ζ as $\tau = 3600/\zeta$.

Here in this research, the diffused volume ratio η is derived based on the perfectly monodispersed AM particles and homogenous diffusion. The homogenous diffusion describes the internal diffusion of lithium ions with the same length of L_{ion} from all surface of an AM particle. In this case, the value of η for a dD AM particle can be expressed by L_{ion}, r, μ, and d (d = 1, 2, or 3) as Equation (25).

$$\eta = 1 - \frac{(r - 2L_{ion})^{3-d}(\mu r - 2L_{ion})^{d}}{\mu^{d} r^{3}} \leq 1 \tag{25}$$

Similarly, this derivation is based on the assumption of the monodispersion of AM particles and homogenous diffusion of lithium ions. To prevent getting the trivial result of η = 1, here we define that $r > r_{ctd} = 2L_{ion}$. From the cross-sectional illustration shown in Figure 4 in the main text, we can obtain the values of η of 1D, 2D, and 3D AM particles as below:

- 1D rods (d = 1 and μ > 1):

$$\eta_{1D} = \frac{\frac{\pi}{4} r^{2} \mu r - \frac{\pi}{4}(r - 2L_{ion})^{2}(\mu r - 2L_{ion})}{\frac{\pi}{4} r^{2} \mu r} = 1 - \frac{(r - 2L_{ion})^{2}(\mu r - 2L_{ion})}{\mu r^{3}} \tag{26}$$

- 2D sheets (d = 2 and μ > 1):

$$\eta_{2D} = \frac{\mu^{2} r^{3} - (r - 2L_{ion})^{2}(\mu r - 2L_{ion})}{\mu^{2} r^{3}} = 1 - \frac{(r - 2L_{ion})(\mu r - 2L_{ion})^{2}}{\mu^{2} r^{3}} \tag{27}$$

- 3D spheres (d = 3 and μ = 1):

$$\eta_{3D} = \frac{\frac{\pi}{6} r^{3} - \frac{\pi}{6}(r - 2L_{ion})3}{\frac{\pi}{6} r^{3}} = 1 - \frac{(r - 2L_{ion})^{3}}{r^{3}} \tag{28}$$

Actually, the formats of Equations (26)-(28) can be unified after considering the values of d and μ for 1D, 2D, and 3D AM particles. Therefore, the generalized

expression of η for perfectly monodispersed 1D, 2D, and 3D AM particles can be summarized as Equation (25).

Therefore, the actual homogenously diffused volume of perfectly monodispersed AM electrodes can be obtained. Then the modified transferred number of e^- in the step of internal diffusion per mol AM electrode is denoted as N_e^{i}' in Equation (29).

$$N_e^{i}{}' = \eta \cdot N_A \cdot x \tag{29}$$

The electrochemical reaction in one charge-discharge cycle is completed after the successive taking place of surface adsorption and internal diffusion. Hence, the total number of transferred e^- in charge-discharge cycle per mol AM electrode (N_e) is the summation of Equation (23) and (29), i.e. Equation (30). If all of these transferred can be transported to the external circuit without the extra dissipation, the total theoretical maximum specific capacity of AM electrode in this cycle (C_{ct}) is derived as Eq. (31).

$$N_e = N_e^{S} + N_e^{i}{}' \tag{30}$$

$$C_{ct} = \frac{N_e e}{3.6M} \text{ (in mAh/g)} \tag{31}$$

After substituting the results in Equation (18) and (29), the general expression of is obtained as Equation (32). For the ideal case of perfect monodispersion of AM particles and homogenous diffusion, Equation (32) can be further derived as the formula of Equation (33). Equation (33) is the most significant result of this research due to its establishing a theoretical kinetic correlation between the experimental parameters of AM electrodes and maximum specific capacity.

$$C_{ct} = \frac{e}{3.6M}(\eta x N_A + A_s n x \theta_s) \text{ (in mAh/g)} \tag{32}$$

$$C_{\mathrm{ct}} = \frac{xe}{3.6M}\left[\left(1-\frac{(r-120\sqrt{D_{\mathrm{Li}}/\zeta})^{3-d}(\mu r-120\sqrt{D_{\mathrm{Li}}/\zeta})^{d}}{\mu^{d}r^{3}}\right)N_{\mathrm{A}}+\frac{2+\mu}{\mu}\frac{2Mn}{\rho r}\frac{c_{\mathrm{Li}}^{1-x}}{1+c_{\mathrm{Li}}^{1-x}}\right] \text{ (in mAh/g)} \quad (33)$$

7.3 Analysis of the constructed model

The change trends of value of C_{ct} under various conditions of changeable parameters are necessary to analyze. For a specific case of one certain AM electrode and liquid electrolyte, parameters of molar mass (M), bulk density (ρ), number of transferred electrons (x), specific available sites (n), and lithium ion diffusion coefficient (D_{Li}) of the AM electrode, and the lithium ion concentration of electrolyte are constant if the potential window is fixed. Then a hypothesized AM material with M = 100 kg mol^{-1}, ρ = 5000 kg m^{-3}, x = 1, n = 10^{18} per m^2, and D_{Li} = 10^{-20} m^2 s^{-1} is defined for the analysis. The concentration of electrolyte is set as c_{Li} = 1 mol L^{-1} according to the typical commercial electrolyte products. In this case, the value of C_{ct} is the function of variables of the smallest particle dimension r, aspect ratio μ, C-rate ζ, and dimension d. Three groups of the analysis will be conducted in following paragraphs.

1) For the same morphology (1D, 2D, or 3D) of AM particles with the same μ = 20, the change of values of η and C_{ct} with larger values of r (2–1000 nm) and constant C-rate of ζ = 0.1 will be analyzed;
2) For the same morphology (1D or 2D of AM particles with the same r = 40 nm, the change of values of η and C_{ct} with larger values of μ (2–500) and constant C-rate of ζ = 0.1 will be analyzed;

3) For the same 1D, 2D, or 3D AM particles with the same r = 40 nm and μ = 20, the change of values of η and C_{ct} with larger values of C-rate ζ (0.1–20) will be analyzed.

The change trends of η and C_{ct} for all groups are depicted as a series of scattered dots plots illustrated in Figures 49-51.

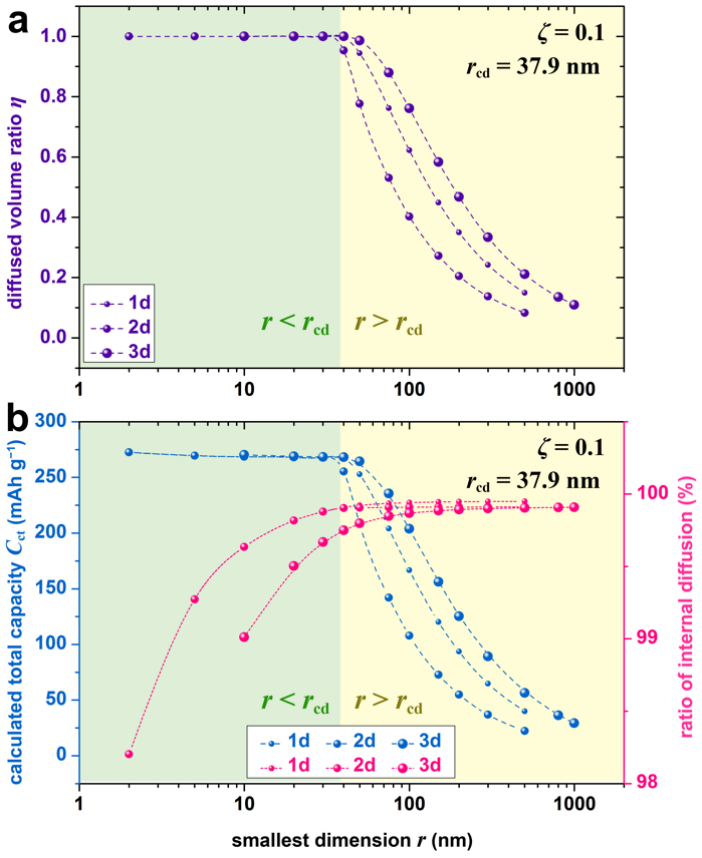

Figure 49. The plots of calculated results of diffused volume ratio η (violet), total theoretical maximum capacity C_{ct} (blue), and ratio of internal diffusion (pink) of 1D, 2D, and 3D AM particles with larger values of r.

For the first group of analysis, the impact to η and C_{ct} from various values of r can be separated into two regimes. The former regime highlighted by green-background

parts in Figure 49a and b has the appealing feature of the constant value of η = 1. This means that all of the internal parts of AM particles participate in the internal diffusion and electrochemical reaction. This regime is therefore named as “full diffusion regime”. Consequently, the values of C_{ct} reach maxima at ~270 mAh g^{-1}. The latter regime is marked by yellow backgrounds in Figure 49a and b. In this regime, the value of η become smaller than 1 and decrease drastically with the increase of r. The value of C_{ct} has a big drop accordingly. Only 10%~20% of maximum values of C_{ct} can be maintained after the values of r reach 500 nm. This regime is called as “partial diffusion regime”. The boundary of “full diffusion regime” and “partial diffusion regime” is located at the critical value of r that ensure the full diffusion. According of the definition of homogenous diffusion and Equation (24), this value of “critical size of full diffusion (r_{cfd})” is defined as Equation (34). For the hypothesized AM electrode, the value of r_{cfd} is 37.9 nm.

$$r_{cfd} = 2L_{ion} = 2\sqrt{D_{Li}\tau} = 120\sqrt{D_{Li}/\zeta} = 120\sqrt{10^{-20}/0.1} = 37.9\,\text{nm} \quad (34)$$

For the second group of analysis in Figure 50a and b, the values of η and C_{ct} show mild fading with increase of μ for 1D and 2D samples when $r > r_{cfd}$. More than 99% and around 95% of maximum values of C_{ct} can be retained after the values of μ reach 500 for 1D and 2D samples, respectively. This means that 2D AM electrodes have a steeper decrease of diffused volume and total capacity than 1D counterparts.

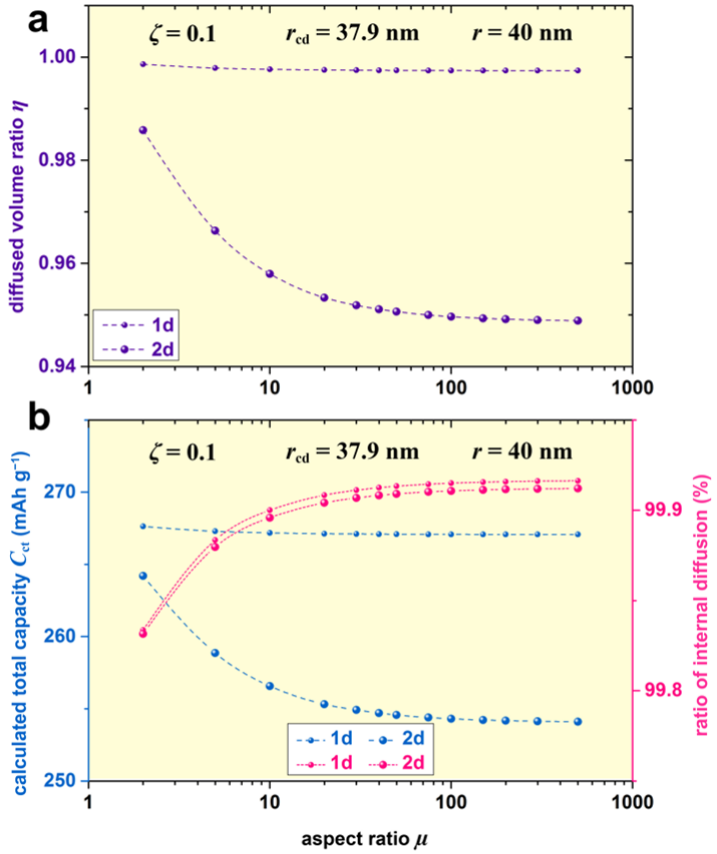

Figure 50. The plots of calculated results of diffused volume ratio η (violet), total theoretical maximum capacity C_{ct} (blue), and ratio of internal diffusion (pink) of 1D and 2D AM particles with larger values of μ.

For the third group of analysis in Figure 51a and b, the values of η and C_{ct} show significant decrease with increase of C-rate ζ for 1D, 2D, and 3D samples when r is always greater than r_{cfd}. The values of η and C_{ct} lose 80~90% after increasing the value of ζ, i.e. shortening the charge-discharge cyclic time. This is the reason why increasing the charge-discharge speed can suppress the capacity performance of one certain AM electrode. Furthermore, it is worth noticing that the contribution of C_{ct} from the surface adsorption is very small for all three groups of analysis. The pink dots in Figure 49b, 50b, and 51b all locate at regions greater than 98%. This phenomenon suggests that the

exclusive improvement of A_s of AM samples cannot significantly increase the capacity performance because the internal diffusion process plays a dominating role to contribute the transferred electrons.

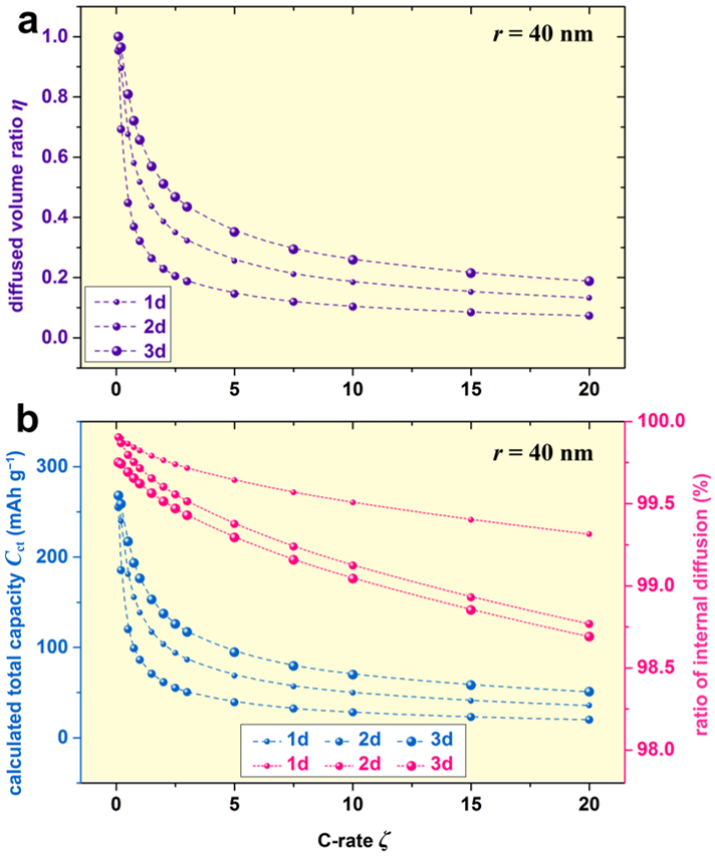

Figure 51. The plots of calculated results of diffused volume ratio η (violet), total theoretical maximum capacity C_{ct} (blue), and ratio of internal diffusion (pink) of 1D, 2D, and 3D AM particles with larger values of C-rate ζ.

The impact to the values of η for three groups of analysis is sketched as a series of cross-sectional illustration in Figure 52. According to the precondition of homogenous diffusion, the diffused volume of each AM particle in Figure 52 is marked by a light-colored uniform ring with the same width. For the first group, Figure 52a reveals the faster increasing rate of the dark undiffused volume than light diffused

volume if the values of r increase. Therefore, the diffused volume ratio η has to reduce even though the absolute value of diffused volume keeps rising. For the second group, Figure 52b demonstrates the similar regulation. The greater undiffused volume with the larger value of aspect ratio μ leads to the shrinking diffused volume ratio η. For the third group, Figure 52c shows the thinner diffused layer of 1D, 2D, and 3D AM particles if the value of C-rate ζ increases. This tendency is attributed to the negative correlation between L_{ion} and ζ for a specific AM electrode. Obviously, the smaller value of diffusion length L_{ion} causes the dropping of diffused volume ratio η if the total volume of AM particles is constant.

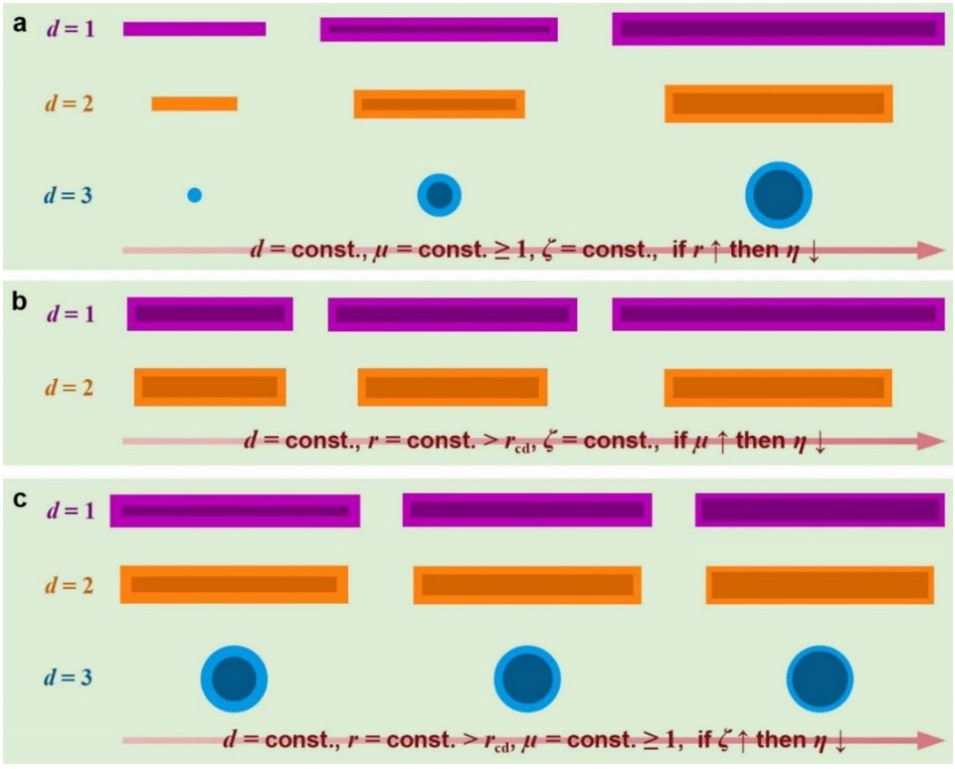

Figure 52. The cross-sectional illustration of the change trends of homogenously diffused volume ratio η for three groups of analysis. (a) 1D, 2D, and 3D AM particles with larger values of r. (c) 1D and 2D AM particles with larger values of μ. (c) 1D, 2D, and 3D AM particles with larger values of C-rate ζ. For each particle, the region with light color marks the diffused volume and the region with dark color marks the undiffused volume.

7.4 Validation of the reliability of the model

The reliability of this proposed theoretical model needs to be confirmed. Twenty-five experimental results of various types of AM electrodes for LIBs published in recent years are selected as the samples. These samples have different materials and their morphologies span all three dimensions of 1D [112, 187-192], 2D [8, 168, 193-198], and 3D [180, 199-206]. Their parameters are listed in Table 6. For these samples, the concentration of lithium ions in the electrolyte is constant as $c_{Li} = 1$ mol L^{-1}, which is the typical value for most of commercial electrolytes [94]. For the simplification, the values of available surface sites per unit area n for all these sample are assumed as 10^{18} per m^2. In real cases, the value of D_{Li} for each sample usually has a wide range due to the complicated and distinct actual diffusion processes. Therefore, an upper and lower threshold of the value of diffused volume ratio η can be calculated for each sample based on Equation (25). Accordingly, a minimum and maximum value of C_{ct}, i.e. $C_{ct\text{-}min}$ and $C_{ct\text{-}max}$, can be derived from Equation (25), respectively. Table 7 compares the values among $C_{ct\text{-}min}$, $C_{ct\text{-}max}$, measured maximum specific capacity $C_{m\text{-}max}$, and theoretical specific capacity C_t of every published result. A scatter dots plot of Figure 53 is demonstrated to compare between C_{ct} and $C_{m\text{-}max}/C_t$ for each sample. It is noticed that most of published results have values of C_{ct} as fixed points. The reason is that these samples have calculated values of diffused volume ratio η as $\eta_{min} = \eta_{max} = 1$. This implies that the morphological design of these sample can ensure that $r < r_{ctd} = 2L_{ion}$. In this case, all of the volume of AM particles for each sample can be sufficiently utilized

to the internal diffusion process. Hence their values of C_{ct} are quite approaching to $C_{m\text{-}max}$ and C_t (errors are smaller than ~25%). Meanwhile, there are few published results whose calculated values of η and C_{ct} have ranges. The ranges of C_{ct} are marked as error bars in horizontal axis. These wide ranges of C_{ct} mean the possible existence of undiffused volume inside the AM particles. Overall, the condense distribution of data balls and stars nearby the red dashed "perfectly matched" line for most of the samples indicates the convincing reliability of the constructed theoretical model.

Table 6. The parameters of the AM electrodes and cyclic conditions of published related results.

Active Material	d	r (nm)	μ	ζ	min(log D_{Li})	max(log D_{Li})	x	Ref.
Fe_2O_3	1	60	10	0.1	−16	−14	6	[187]
Fe_3O_4		50	12	0.1	−19	−17	8	[187]
$Li_4Ti_5O_{12}$		90	90	5	−17	−13	3	[188]
TiO_2		200	100	0.2	−19	−13	1	[112]
TiO_2		180	500	0.1	−19	−13	1	[189]
Co_3O_4		200	10	2.25	−15	−14	8	[190]
$Li_4Ti_5O_{12}$		50	400	2	−17	−13	3	[191]
ZnO		70	20	0.2	−18	−16	3	[192]
$FeVO_4$	2	25	12	0.15	−16	−14	8	[193]
Si		25	1000	0.05	−17	−16	4	[194]
MoO_3		30	200	0.09	−17	−15	6	[195]
$Li_4Ti_5O_{12}$		14	100	50	−17	−13	3	[168]
$LiFePO_4$		50	300	10	−18	−15	1	[196]
$LiMn_2O_4$		50	25	1	−15	−11	1	[197]
V_2O_5		50	1000	5	−17	−16	2	[8]
V_2O_5		50	40	0.2	−17	−16	1	[198]
TiO_2	3	100	1	0.2	−19	−13	0.6	[199]
SnO_2		7.5		0.64	−19	−17	4.4	[200]
Fe_3O_4		30		1	−19	−17	8	[201]
MoO_2		45		0.24	−14	−13	4	[202]
Sn		15		0.2	−20	−18	4.4	[203]
Fe_3O_4		9.6		0.11	−19	−17	9	[204]
TiO_2		20		9	−19	−13	0.5	[205]
$LiFePO_4$		80		1	−18	−15	1	[206]
TiO_2		100		0.1	−19	−13	1	[180]

Table 7. The comparison of the calculated maximum specific capacity C_{ct}, measured maximum specific capacity $C_{m\text{-}max}$, and theoretical specific capacity C_t of published related results.

Active Material	d	η_{min}	η_{max}	$C_{ct\text{-}min}$ (mAh g^{-1})	$C_{ct\text{-}max}$ (mAh g^{-1})	$C_{m\text{-}max}$ (mAh g^{-1})	C_t (mAh g^{-1})	Ref.
Fe_2O_3	1	1	1	1006.2	1006.2	980.9	1006	[187]
Fe_3O_4		1	1	914.23	914.23	914.9	925	[187]
$Li_4Ti_5O_{12}$		0.23	1	41.5	175.7	157	175	[188]
TiO_2		0.67	1	224.4	335.0	207	335	[112]
TiO_2		0.89	1	297.8	335.0	255	335	[189]
Co_3O_4		1	1	913.2	913.2	1050	890	[190]
$Li_4Ti_5O_{12}$		1	1	176.4	176.4	174	175	[191]
ZnO		1	1	986.5	986.5	890	988	[192]
$FeVO_4$	2	1	1	1257.8	1257.8	1316	1300	[193]
Si		1	1	3347.8	3347.8	3350	3685	[194]
MoO_3		1	1	1117.2	1117.2	880	1116	[195]
$Li_4Ti_5O_{12}$		1	1	180.7	180.7	134	175	[168]
$LiFePO_4$		0.76	1	129.2	169.8	100	170	[196]
$LiMn_2O_4$		1	1	148.2	148.2	128	148	[197]
V_2O_5		1	1	294.7	294.7	250	294	[8]
V_2O_5		1	1	147.4	147.4	165.6	147	[198]
TiO_2	3	0.99	1	201.6	202.3	204	167.5	[199]
SnO_2		1	1	793.3	793.3	759.6	782	[200]
Fe_3O_4		1	1	941.1	941.1	870	925	[201]
MoO_2		1	1	838.3	838.3	986.9	838	[202]
Sn		1	1	998.5	998.5	1100	992	[203]
Fe_3O_4		1	1	1051.7	1051.7	1130	925	[204]
TiO_2		0.95	1	160.0	168.3	167	167.5	[205]
$LiFePO_4$		1	1	170.1	170.1	170	170	[206]
TiO_2		1	1	268.2	268.2	283.3	335	[180]

The above comparison results reveal the convincing reliability of this theoretical model. However, it is necessary to point out that this model cannot describe all cases of the cycling process of one certain AM electrode. It has several following limitations. Firstly, this model can only describe the maximum capacity of an LIB test due to it is based on the ideal status of the AM electrode. The phenomenon of capacity fading with the prolonged cycles is not included in this model. Secondly, this model is based on the perfect monodispersion of AM particles. The morphologies of AM particles are also

restricted as 1D rods, 2D sheets, and 3D spheres. There are an increasing number of novel types of AM particles with fancy morphologies such as core–shell, multilayered, porous, and hierarchical structures [150, 207-210]. The parameter of r, μ, A_s, and η will be quite complicated to be determined. Thirdly, the simplified assumption of homogenous diffusion cannot be suitable for all actual cases of internal diffusion of lithium ions. The diffusion lengths may be uneven with preference according to the crystalline orientations. Fourthly, this model only consider the contribution of AM particles without current collectors. Actually, the enhancement effect to the electrochemical performance from hierarchical or 3D current collectors has been extensively reported [211, 212]. Some modifications of corrections of this model will be necessary after considering the assistance of current collectors.

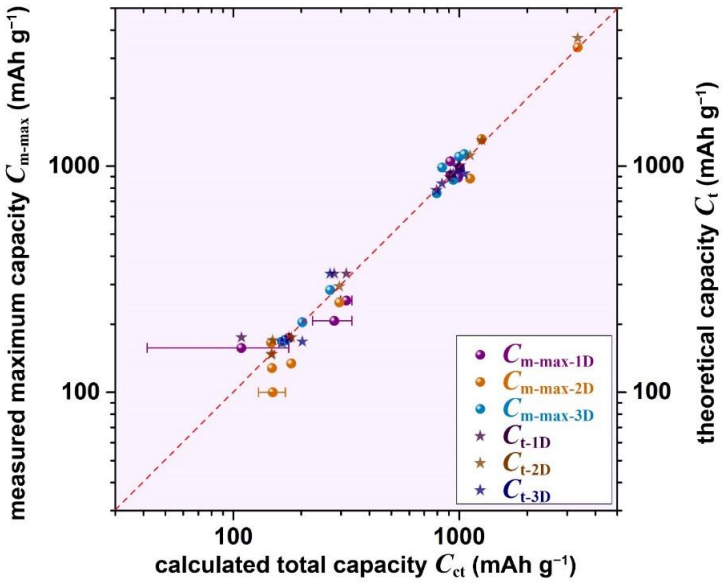

Figure 53. The comparison among calculated total maximum capacity ($C_{ct\text{-}min}$ and $C_{ct\text{-}max}$), measured maximum specific capacity $C_{m\text{-}max}$, and theoretical specific capacity C_t of 25 recently published results of AM electrodes. Balls are data points of $C_{m\text{-}max}$ collected from each sample. Accompanied error bars are ranges of C_{ct} calculated for corresponding sample. Stars are C_t of each sample. The red dashed line marks the perfect matching between C_{ct} and $C_{m\text{-}max}/C_t$.

7.5 Summary

In this chapter, a quantitative electrochemical model to determine the maximum capacity of one specific active material with specific morphology and cycling condition was constructed and analyzed at the first time. This model is based on the electrochemical reaction process with two steps. The first steps is the surface adsorption of lithium ions. This step is described by the partial occupancy of lithium ions according to liquid–solid Langmuir adsorption. The second step is the internal diffusion of the lithium ions. Various diffusion lengths and diffused volume ratios were obtained for 1D/2D/3D active materials under the conditions of various speeds of charge-discharge, i.e. C-rates. The value of total maximum specific capacity was subsequently calculated by summing up the transferred electrons in both steps. The contribution of capacity from internal diffusion is always significantly greater than that of surface adsorption. Through a series of control analysis for a hypothesized active material, the effects on the total maximum capacity from the various smallest sizes of particles, aspect ratios of particles, and C-rates were systematically evaluated. It is found that larger particle size of active materials and faster C-rates will result in the drastic reduction of maximum capacity. Meanwhile, the greater aspect ratio of active materials can also slightly decrease the maximum capacity.

Furthermore, the reliability of this model was confirmed through the comparison between calculated maximum capacities and measured maximum capacities of 25 published results. The excellent matching after comparison indicates the convincing reliability of the model although there are several simplification and limitations in it. In a

word, this quantitative theoretical model offers a feasible approach to calculate the maximum capacity of one active material under a specific charge-discharge condition. The direct correlation between the measured capacity value and morphological and electrochemical parameters of electrodes will open a new avenue for the design strategies of electrode materials for advanced energy storage technologies.

CHAPTER VIII

CONCLUSIONS AND OUTLOOKS

8.1 Conclusions

This doctoral research systematically and comprehensively investigated the emerging types of hierarchical nanomaterials and their applications on enhanced wetting property, improved heat dissipation, and excellent electrochemical energy storage performance. Furthermore, the quantitative correlation between the maximum capacity and the morphological features of a specific LIB electrode is also theoretically studied and validated.

The following items are the highlights of major findings and conclusions of this research described in previous chapters:

1. A novel type of aluminum porous structure with numerous vertically-aligned pores was fabricated through a simple method of electrochemical etching. The mechanism of the pores formation was discovered as the selective etching with the assistance of hydrogen bubbles. The enhanced hydrophilicity of the as-fabricated aluminum porous structure was confirmed;
2. Two-dimensional V_2O_5 nanosheets and assembled three-dimensional micro-peonies were hydrothermally deposited on the surface of hierarchical Ni micro-channeled substrate. The ultrahigh surface area and improved heat dissipation property was characterized. Corresponding mechanisms were analyzed accordingly;

3. Nanosized anatase TiO_2 particles with uniform size and spherical shape were synthesized through a fast and cost-effective wet-chemical approach. After combining the as-fabricated TiO_2 nanoparticles with porous Cu/Ni micro-channeled current collectors, the hierarchical Cu/Ni/TiO_2 nanocomposite was used as a novel anode of LIBs. The excellent electrochemical performance and relevant mechanism were investigated;
4. A quantitative theoretical model to describe the electrochemical reaction between lithium ions and active material particles was proposed using the idea of surface adsorption and internal diffusion. This model provided a direct method to theoretically calculate the maximum capacity value of a specific type of active material particles under a specific cyclic condition. The regulation and reliability of this proposed model was systematically analyzed and validated.

8.2 Outlooks

The following perspective directions are proposed in this section for the future research:

1. The novel types of porous thin substrate with vertically-align channeled structures are necessary to be fabricated. The innovation of the approaches, materials, and morphologies is critical for the application of superhydrophobicity.

2. The novel design of the super-hierarchical nanocomposites fabricated through the direct deposition is a significant topic to develop advanced 3D electrodes for next-generation high-capacity-density and flexible electrochemical energy storage devices.
3. Detailed theoretical investigation referring to the electrochemical kinetics of complicated hierarchical micro-electrodes can promote the design strategies of advanced battery cells. The contribution of the hierarchical current collectors is also necessary to be considered.

REFERENCES

1. Lakes, R., *Materials with structural hierarchy.* Nature, 1993. **361**(6412): p. 511-515.

2. Zhao, Y. and L. Jiang, *Hollow micro/nanomaterials with multilevel interior structures.* Advanced Materials, 2009. **21**(36): p. 3621-3638.

3. Goriparti, S., E. Miele, F. De Angelis, E. Di Fabrizio, R. Proietti Zaccaria, and C. Capiglia, *Review on recent progress of nanostructured anode materials for Li-ion batteries.* Journal of Power Sources, 2014. **257**: p. 421-443.

4. Liu, J., S.Z. Qiao, S. Budi Hartono, and G.Q.M. Lu, *Monodisperse yolk–shell nanoparticles with a hierarchical porous structure for delivery vehicles and nanoreactors.* Angewandte Chemie International Edition, 2010. **122**(29): p. 5101-5105.

5. Tan, J. and X. Huang, *Ultra-thin nanosheets-assembled hollowed-out hierarchical α-Fe 2 O 3 nanorods: Synthesis via an interface reaction route and its superior gas sensing properties.* Sensors and Actuators B: Chemical, 2016. **237**: p. 159-166.

6. Lu, Y., Y. Ma, S. Ma, W. Jin, S. Yan, X. Xu, and Q. Chen, *Curly porous NiO nanosheets with enhanced gas-sensing properties.* Materials Letters, 2017. **190**: p. 252-255.

7. Sun, P., W. Zhao, Y. Cao, Y. Guan, Y. Sun, and G. Lu, *Porous SnO2 hierarchical nanosheets: hydrothermal preparation, growth mechanism, and gas sensing properties.* Cryst Eng Comm, 2011. **13**(11): p. 3718-3724.

8. Liu, J., Q. Zheng, M.D. Goodman, H. Zhu, J. Kim, N.A. Krueger, H. Ning, X. Huang, J. Liu, and M. Terrones, *Graphene sandwiched mesostructured Li‐ion battery electrodes.* Advanced Materials, 2016. **28**: p. 7696-7702.

9. Liu, H. and H. Liu, *Preparing micro/nano dumbbell-shaped CeO2 for high performance electrode materials.* Journal of Alloys and Compounds, 2016. **681**: p. 342-349.

10. Pérez-Ramírez, J., C.H. Christensen, K. Egeblad, C.H. Christensen, and J.C. Groen, *Hierarchical zeolites: enhanced utilisation of microporous crystals in catalysis by advances in materials design.* Chemical Society Reviews, 2008. **37**(11): p. 2530-2542.

11. Schreiber, R., J. Do, E.-M. Roller, T. Zhang, V.J. Schüller, P.C. Nickels, J. Feldmann, and T. Liedl, *Hierarchical assembly of metal nanoparticles, quantum dots and organic dyes using DNA origami scaffolds.* Nature Nanotechnology, 2014. **9**(1): p. 74-78.

12. Liu, Y., Y. Jiao, Z. Zhang, F. Qu, A. Umar, and X. Wu, *Hierarchical SnO2 nanostructures made of intermingled ultrathin nanosheets for environmental remediation, smart gas sensor, and supercapacitor applications.* ACS Applied Materials & Interfaces, 2014. **6**(3): p. 2174-2184.

13. Vallet‐Regí, M., F. Balas, and D. Arcos, *Mesoporous materials for drug delivery.* Angewandte Chemie International Edition, 2007. **46**(40): p. 7548-7558.

14. Zhang, J., X. Liu, G. Neri, and N. Pinna, *Nanostructured materials for room-temperature gas sensors.* Advanced Materials, 2016. **28**(5): p. 795-831.

15. Byrappa, K. and T. Adschiri, *Hydrothermal technology for nanotechnology.* Progress in Crystal Growth and Characterization of Materials, 2007. **53**(2): p. 117-166.

16. Baruah, S. and J. Dutta, *Hydrothermal growth of ZnO nanostructures.* Science and Technology of Advanced Materials, 2016. **10**(1): p. 013001

17. Zhang, W.H., C. Liang, H. Sun, Z. Shen, Y. Guan, P. Ying, and C. Li, *Synthesis of ordered mesoporous carbons composed of nanotubes via catalytic chemical vapor deposition.* Advanced Materials, 2002. **14**(23): p. 1776-1778.

18. Liu, H., L. Feng, J. Zhai, L. Jiang, and D. Zhu, *Reversible wettability of a chemical vapor deposition prepared ZnO film between superhydrophobicity and superhydrophilicity.* Langmuir, 2004. **20**(14): p. 5659-5661.

19. Park, J., W.G. Moon, G.-P. Kim, I. Nam, S. Park, Y. Kim, and J. Yi, *Three-dimensional aligned mesoporous carbon nanotubes filled with Co3O4 nanoparticles for Li-ion battery anode applications.* Electrochimica Acta, 2013. **105**: p. 110-114.

20. Nithiyanantham, U., A. Ramadoss, and S. Kundu, *Supercapacitor and dye-sensitized solar cell (DSSC) applications of shape-selective TiO2 nanostructures.* RSC Advances, 2014. **4**(67): p. 35659-35672.

21. Wang, K., S. Luo, Y. Wu, X. He, F. Zhao, J. Wang, K. Jiang, and S. Fan, *Super‐aligned carbon nanotube films as current collectors for lightweight and flexible lithium ion batteries.* Advanced Functional Materials, 2013. **23**(7): p. 846-853.

22. Qiu, H., Z.M. Hudson, M.A. Winnik, and I. Manners, *Multidimensional hierarchical self-assembly of amphiphilic cylindrical block comicelles.* Science, 2015. **347**(6228): p. 1329-1332.

23. Whang, D., S. Jin, Y. Wu, and C.M. Lieber, *Large-scale hierarchical organization of nanowire arrays for integrated nanosystems.* Nano Letters, 2003. **3**(9): p. 1255-1259.

24. Cote, L.J., F. Kim, and J. Huang, *Langmuir−Blodgett assembly of graphite oxide single layers.* Journal of the American Chemical Society, 2008. **131**(3): p. 1043-1049.

25. Jiang, P. and M.J. McFarland, *Large-scale fabrication of wafer-size colloidal crystals, macroporous polymers and nanocomposites by spin-coating.* Journal of the American Chemical Society, 2004. **126**(42): p. 13778-13786.

26. Xia, D., A. Biswas, D. Li, and S.R. Brueck, *Directed self-assembly of silica nanoparticles into nanometer-scale patterned surfaces using spin-coating.* Advanced Materials, 2004. **16**(16): p. 1427-1432.

27. Qiu, J., M. Guo, Y. Feng, and X. Wang, *Electrochemical deposition of branched hierarchical ZnO nanowire arrays and its photoelectrochemical properties.* Electrochimica Acta, 2011. **56**(16): p. 5776-5782.

28. Xia, X.-h., J.-p. Tu, X.-l. Wang, C.-d. Gu, and X.-b. Zhao, *Hierarchically porous NiO film grown by chemical bath deposition via a colloidal crystal template as an electrochemical pseudocapacitor material.* Journal of Materials Chemistry, 2011. **21**(3): p. 671-679.

29. Teo, W.E. and S. Ramakrishna, *A review on electrospinning design and nanofibre assemblies.* Nanotechnology, 2006. **17**(14): p. R89.

30. Teo, W.-E. and S. Ramakrishna, *Electrospun nanofibers as a platform for multifunctional, hierarchically organized nanocomposite.* Composites Science and Technology, 2009. **69**(11): p. 1804-1817.

31. Byrappa, K. and M. Yoshimura, *Handbook of hydrothermal technology*. 2001: William Andrew. Norwich, NY.

32. Puma, G.L., A. Bono, D. Krishnaiah, and J.G. Collin, *Preparation of titanium dioxide photocatalyst loaded onto activated carbon support using chemical vapor deposition: A review paper.* Journal of hazardous Materials, 2008. **157**(2): p. 209-219.

33. Zhang, Y., L. Zhang, and C. Zhou, *Review of chemical vapor deposition of graphene and related applications.* Accounts of chemical research, 2013. **46**(10): p. 2329-2339.

34. De Volder, M. and A.J. Hart, *Engineering hierarchical nanostructures by elastocapillary self-assembly.* Angewandte Chemie International Edition, 2013. **52**(9): p. 2412-2425.

35. Rehnlund, D., M. Valvo, K. Edström, and L. Nyholm, *Electrodeposition of vanadium oxide/manganese oxide hybrid thin films on nanostructured aluminum substrates.* Journal of The Electrochemical Society, 2014. **161**(10): p. D515-D521.

36. Nuraje, N., W.S. Khan, Y. Lei, M. Ceylan, and R. Asmatulu, *Superhydrophobic electrospun nanofibers.* Journal of Materials Chemistry A, 2013. **1**(6): p. 1929-1946.

37. Grzelczak, M., J. Vermant, E.M. Furst, and L.M. Liz-Marzán, *Directed self-assembly of nanoparticles.* ACS Nano, 2010. **4**(7): p. 3591-3605.

38. Berteloot, G., A. Hoang, A. Daerr, H.P. Kavehpour, F. Lequeux, and L. Limat, *Evaporation of a sessile droplet: Inside the coffee stain.* Journal of Colloid and Interface Science, 2012. **370**(1): p. 155-161.

39. Kim, S., A.A. Polycarpou, and H. Liang, *Active control of surface forces via nanopore structures.* APL Materials, 2013. **1**(3): p. 032118.

40. Callister, W.D. and D.G. Rethwisch, *Materials science and engineering: an introduction*. Vol. 7. 2007: Wiley New York. New york, NY.

41. Mai, L., X. Tian, X. Xu, L. Chang, and L. Xu, *Nanowire electrodes for electrochemical energy storage devices.* Chemical Reviews, 2014. **114**(23): p. 11828-11862.

42. David, L.R., Thomas, *Handbook of batteries*. 3rd ed. 2002: McGraw-Hill. New York, NY

43. Whittingham, M.S., *Lithium batteries and cathode materials.* Chemical Reviews, 2004. **104**(10): p. 4271-4302.

44. Vetter, J., P. Novák, M.R. Wagner, C. Veit, K.C. Möller, J.O. Besenhard, M. Winter, M. Wohlfahrt-Mehrens, C. Vogler, and A. Hammouche, *Ageing mechanisms in lithium-ion batteries.* Journal of Power Sources, 2005. **147**(1–2): p. 269-281.

45. Guo, Y.G., J.S. Hu, and L.J. Wan, *Nanostructured materials for electrochemical energy conversion and storage devices.* Advanced Materials, 2008. **20**(15): p. 2878-2887.

46. Fergus, J.W., *Recent developments in cathode materials for lithium ion batteries.* Journal of Power Sources, 2010. **195**(4): p. 939-954.

47. Tarascon, J.M., *Key challenges in future Li-battery research.* Philosophical Transactions A: Mathematical, Physical and Engineering Sciences, 2010. **368**(1923): p. 3227-41.

48. Lu, L., X. Han, J. Li, J. Hua, and M. Ouyang, *A review on the key issues for lithium-ion battery management in electric vehicles.* Journal of Power Sources, 2013. **226**: p. 272-288.

49. Rohan, J.F., M. Hasan, S. Patil, D.P. Casey, and T. Clancy, *Energy storage: battery materials and architectures at the nanoscale.* ICT-Energy-Nanoscale energy management concepts towards Zero-Power Information and Communication Technology, 2014.

50. Nitta, N., F. Wu, J.T. Lee, and G. Yushin, *Li-ion battery materials: present and future.* Materials Today, 2015. **18**(5): p. 252-264.

51. Sun, M.H., S.Z. Huang, L.H. Chen, Y. Li, X.Y. Yang, Z.Y. Yuan, and B.L. Su, *Applications of hierarchically structured porous materials from energy storage and conversion, catalysis, photocatalysis, adsorption, separation, and sensing to biomedicine.* Chemical Society Review, 2016. **45**(12): p. 3479-563.

52. Bard, A.J., L.R. Faulkner, J. Leddy, and C.G. Zoski, *Electrochemical methods: fundamentals and applications*. Vol. 2. 1980: Wiley New York. New York, NY.

53. Zhang, Y., H. Feng, X. Wu, L. Wang, A. Zhang, T. Xia, H. Dong, X. Li, and L. Zhang, *Progress of electrochemical capacitor electrode materials: A review.* International Journal of Hydrogen Energy, 2009. **34**(11): p. 4889-4899.

54. Snook, G.A., P. Kao, and A.S. Best, *Conducting-polymer-based supercapacitor devices and electrodes.* Journal of Power Sources, 2011. **196**(1): p. 1-12.

55. Ghosh, A. and Y.H. Lee, *Carbon‐based electrochemical capacitors.* Chem Sus Chem, 2012. **5**(3): p. 480-499.

56. Wang, F., S. Xiao, Y. Hou, C. Hu, L. Liu, and Y. Wu, *Electrode materials for aqueous asymmetric supercapacitors.* RSC Advances, 2013. **3**(32): p. 13059-13084.

57. Yan, J., Q. Wang, T. Wei, and Z. Fan, *Recent advances in design and fabrication of electrochemical supercapacitors with high energy densities.* Advanced Energy Materials, 2014. **4**(4). p. 1300816

58. Jin, B., J.-U. Kim, and H.-B. Gu, *Electrochemical properties of lithium–sulfur batteries.* Journal of Power Sources, 2003. **117**(1): p. 148-152.

59. Kolosnitsyn, V. and E. Karaseva, *Lithium-sulfur batteries: Problems and solutions.* Russian Journal of Electrochemistry, 2008. **44**(5): p. 506-509.

60. Yin, Y.X., S. Xin, Y.G. Guo, and L.J. Wan, *Lithium–sulfur batteries: electrochemistry, materials, and prospects.* Angewandte Chemie International Edition, 2013. **52**(50): p. 13186-13200.

61. Nazar, L.F., M. Cuisinier, and Q. Pang, *Lithium-sulfur batteries.* MRS Bulletin, 2014. **39**(05): p. 436-442.

62. Manthiram, A., Y. Fu, S.-H. Chung, C. Zu, and Y.-S. Su, *Rechargeable lithium–sulfur batteries.* Chemical Reviews, 2014. **114**(23): p. 11751-11787.

63. Girishkumar, G., B. McCloskey, A. Luntz, S. Swanson, and W. Wilcke, *Lithium–air battery: promise and challenges.* The Journal of Physical Chemistry Letters, 2010. **1**(14): p. 2193-2203.

64. Zhang, D., R. Li, T. Huang, and A. Yu, *Novel composite polymer electrolyte for lithium air batteries.* Journal of Power Sources, 2010. **195**(4): p. 1202-1206.

65. Bruce, P.G., L.J. Hardwick, and K. Abraham, *Lithium–air and lithium–sulfur batteries.* MRS Bulletin, 2011. **36**(07): p. 506-512.

66. Shao, Y., S. Park, J. Xiao, J.-G. Zhang, Y. Wang, and J. Liu, *Electrocatalysts for nonaqueous lithium–air batteries: status, challenges, and perspective.* ACS Catalysis, 2012. **2**(5): p. 844-857.

67. Park, M., H. Sun, H. Lee, J. Lee, and J. Cho, *Lithium–air batteries: Survey on the current status and perspectives towards automotive applications from a battery industry standpoint.* Advanced Energy Materials, 2012. **2**(7): p. 780-800.

68. Kwabi, D., N. Ortiz-Vitoriano, S. Freunberger, Y. Chen, N. Imanishi, P. Bruce, and Y. Shao-Horn, *Materials challenges in rechargeable lithium–air batteries.* MRS Bulletin, 2014. **39**(05): p. 443-452.

69. Imanishi, N. and O. Yamamoto, *Rechargeable lithium–air batteries: characteristics and prospects.* Materials Today, 2014. **17**(1): p. 24-30.

70. Ellis, B.L. and L.F. Nazar, *Sodium and sodium-ion energy storage batteries.* Current Opinion in Solid State and Materials Science, 2012. **16**(4): p. 168-177.

71. Kim, S.W., D.H. Seo, X. Ma, G. Ceder, and K. Kang, *Electrode materials for rechargeable sodium-ion batteries: potential alternatives to current lithium-ion batteries.* Advanced Energy Materials, 2012. **2**(7): p. 710-721.

72. Slater, M.D., D. Kim, E. Lee, and C.S. Johnson, *Sodium-ion batteries.* Advanced Functional Materials, 2013. **23**(8): p. 947-958.

73. Yabuuchi, N., K. Kubota, M. Dahbi, and S. Komaba, *Research development on sodium-ion batteries.* Chemical Reviews, 2014. **114**(23): p. 11636-11682.

74. Huie, M.M., D.C. Bock, E.S. Takeuchi, A.C. Marschilok, and K.J. Takeuchi, *Cathode materials for magnesium and magnesium-ion based batteries.* Coordination Chemistry Reviews, 2015. **287**: p. 15-27.

75. Kim, J.G., B. Son, S. Mukherjee, N. Schuppert, A. Bates, O. Kwon, M.J. Choi, H.Y. Chung, and S. Park, *A review of lithium and non-lithium based solid state batteries.* Journal of Power Sources, 2015. **282**: p. 299-322.

76. Simon, P. and Y. Gogotsi, *Materials for electrochemical capacitors.* Nature Materials, 2008. **7**(11): p. 845-854.

77. Goodenough, J.B. and Y. Kim, *Challenges for rechargeable Li batteries.* Chemistry of Materials, 2009. **22**(3): p. 587-603.

78. Zhang, Q., Q.-F. Dong, M.-S. Zheng, and Z.-W. Tian, *Electrochemical energy storage device for electric vehicles.* Journal of The Electrochemical Society, 2011. **158**(5): p. A443-A446.

79. Yue, Y. and H. Liang, *Hierarchical micro-architectures of electrodes for energy storage.* Journal of Power Sources, 2015. **284**: p. 435-445.

80. Yang, Z., J. Zhang, M.C. Kintner-Meyer, X. Lu, D. Choi, J.P. Lemmon, and J. Liu, *Electrochemical energy storage for green grid.* Chemical Reviews, 2011. **111**(5): p. 3577-613.

81. Kim, H., J. Hong, K.-Y. Park, H. Kim, S.-W. Kim, and K. Kang, *Aqueous rechargeable Li and Na ion batteries.* Chemical Reviews, 2014. **114**(23): p. 11788-11827.

82. Yoshio, M., R. Brodd, and A. Kozawa, *Lithium-ion batteries: science and technologies*. 2009, Springer. Berlin, Germany.

83. Dahn, J., T. Zheng, Y. Liu, and J. Xue, *Mechanisms for lithium insertion in carbonaceous materials.* Science, 1995. **270**(5236): p. 590.

84. Winter, M., J.O. Besenhard, M.E. Spahr, and P. Novak, *Insertion electrode materials for rechargeable lithium batteries.* Advanced Materials, 1998. **10**(10): p. 725-763.

85. Raccichini, R., A. Varzi, S. Passerini, and B. Scrosati, *The role of graphene for electrochemical energy storage.* Nature Materials, 2015. **14**(3): p. 271-279.

86. Ellis, B.L., K.T. Lee, and L.F. Nazar, *Positive electrode materials for Li-ion and Li-batteries.* Chemistry of Materials, 2010. **22**(3): p. 691-714.

87. Antolini, E., *LiCoO 2: formation, structure, lithium and oxygen nonstoichiometry, electrochemical behaviour and transport properties.* Solid State Ionics, 2004. **170**(3): p. 159-171.

88. Abraham, K., D. Pasquariello, and E. Willstaedt, *Discharge rate capability of the LiCoO2 electrode.* Journal of The Electrochemical Society, 1998. **145**(2): p. 482-486.

89. Amriou, T., B. Khelifa, H. Aourag, S. Aouadi, and C. Mathieu, *Ab initio investigation of the Jahn–Teller distortion effect on the stabilizing lithium intercalated compounds.* Materials Chemistry and Physics, 2005. **92**(2): p. 499-504.

90. Martha, S., E. Markevich, V. Burgel, G. Salitra, E. Zinigrad, B. Markovsky, H. Sclar, Z. Pramovich, O. Heik, and D. Aurbach, *A short review on surface chemical aspects of Li batteries: A key for a good performance.* Journal of Power Sources, 2009. **189**(1): p. 288-296.

91. Thackeray, M., A. De Kock, and W. David, *Synthesis and structural characterization of defect spinels in the lithium-manganese-oxide system.* Materials Research Bulletin, 1993. **28**(10): p. 1041-1049.

92. Padhi, A., K. Nanjundaswamy, C. Masquelier, S. Okada, and J. Goodenough, *Effect of structure on the Fe3+/Fe2+ redox couple in iron phosphates.* Journal of the Electrochemical Society, 1997. **144**(5): p. 1609-1613.

93. Patil, A., V. Patil, D. Wook Shin, J.-W. Choi, D.-S. Paik, and S.-J. Yoon, *Issue and challenges facing rechargeable thin film lithium batteries.* Materials Research Bulletin, 2008. **43**(8-9): p. 1913-1942.

94. Daniel, C. and J.O. Besenhard, *Handbook of battery materials*. 2012: John Wiley & Sons. Hoboken, NJ.

95. Wang, X., X.-L. Wu, Y.-G. Guo, Y. Zhong, X. Cao, Y. Ma, and J. Yao, *Synthesis and lithium storage properties of Co3O4 nanosheet-assembled multishelled hollow spheres.* Advanced Functional Materials, 2010. **20**(10): p. 1680-1686.

96. Hu, J., H. Li, and X. Huang, *Cr2O3-based anode materials for Li-ion batteries.* Electrochemical and Solid-State Letters, 2005. **8**(1): p. A66-A69.

97. Wang, Z., F. Su, S. Madhavi, and X.W. Lou, *CuO nanostructures supported on Cu substrate as integrated electrodes for highly reversible lithium storage.* Nanoscale, 2011. **3**(4): p. 1618-23.

98. Wang, B., J.S. Chen, H.B. Wu, Z. Wang, and X.W. Lou, *Quasiemulsion-templated formation of alpha-Fe2O3 hollow spheres with enhanced lithium storage properties.* Journal of American Chemical Society, 2011. **133**(43): p. 17146-8.

99. Xia, H., M. Lai, and L. Lu, *Nanoflaky MnO2/carbon nanotube nanocomposites as anode materials for lithium-ion batteries.* Journal of Materials Chemistry, 2010. **20**(33): p. 6896.

100. Liu, H., G. Wang, J. Liu, S. Qiao, and H. Ahn, *Highly ordered mesoporous NiO anode material for lithium ion batteries with an excellent electrochemical performance.* Journal of Materials Chemistry, 2011. **21**(9): p. 3046-3052.

101. Wang, Z., D. Luan, F.Y. Boey, and X.W. Lou, *Fast formation of SnO2 nanoboxes with enhanced lithium storage capability.* Journal of American Chemical Society, 2011. **133**(13): p. 4738-41.

102. Ren, Y., Z. Liu, F. Pourpoint, A.R. Armstrong, C.P. Grey, and P.G. Bruce, *Nanoparticulate TiO2 (B): an anode for lithium-ion batteries.* Angewandte Chemie International Edition, 2012. **51**(9): p. 2164-2167.

103. Dambournet, D., I. Belharouak, and K. Amine, *Tailored preparation methods of TiO2 anatase, rutile, brookite: Mechanism of formation and electrochemical properties.* Chemistry of Materials, 2010. **22**(3): p. 1173-1179.

104. Whittingham, M.S., Y. Song, S. Lutta, P.Y. Zavalij, and N.A. Chernova, *Some transition metal (oxy) phosphates and vanadium oxides for lithium batteries.* Journal of Materials Chemistry, 2005. **15**(33): p. 3362-3379.

105. Li, B., Y. Xu, G. Rong, M. Jing, and Y. Xie, *Vanadium pentoxide nanobelts and nanorolls: from controllable synthesis to investigation of their electrochemical properties and photocatalytic activities.* Nanotechnology, 2006. **17**(10): p. 2560.

106. Reddy, C.V.S., J. Wei, Z. Quan-Yao, D. Zhi-Rong, C. Wen, S.-i. Mho, and R.R. Kalluru, *Cathodic performance of (V2O5+PEG) nanobelts for Li ion rechargeable battery.* Journal of Power Sources, 2007. **166**(1): p. 244-249.

107. Cheah, S.K., E. Perre, M. Rooth, M. Fondell, A. Hårsta, L. Nyholm, M. Boman, T.r. Gustafsson, J. Lu, and P. Simon, *Self-supported three-dimensional nanoelectrodes for microbattery applications.* Nano Letters, 2009. **9**(9): p. 3230-3233.

108. Pan, Q., L. Qin, J. Liu, and H. Wang, *Flower-like ZnO–NiO–C films with high reversible capacity and rate capability for lithium-ion batteries.* Electrochimica Acta, 2010. **55**(20): p. 5780-5785.

109. Xiao, J., J. Zheng, X. Li, Y. Shao, and J.G. Zhang, *Hierarchically structured materials for lithium batteries.* Nanotechnology, 2013. **24**(42): p. 424004.

110. Chabi, S., C. Peng, D. Hu, and Y. Zhu, *Ideal three-dimensional electrode structures for electrochemical energy storage.* Advanced Materials, 2014. **26**(15): p. 2440-2445.

111. Zhao, H., W. Yuan, and G. Liu, *Hierarchical electrode design of high-capacity alloy nanomaterials for lithium-ion batteries.* Nano Today, 2015. **10**(2): p. 193-212.

112. Lee, S., J. Ha, J. Choi, T. Song, J.W. Lee, and U. Paik, *3D cross-linked nanoweb architecture of binder-free TiO2 electrodes for lithium ion batteries.* ACS Applied Materials & Interfaces, 2013. **5**(22): p. 11525-11529.

113. Hu, T., G. Xin, H. Sun, X. Sun, M. Yu, C. Liu, and J. Lian, *Electrospray deposition of a Co3O4 nanoparticles–graphene composite for a binder-free lithium ion battery electrode.* RSC Advances, 2014. **4**(4): p. 1521-1525.

114. Kaufman, J.G., *Introduction to aluminum alloys and tempers*. 2000: ASM International. Rossell Township, OH.

115. Davis, J.R., *Alloying: understanding the basics*. 2001: ASM International. Rossell Township, OH.

116. De Garmo, E.P., J.T. Black, and R.A. Kohser, *DeGarmo's Materials and Processes in Manufacturing*. 2011: John Wiley & Sons. Hoboken, NJ.

117. Smallwood, I., *Handbook of organic solvent properties*. 2012: Butterworth-Heinemann. Oxford, United Kingdom.

118. Bandyopadhyay, S., A.E. Miller, H.C. Chang, G. Banerjee, V. Yuzhakov, D.F. Yue, R.E. Ricker, S. Jones, J.A. Eastman, E. Baugher, and M. Chandrasekhar, *Electrochemically assembled quasi-periodic quantum dot arrays.* Nanotechnology, 1996. **7**(4): p. 360-371.

119. Vargel, C., *Corrosion of aluminium*. 2004: Elsevier. Amsterdam, the Netherlands

120. Tian, Z.-R., W. Tong, J.-Y. Wang, N.-G. Duan, V.V. Krishnan, and S.L. Suib, *Manganese oxide mesoporous structures: mixed-valent semiconducting catalysts.* Science, 1997. **276**(5314): p. 926-930.

121. Parlett, C.M., K. Wilson, and A.F. Lee, *Hierarchical porous materials: catalytic applications.* Chemical Society Reviews, 2013. **42**(9): p. 3876-3893.

122. Dubal, D., O. Ayyad, V. Ruiz, and P. Gómez-Romero, *Hybrid energy storage: the merging of battery and supercapacitor chemistries.* Chemical Society Reviews, 2015. **44**(7): p. 1777-1790.

123. Jun, S.-H., E.-J. Lee, T.-S. Jang, H.-E. Kim, J.-H. Jang, and Y.-H. Koh, *Bone morphogenic protein-2 (BMP-2) loaded hybrid coating on porous hydroxyapatite scaffolds for bone tissue engineering.* Journal of Materials Science: Materials in Medicine, 2013. **24**(3): p. 773-782.

124. Wang, C., Y. Li, Y.-S. Chui, Q.-H. Wu, X. Chen, and W. Zhang, *Three-dimensional Sn–graphene anode for high-performance lithium-ion batteries.* Nanoscale, 2013. **5**(21): p. 10599-10604.

125. Niu, Z., L. Liu, L. Zhang, Q. Shao, W. Zhou, X. Chen, and S. Xie, *A universal strategy to prepare functional porous graphene hybrid architectures.* Advanced Materials, 2014. **26**(22): p. 3681-3687.

126. Onda, T., S. Shibuichi, N. Satoh, and K. Tsujii, *Super-water-repellent fractal surfaces.* Langmuir, 1996. **12**(9): p. 2125-2127.

127. Drelich, J. and E. Chibowski, *Superhydrophilic and superwetting surfaces: definition and mechanisms of control.* Langmuir, 2010. **26**(24): p. 18621-18623.

128. Yuan, Y. and T.R. Lee, *Contact angle and wetting properties*, in *Surface science techniques*. 2013: Springer. Berlin, Germany.

129. Grewal, H., H.N. Kim, I.-J. Cho, and E.-S. Yoon, *Role of viscous dissipative processes on the wetting of textured surfaces.* Scientific Reports, 2015. **5**.

130. Jana, N.R., *Shape effect in nanoparticles self-assembly.* Angewandte Chemie International Edition, 2004. **43**(12): p. 1536-1540.

131. Sau, T.K. and C.J. Murphy, *Self-assembly patterns formed upon solvent evaporation of aqueous cetyltrimethylammonium bromide-coated gold nanoparticles of various shapes.* Langmuir, 2005. **21**(7): p. 2923-2929.

132. Singh, A., R.D. Gunning, S. Ahmed, C.A. Barrett, N.J. English, J.-A. Garate, and K.M. Ryan, *Controlled semiconductor nanorod assembly from solution: influence of concentration, charge and solvent nature.* Journal of Materials Chemistry, 2012. **22**(4): p. 1562-1569.

133. Tian, H.-C., J.-Q. Liu, D.-X. Wei, X.-Y. Kang, C. Zhang, J.-C. Du, B. Yang, X. Chen, H.-Y. Zhu, and Y.-N. NuLi, *Graphene oxide doped conducting polymer nanocomposite film for electrode-tissue interface.* Biomaterials, 2014. **35**(7): p. 2120-2129.

134. Kajiya*, T., D. Kaneko, and M. Doi, *Dynamical visualization of "coffee stain phenomenon" in droplets of polymer solution via fluorescent microscopy.* Langmuir, 2008. **24**(21): p. 12369-12374.

135. Eral, H.B., D.M. Augustine, M.H. Duits, and F. Mugele, *Suppressing the coffee stain effect: how to control colloidal self-assembly in evaporating drops using electrowetting.* Soft Matter, 2011. **7**(10): p. 4954-4958.

136. Majumder, M., C.S. Rendall, J.A. Eukel, J.Y. Wang, N. Behabtu, C.L. Pint, T.-Y. Liu, A.W. Orbaek, F. Mirri, and J. Nam, *Overcoming the "coffee-stain" effect by compositional Marangoni-flow-assisted drop-drying.* The Journal of Physical Chemistry B, 2012. **116**(22): p. 6536-6542.

137. Marozzi, C. and A. Chialvo, *Development of electrode morphologies of interest in electrocatalysis. Part 1: Electrodeposited porous nickel electrodes.* Electrochimica Acta, 2000. **45**(13): p. 2111-2120.

138. Wang, Y. and G. Cao, *Synthesis and enhanced intercalation properties of nanostructured vanadium oxides.* Chemistry of Materials, 2006. **18**(12): p. 2787-2804.

139. Yue, Y. and H. Liang, *Micro- and nano-structured vanadium pentoxide (V2O5) for electrodes of lithium-ion batteries.* Advanced Energy Materials, 2017. **7**: p. 1602545.

140. Chernova, N.A., M. Roppolo, A.C. Dillon, and M.S. Whittingham, *Layered vanadium and molybdenum oxides: batteries and electrochromics.* Journal of Materials Chemistry, 2009. **19**(17): p. 2526-2552.

141. Dewangan, K., N.N. Sinha, P.G. Chavan, P.K. Sharma, A.C. Pandey, M.A. More, D.S. Joag, N. Munichandraiah, and N.S. Gajbhiye, *Synthesis and*

characterization of self-assembled nanofiber-bundles of V2O5: their electrochemical and field emission properties. Nanoscale, 2012. **4**(2): p. 645-51.

142. Qu, B., L. Hu, Q. Li, Y. Wang, L. Chen, and T. Wang, *High-performance lithium-ion battery anode by direct growth of hierarchical ZnCo2O4 nanostructures on current collectors.* ACS Applied Materials & Interfaces, 2013. **6**(1): p. 731-736.

143. Rui, X., Z. Lu, H. Yu, D. Yang, H.H. Hng, T.M. Lim, and Q. Yan, *Ultrathin V2O5 nanosheet cathodes: realizing ultrafast reversible lithium storage.* Nanoscale, 2013. **5**(2): p. 556-560.

144. Fontenot, C.J., J.W. Wiench, M. Pruski, and G. Schrader, *Vanadia gel synthesis via peroxovanadate precursors. 1. in situ laser Raman and 51V NMR characterization of the gelation process.* The Journal of Physical Chemistry B, 2000. **104**(49): p. 11622-11631.

145. Liu, Y., M. Clark, Q. Zhang, D. Yu, D. Liu, J. Liu, and G. Cao, *V2O5 nano-electrodes with high power and energy densities for thin film Li-ion batteries.* Advanced Energy Materials, 2011. **1**(2): p. 194-202.

146. Zhu, J., L. Cao, Y. Wu, Y. Gong, Z. Liu, H.E. Hoster, Y. Zhang, S. Zhang, S. Yang, Q. Yan, P.M. Ajayan, and R. Vajtai, *Building 3D structures of vanadium pentoxide nanosheets and application as electrodes in supercapacitors.* Nano Letters, 2013. **13**(11): p. 5408-13.

147. Böker, A., J. He, T. Emrick, and T.P. Russell, *Self-assembly of nanoparticles at interfaces.* Soft Matter, 2007. **3**(10): p. 1231-1248.

148. Pan, A.Q., H.B. Wu, L. Zhang, and X.W.D. Lou, *Uniform V2O5 nanosheet-assembled hollow microflowers with excellent lithium storage properties.* Energy & Environmental Science, 2013. **6**(5): p. 1476-1479.

149. Rahman, M.M., A.Z. Sadek, I. Sultana, M. Srikanth, X.J. Dai, M.R. Field, D.G. McCulloch, S.B. Ponraj, and Y. Chen, *Self-assembled V2O5 interconnected microspheres produced in a fish-water electrolyte medium as a high-performance lithium-ion-battery cathode.* Nano Research, 2015. **8**(11): p. 3591-3603.

150. Zhou, L., Z. Zhuang, H. Zhao, M. Lin, D. Zhao, and L. Mai, *Intricate hollow structures: controlled synthesis and applications in energy storage and conversion.* Advanced Materials, 2017. **29**: p. 1602914.

151. Park, W.I., D.H. Kim, S.-W. Jung, and G.-C. Yi, *Metalorganic vapor-phase epitaxial growth of vertically well-aligned ZnO nanorods.* Applied Physics Letters, 2002. **80**(22): p. 4232-4234.

152. Lalmi, B., H. Oughaddou, H. Enriquez, A. Kara, S. Vizzini, B. Ealet, and B. Aufray, *Epitaxial growth of a silicene sheet.* Applied Physics Letters, 2010. **97**(22): p. 223109.

153. Zhou, M., W. Ming, Z. Liu, Z. Wang, P. Li, and F. Liu, *Epitaxial growth of large-gap quantum spin Hall insulator on semiconductor surface.* Proceedings of the National Academy of Sciences, 2014. **111**(40): p. 14378-14381.

154. Andre, D., S.-J. Kim, P. Lamp, S.F. Lux, F. Maglia, O. Paschos, and B. Stiaszny, *Future generations of cathode materials: an automotive industry perspective.* Journal of Materials Chemistry A, 2015. **3**(13): p. 6709-6732.

155. Tan, C. and H. Zhang, *Epitaxial growth of hetero-nanostructures based on ultrathin two-dimensional nanosheets.* Journal of the American Chemical Society, 2015. **137**(38): p. 12162-12174.

156. Rho, H., S. Lee, S. Bae, T.-W. Kim, D.S. Lee, H.J. Lee, J.Y. Hwang, T. Jeong, S. Kim, and J.-S. Ha, *Three-dimensional porous copper-graphene heterostructures with durability and high heat dissipation performance.* Scientific Reports, 2015. **5**: p. 12710.

157. Liu, P., Z. Fan, A. Mikhalchan, T.Q. Tran, D. Jewell, H.M. Duong, and A.M. Marconnet, *Continuous carbon nanotube-based fibers and films for applications requiring enhanced heat dissipation.* ACS Applied Materials & Interfaces, 2016. **8**(27): p. 17461-17471.

158. Balasingam, S.K., M.G. Kang, and Y. Jun, *Metal substrate based electrodes for flexible dye-sensitized solar cells: fabrication methods, progress and challenges.* Chemical Communications, 2013. **49**(98): p. 11457-11475.

159. Santos, R., J. Loureiro, A. Nogueira, E. Elangovan, J. Pinto, J. Veiga, T. Busani, E. Fortunato, R. Martins, and I. Ferreira, *Thermoelectric properties of V2O5 thin films deposited by thermal evaporation.* Applied Surface Science, 2013. **282**: p. 590-594.

160. Hanaor, D.A., I. Chironi, I. Karatchevtseva, G. Triani, and C.C. Sorrell, *Single and mixed phase TiO2 powders prepared by excess hydrolysis of titanium alkoxide.* Advances in Applied Ceramics, 2012. **111**(3): p. 149-158.

161. Verma, P., P. Maire, and P. Novák, *A review of the features and analyses of the solid electrolyte interphase in Li-ion batteries.* Electrochimica Acta, 2010. **55**(22): p. 6332-6341.

162. Xu, Q., J.Y. Li, J.K. Sun, Y.X. Yin, L.J. Wan, and Y.G. Guo, *Watermelon-inspired Si/C microspheres with hierarchical buffer structures for densely compacted lithium-ion battery anodes.* Advanced Energy Materials, 2017. **7**: p. 1601481.

163. Xu, J., C. Jia, B. Cao, and W. Zhang, *Electrochemical properties of anatase TiO 2 nanotubes as an anode material for lithium-ion batteries.* Electrochimica Acta, 2007. **52**(28): p. 8044-8047.

164. Chen, J.S., Y.L. Tan, C.M. Li, Y.L. Cheah, D. Luan, S. Madhavi, F.Y.C. Boey, L.A. Archer, and X.W. Lou, *Constructing hierarchical spheres from large ultrathin anatase TiO2 nanosheets with nearly 100% exposed (001) facets for fast reversible lithium storage.* Journal of the American Chemical Society, 2010. **132**(17): p. 6124-6130.

165. Shen, L., X. Zhang, H. Li, C. Yuan, and G. Cao, *Design and tailoring of a three-dimensional TiO2–graphene–carbon nanotube nanocomposite for fast lithium storage.* The Journal of Physical Chemistry Letters, 2011. **2**(24): p. 3096-3101.

166. Wang, Y., X. Su, and S. Lu, *Shape-controlled synthesis of TiO 2 hollow structures and their application in lithium batteries.* Journal of Materials Chemistry, 2012. **22**(5): p. 1969-1976.

167. Anh, L.T., A.K. Rai, T.V. Thi, J. Gim, S. Kim, E.-C. Shin, J.-S. Lee, and J. Kim, *Improving the electrochemical performance of anatase titanium dioxide by vanadium doping as an anode material for lithium-ion batteries.* Journal of Power Sources, 2013. **243**: p. 891-898.

168. Chen, S., Y. Xin, Y. Zhou, Y. Ma, H. Zhou, and L. Qi, *Self-supported Li4Ti5O12 nanosheet arrays for lithium ion batteries with excellent rate capability and ultralong cycle life.* Energy & Environmental Science, 2014. **7**(6): p. 1924-1930.

169. Geng, H., H. Ming, D. Ge, J. Zheng, and H. Gu, *Designed fabrication of fluorine-doped carbon coated mesoporous TiO2 hollow spheres for improved lithium storage.* Electrochimica Acta, 2015. **157**: p. 1-7.

170. Wang, B., J. Liu, Q. Sun, B. Xiao, R. Li, T.K. Sham, and X. Sun, *Titanium dioxide/lithium phosphate nanocomposite derived from atomic layer deposition as a high-performance anode for lithium ion batteries.* Advanced Materials Interfaces, 2016. **3**(21): p. 1600369.

171. Liu, R., J. Duay, and S.B. Lee, *Heterogeneous nanostructured electrode materials for electrochemical energy storage.* Chemical Communications, 2011. **47**(5): p. 1384-404.

172. Xu, K., *Electrolytes and interphases in Li-ion batteries and beyond.* Chemical Reviews, 2014. **114**(23): p. 11503-11618.

173. Barsoukov, E. and J.R. Macdonald, *Impedance spectroscopy: theory, experiment, and applications*. 2005: John Wiley & Sons. Hoboken, NJ.

174. Moisel, M., M.L. de Mele, and W.D. Müller, *Biomaterial interface investigated by electrochemical impedance spectroscopy.* Advanced Engineering Materials, 2008. **10**(10): p. B33-B46.

175. Chang, B.-Y. and S.-M. Park, *Electrochemical impedance spectroscopy.* Annual Review of Analytical Chemistry, 2010. **3**: p. 207-229.

176. Yoon, S. and A. Manthiram, *Hollow core–shell mesoporous TiO2 spheres for lithium ion storage.* The Journal of Physical Chemistry C, 2011. **115**(19): p. 9410-9416.

177. Ruffo, R., S.S. Hong, C.K. Chan, R.A. Huggins, and Y. Cui, *Impedance analysis of silicon nanowire lithium ion battery anodes.* The Journal of Physical Chemistry C, 2009. **113**(26): p. 11390-11398.

178. Han, C., D. Yang, Y. Yang, B. Jiang, Y. He, M. Wang, A.-Y. Song, Y.-B. He, B. Li, and Z. Lin, *Hollow titanium dioxide spheres as anode material for lithium ion battery with largely improved rate stability and cycle performance by suppressing the formation of solid electrolyte interface layer.* Journal of Materials Chemistry A, 2015. **3**(25): p. 13340-13349.

179. Zheng, P., T. Liu, Y. Su, L. Zhang, and S. Guo, *TiO2 nanotubes wrapped with reduced graphene oxide as a high-performance anode material for lithium-ion batteries.* Scientific Reports, 2016. **6**: p. 36580.

180. Yue, Y., D. Juarez-Robles, Y. Chen, L. Ma, K.W.C. H., P. Mukherjee, and H. Liang, *Hierarchical structured Cu/Ni/TiO2 nanocomposites as electrodes for lithium-ion batteries.* ACS Applied Materials and Interfaces, 2017. **9**(34): p. 28695-28703.

181. Mekonnen, Y., A. Sundararajan, and A.I. Sarwat. *A review of cathode and anode materials for lithium-ion batteries*. In *SoutheastCon, 2016*. 2016. Norfolk, VA. IEEE: p. 1-6.

182. Roy, P. and S.K. Srivastava, *Nanostructured anode materials for lithium ion batteries.* Journal of Materials Chemistry A, 2015. **3**(6): p. 2454-2484.

183. Chen, G., L. Yan, H. Luo, and S. Guo, *Nanoscale Engineering of Heterostructured Anode Materials for Boosting Lithium-Ion Storage.* Advanced Materials, 2016. **28**(35): p. 7580-7602.

184. Liu, Y., *Some consideration on the Langmuir isotherm equation.* Colloids and Surfaces A: Physicochemical and Engineering Aspects, 2006. **274**(1): p. 34-36.

185. Pivovarov, S., *Surface structure and site density of the oxide-solution interface.* Journal of Colloid and Interface Science, 1997. **196**(2): p. 321-323.

186. Kavan, L., J. Procházka, T.M. Spitler, M. Kalbáč, M. Zukalová, T. Drezen, and M. Grätzel, *Li insertion into Li4Ti5O12 (spinel) charge capability vs. particle size in thin-film electrodes.* Journal of the Electrochemical Society, 2003. **150**(7): p. A1000-A1007.

187. Xiao, Z., Y. Xia, Z. Ren, Z. Liu, G. Xu, C. Chao, X. Li, G. Shen, and G. Han, *Facile synthesis of single-crystalline mesoporous α-Fe2O3 and Fe3O4 nanorods as anode materials for lithium-ion batteries.* Journal of Materials Chemistry, 2012. **22**(38): p. 20566-20573.

188. Shen, L., E. Uchaker, X. Zhang, and G. Cao, *Hydrogenated Li4Ti5O12 nanowire arrays for high rate lithium ion batteries.* Advanced Materials, 2012. **24**(48): p. 6502-6506.

189. Yang, Y., H. Wang, Q. Zhou, M. Kong, H. Ye, and G. Yang, *Improved lithium storage properties of electrospun TiO2 with tunable morphology: from porous anatase to necklace rutile.* Nanoscale, 2013. **5**(21): p. 10267-10274.

190. Xia, X., Q. Xiong, Y. Zhang, J. Tu, C.F. Ng, and H.J. Fan, *Oxide nanostructures hyperbranched with thin and hollow metal shells for high-performance nanostructured battery electrodes.* Small, 2014. **10**(12): p. 2419-2428.

191. Wang, X., B. Liu, X. Hou, Q. Wang, W. Li, D. Chen, and G. Shen, *Ultralong-life and high-rate web-like Li4Ti5O12 anode for high-performance flexible lithium-ion batteries.* Nano Research, 2014. **7**(7): p. 1073-1082.

192. Huang, L., X. Wang, F. Yin, C. Zhang, J. Gao, J. Liu, G. Zhou, Y. Zhang, and Z. Bakenov, *Three-dimensional carbon cloth-supported ZnO nanorod arrays as a binder-free anode for lithium-ion batteries.* Journal of Nanoparticle Research, 2017. **19**(2): p. 42.

193. Sim, D.H., X. Rui, J. Chen, H. Tan, T.M. Lim, R. Yazami, H.H. Hng, and Q. Yan, *Direct growth of FeVO4 nanosheet arrays on stainless steel foil as high-performance binder-free Li ion battery anode.* RSC Advances, 2012. **2**(9): p. 3630-3633.

194. Zhang, H. and P.V. Braun, *Three-dimensional metal scaffold supported bicontinuous silicon battery anodes.* Nano Letters, 2012. **12**(6): p. 2778-2783.

195. Sun, Y., J. Wang, B. Zhao, R. Cai, R. Ran, and Z. Shao, *Binder-free α-MoO3 nanobelt electrode for lithium-ion batteries utilizing van der Waals forces for film formation and connection with current collector.* Journal of Materials Chemistry A, 2013. **1**(15): p. 4736-4746.

196. Zhao, Y., L. Peng, B. Liu, and G. Yu, *Single-crystalline LiFePO4 nanosheets for high-rate Li-ion batteries.* Nano Letters, 2014. **14**(5): p. 2849-2853.

197. Xia, H., Q. Xia, B. Lin, J. Zhu, J.K. Seo, and Y.S. Meng, *Self-standing porous LiMn2O4 nanowall arrays as promising cathodes for advanced 3D microbatteries and flexible lithium-ion batteries.* Nano Energy, 2016. **22**: p. 475-482.

198. Yue, Y., D. Juarez-Robles, P. Mukherjee, and H. Liang, *Super-hierarchical nickel-vanadia nanocomposites as cathodes for lithium-ion batteries.* Journal of Materials Chemistry A, 2018. under review.

199. Choi, J., S. Lee, J. Ha, T. Song, and U. Paik, *Sol–gel nanoglues for an organic binder-free TiO2 nanofiber anode for lithium ion batteries.* Nanoscale, 2013. **5**(8): p. 3230-3234.

200. Huang, X., J. Chen, Z. Lu, H. Yu, Q. Yan, and H.H. Hng, *Carbon inverse opal entrapped with electrode active nanoparticles as high-performance anode for lithium-ion batteries.* Scientific Reports, 2013. **3**: p. 2317.

201. Luo, J., J. Liu, Z. Zeng, C.F. Ng, L. Ma, H. Zhang, J. Lin, Z. Shen, and H.J. Fan, *Three-dimensional graphene foam supported Fe3O4 lithium battery anodes with long cycle life and high rate capability.* Nano Letters, 2013. **13**(12): p. 6136-6143.

202. Huang, Z.X., Y. Wang, Y.G. Zhu, Y. Shi, J.I. Wong, and H.Y. Yang, *3D graphene supported MoO2 for high performance binder-free lithium ion battery.* Nanoscale, 2014. **6**(16): p. 9839-9845.

203. Qin, J., C. He, N. Zhao, Z. Wang, C. Shi, E.-Z. Liu, and J. Li, *Graphene networks anchored with Sn@graphene as lithium ion battery anode.* ACS Nano, 2014. **8**(2): p. 1728-1738.

204. Wan, Y., Z. Yang, G. Xiong, R. Guo, Z. Liu, and H. Luo, *Anchoring Fe3O4 nanoparticles on three-dimensional carbon nanofibers toward flexible high-performance anodes for lithium-ion batteries.* Journal of Power Sources, 2015. **294**: p. 414-419.

205. Gao, H., F. Hou, Z. Wan, S. Zhao, D. Yang, J. Liu, A. Guo, and Y. Gong, *One-step synthesis of continuous free-standing carbon nanotubes-titanium oxide composite films as anodes for lithium-ion batteries.* Electrochimica Acta, 2015. **154**: p. 321-328.

206. Tian, X., Y. Zhou, X. Tu, Z. Zhang, and G. Du, *Well-dispersed LiFePO4 nanoparticles anchored on a three-dimensional graphene aerogel as high-performance positive electrode materials for lithium-ion batteries.* Journal of Power Sources, 2017. **340**: p. 40-50.

207. ten Elshof, J.E., H. Yuan, and P. Gonzalez Rodriguez, *Two-dimensional metal oxide and metal hydroxide nanosheets: synthesis, controlled assembly and applications in energy conversion and storage.* Advanced Energy Materials, 2016. **6**: p. 1600355.

208. Zhang, X., L. Hou, A. Ciesielski, and P. Samorì, *2D materials beyond graphene for high-performance energy storage applications.* Advanced Energy Materials, 2016. **6**: p. 1600671.

209. Wei, Q., F. Xiong, S. Tan, L. Huang, E.H. Lan, B. Dunn, and L. Mai, *Porous one-dimensional nanomaterials: design, fabrication and applications in electrochemical energy storage.* Advanced Materials, 2017. **29**: p. 1602300.

210. Yu, L., H. Hu, H.B. Wu, and X.W.D. Lou, *Complex hollow nanostructures: synthesis and energy-related applications.* Advanced Materials, 2017. **29**: p. 1604563.

211. Long, J.W., B. Dunn, D.R. Rolison, and H.S. White, *Three-dimensional battery architectures.* Chemical Reviews, 2004. **104**(10): p. 4463-4492.

212. Etiemble, A., J. Adrien, E. Maire, H. Idrissi, D. Reyter, and L. Roué, *3D morphological analysis of copper foams as current collectors for Li-ion batteries by means of X-ray tomography.* Materials Science and Engineering: B, 2014. **187**: p. 1-8.